

# **Broadband Feed Antenna Design**

by

André Mark Allan Johnson

B. Eng., The University of Victoria, 2008

A THESIS SUBMITTED IN PARTIAL FULFILLMENT  
OF THE REQUIREMENTS FOR THE DEGREE OF  
MASTER OF APPLIED SCIENCE

in

THE COLLEGE OF GRADUATE STUDIES  
(Applied Science)

THE UNIVERSITY OF BRITISH COLUMBIA  
(Okanagan)

September 2012

© André Mark Allan Johnson, 2012

# Abstract

This thesis describes the development of a log-periodic waveguide feed antenna from concept to design and finally to prototyping and testing. An electromagnetic simulator (CST) was used to evaluate different design concepts and a design based on a nested coaxial waveguide structure was selected. A design was developed that included a common excitation structure for all the waveguides and an aperture matching structure that scales periodically with frequency. In the design, each waveguide has a bandwidth ratio of 2:1 and the total bandwidth of the design is 1 GHz to 8 GHz. A physical model was created using the SolidWorks design software and a prototype was manufactured and tested. Simulation results were in good agreement with the experimental results over the majority of the antenna's bandwidth. The antenna design had good farfield patterns across most of the antenna's bandwidth with frequency-specific farfield issues. The return loss of the antenna varied greatly with frequency, being greater than 2 dB across the entire bandwidth of the antenna and greater than 6 dB for the majority of the bandwidth of the antenna. There were significant difficulties in achieving a good return loss at the aperture which limited the return loss of the antenna. This work demonstrates the potential of employing a nested coaxial waveguide structure for wideband feed applications.

# Preface

This project was a collaboration between the National Research Council of Canada (NRC) and the University of British Columbia (UBC). The primary research site for the project was the Dominion Radio Astrophysical Observatory (DRAO) in Penticton, BC. The prototype was fabricated at the UBC Okanagan Campus and assembled and tested at DRAO. Funding for the project was provided by NRC, UBC, and the research grants of Dr. Julian Cheng and Dr. Thomas Johnson.

The project concept was created by Dr. Tom Landecker and Dr. Bruce Veidt at DRAO. The primary researcher for this project was André Johnson with consultation from Dr. Landecker and Dr. Veidt at DRAO and Dr. Johnson at UBC. André Johnson is the author of this thesis with editing assistance from Dr. Landecker, Dr. Johnson, and Dr. Veidt.

# Table of Contents

<b>Abstract</b> . . . . .	<b>ii</b>
<b>Preface</b> . . . . .	<b>iii</b>
<b>Table of Contents</b> . . . . .	<b>iv</b>
<b>List of Tables</b> . . . . .	<b>ix</b>
<b>List of Figures</b> . . . . .	<b>xi</b>
<b>Acronyms</b> . . . . .	<b>xvi</b>
<b>Glossary</b> . . . . .	<b>xviii</b>
<b>Acknowledgements</b> . . . . .	<b>xxi</b>
<b>Chapter 1 Introduction</b> . . . . .	<b>1</b>
1.1 Rationale . . . . .	1
1.2 Background Information . . . . .	2
1.2.1 Antenna Design . . . . .	2
1.2.2 Radio Astronomy . . . . .	6
1.2.3 Maxwell's Equations . . . . .	10
1.2.4 Waveguides . . . . .	12
1.2.5 Farfield . . . . .	15
1.2.6 Return Loss . . . . .	19
<b>Chapter 2 Related Work</b> . . . . .	<b>21</b>

2.1	Coaxial Waveguide . . . . .	21
2.2	Circular Waveguide Antenna . . . . .	22
2.3	Corrugated Feed Horn Antenna . . . . .	22
2.4	Eleven Antenna . . . . .	22
2.5	Log-Periodic Spiral Antenna . . . . .	23
<b>Chapter 3</b>	<b>Tools Used . . . . .</b>	<b>25</b>
3.1	Computer Simulation Technology . . . . .	25
3.1.1	Transient Solver . . . . .	25
3.1.2	Frequency Analysis . . . . .	26
3.1.3	Hexahedral Gridding . . . . .	26
3.1.4	Parameter Sweeps and Optimization . . . . .	26
3.1.5	Time vs Accuracy Trade-Off . . . . .	27
3.1.6	Simulation Limitations of CST . . . . .	28
3.1.7	Assumptions Adopted to Reduce Simulation Time . . . . .	28
3.1.8	Blackbox Simulator . . . . .	29
3.2	Solidworks . . . . .	29
3.3	AutoCAD / Gimp / Inkscape . . . . .	29
3.4	Matlab / Octave / Excel . . . . .	30
3.5	R . . . . .	30
<b>Chapter 4</b>	<b>Design Goals . . . . .</b>	<b>31</b>
4.1	Overall Design Goals . . . . .	31
4.2	Waveguide Coupling Design Goals . . . . .	31
4.3	Farfield Design Goals . . . . .	32
4.4	Physical Constraints . . . . .	33
<b>Chapter 5</b>	<b>Design Procedure . . . . .</b>	<b>34</b>
5.1	Concept . . . . .	34
5.2	Choosing the General Waveguide Shape . . . . .	35
5.3	Farfield Bandwidth of Coaxial Waveguides . . . . .	36
5.3.1	Effect of Nested Waveguides on Farfield Band- width . . . . .	38

5.4	Four Section Piece-Wise Design . . . . .	40
5.5	Designing the Aperture . . . . .	41
5.6	Designing the Excitation Structure . . . . .	43
5.6.1	Excitation Structure Goals . . . . .	44
5.6.2	Feed Line Design . . . . .	45
5.6.3	Excitation Element Design . . . . .	48
5.6.4	Analyzing the Farfield of the Partial Model . . . . .	59
5.6.5	Suppressing the TE <sub>31</sub> Mode . . . . .	60
5.7	Designing the Aperture Matching Structure . . . . .	62
5.8	Designing the Choke . . . . .	63
5.9	Aperture Alignment Section Length Sweep . . . . .	65
<b>Chapter 6</b>	<b>Physical Prototype Design . . . . .</b>	<b>67</b>
6.1	Front Section . . . . .	67
6.2	Back Section . . . . .	68
6.2.1	Feed Line Termination . . . . .	68
6.3	Assembling the Components . . . . .	71
6.4	The Feed Centre Assembly . . . . .	74
<b>Chapter 7</b>	<b>Prototype Fabrication and Assembly . . . . .</b>	<b>75</b>
7.1	Fabricating the Components . . . . .	75
7.2	Building the Feed Centre Assembly . . . . .	76
7.2.1	Testing the Feeding Cables . . . . .	77
7.2.2	Assembling the Feed Centre Assembly . . . . .	78
7.3	Assembling the Full Prototype . . . . .	79
<b>Chapter 8</b>	<b>Prototype Testing . . . . .</b>	<b>85</b>
8.1	Network Analyzer Tests . . . . .	85
8.1.1	Alternative Feed Line Termination Tests . . . . .	90
8.1.2	Addressing the Return Loss Shortfall . . . . .	90
8.2	Farfield Testing . . . . .	91
<b>Chapter 9</b>	<b>Results . . . . .</b>	<b>98</b>
9.1	Return Loss . . . . .	98

9.2	Farfield Results . . . . .	98
<b>Chapter 10</b>	<b>Discussion . . . . .</b>	<b>114</b>
10.1	Comparison of Simulated and Experimental Return Loss . . . . .	114
10.2	Evaluation of Return Loss . . . . .	116
10.3	Simulated Farfield Patterns . . . . .	118
10.4	Experimental Farfield Patterns . . . . .	120
10.5	Comparing Simulated and Experimental Farfield Patterns . . . . .	124
10.6	Correlation Between Return Loss and the Quality of the Farfield Patterns . . . . .	124
10.7	Effects of Poor Return Loss at the Aperture . . . . .	127
10.8	Issues with Prototype Construction . . . . .	127
10.9	General Feasibility of the Design . . . . .	129
<b>Chapter 11</b>	<b>Further Work . . . . .</b>	<b>130</b>
11.1	Improved Aperture Matching Structure . . . . .	130
11.2	Feed Centre Redesign . . . . .	131
11.3	Balun . . . . .	131
11.4	Excitation Optimization and Redesign . . . . .	131
11.5	Mode and Frequency Filtering . . . . .	132
11.6	Dielectric Lenses . . . . .	132
11.7	Choke Study . . . . .	133
11.8	Aperture Alignment Section Length Study . . . . .	133
11.9	Phase Study . . . . .	133
11.10	Cryogenic Study . . . . .	133
11.11	Full Model Optimization . . . . .	134
11.12	Improved Fabrication Techniques . . . . .	134
11.13	Alternative Designs . . . . .	134
<b>Chapter 12</b>	<b>Conclusion . . . . .</b>	<b>135</b>
	<b>Bibliography . . . . .</b>	<b>137</b>

**Appendices . . . . . 141**

- Appendix A DRAO Concept Document . . . . . 141
- Appendix B DRAO Concept Drawing I . . . . . 147
- Appendix C DRAO Concept Drawing II . . . . . 149
- Appendix D Prototype Construction Drawings . . . . . 151
- Appendix E Feed Line Construction Drawings . . . . . 161

# List of Tables

Table 1.1	Values of $x'_{m1}$ for TE Modes in Coaxial Waveguides. From [18]	14
Table 3.1	Comparison of Optimization Algorithms Used by CST . . . . .	27
Table 4.1	Design Goals for the Overall Antenna . . . . .	31
Table 4.2	Coupling Design Goals . . . . .	32
Table 4.3	Design Goals for the Farfield Pattern . . . . .	33
Table 4.4	Relaxed Design Goals for the Farfield Patterns . . . . .	33
Table 5.1	Parameters Used to Define Waveguide Geometry . . . . .	36
Table 5.2	Model Dimensions for Waveguide Ratio Farfield Test . . . . .	37
Table 5.3	Bandwidth Results for Single Waveguide Ratio Tests . . . . .	38
Table 5.4	Bandwidth Results for Nested Waveguide Simulations . . . . .	39
Table 5.5	Comparing the Bandwidth under the Original and Relaxed Farfield Goals . . . . .	40
Table 5.6	Parameters for Maximum Replication Ratio with Regards to Farfield Patterns . . . . .	40
Table 5.7	Return Loss for Various Values of $\zeta$ when $t \approx 0$ . . . . .	42
Table 5.8	Final Aperture Design Parameters . . . . .	43
Table 5.9	Design Goals for Individual Excitation Structures . . . . .	44
Table 5.10	Design Dimensions for Redesigned Feed Line . . . . .	47
Table 5.11	Parameter Results for the Partially Optimized Crossbar Excita- tion Design . . . . .	49
Table 5.12	Parameter Results for the Optimized “Frisbee” Excitation Design	52
Table 5.13	Parameter Results for the Optimized Hybrid Excitation Design	55

Table 5.14	Parameter Results for the Optimized Three-Angle Excitation Design . . . . .	57
Table 5.15	Results of Aperture Matching Structure Design . . . . .	63
Table 5.16	Design Dimensions for Choke . . . . .	65
Table 8.1	Manufacturer’s Specification for Hybrids . . . . .	87
Table 8.2	Specification of Probes Used for Nearfield Measurements . . .	95
Table 8.3	Software Used in the Antenna Laboratory . . . . .	97

# List of Figures

Figure 1.1	Operating Frequency Band of One Antenna . . . . .	5
Figure 1.2	Operating Frequency Bands of Multiple Antennas . . . . .	5
Figure 1.3	Log-Periodic Dipole Array . . . . .	6
Figure 1.4	Parabolic Antenna and Feed Antenna . . . . .	7
Figure 1.5	Atmospheric Electromagnetic Opacity . . . . .	8
Figure 1.6	Electric Fields of Modes in a Circular Coaxial Waveguide . .	16
Figure 1.7	Farfield Coordinate System . . . . .	17
Figure 1.8	Linearly Polarized Waves . . . . .	18
Figure 1.9	Circularly Polarized Wave . . . . .	18
Figure 1.10	Test Setup for Ludwig's Third Definition of Polarization . .	19
Figure 2.1	An Eleven Antenna Built at DRAO . . . . .	23
Figure 2.2	Log-Periodic Spiral Antenna Designed and Built at DAO . .	24
Figure 5.1	Generic Layout of Rectangular Waveguide Antenna . . . . .	35
Figure 5.2	CST Model for Testing Nested Waveguides . . . . .	38
Figure 5.3	Four Section Design . . . . .	41
Figure 5.4	Electric Field of the $TE_{11}$ Mode in a Coaxial Waveguide . .	44
Figure 5.5	Port Definitions for Individual Generic Excitation Structure .	45
Figure 5.6	Parameters for Finding the Characteristic Impedance of a Rectangular Coaxial Waveguide . . . . .	46
Figure 5.7	Stepped Feed Line . . . . .	47
Figure 5.8	Crossbar Excitation Design . . . . .	49
Figure 5.9	Simulated Crossbar Excitation Design Results . . . . .	50

Figure 5.10	Simulated Crossbar Excitation Design Results – Extended Frequency Range . . . . .	50
Figure 5.11	“Frisbee” Excitation Design . . . . .	52
Figure 5.12	Simulated “Frisbee” Excitation Design Results . . . . .	53
Figure 5.13	TE <sub>11</sub> and TE <sub>31</sub> Modes in Simulated “Frisbee” Excitation De- sign Results . . . . .	53
Figure 5.14	Hybrid Excitation Design . . . . .	54
Figure 5.15	Simulated Hybrid Excitation Design Results . . . . .	55
Figure 5.16	TE <sub>11</sub> and TE <sub>31</sub> Modes in Simulated Hybrid Excitation Design Results . . . . .	56
Figure 5.17	Three-Angle Excitation Design . . . . .	58
Figure 5.18	Electric Performance of Three-Angle Excitation Design . . .	59
Figure 5.19	Electric Field for the TE <sub>31</sub> Mode in a Coaxial Waveguide . .	61
Figure 5.20	45° Walls with the TE <sub>31</sub> Mode Overlaid . . . . .	61
Figure 5.21	Cross Section of a Generic Stepped Matching Structure . . .	62
Figure 5.22	Return Loss for Optimized Aperture Matching Structure . .	64
Figure 5.23	Cross Section of a Generic Choke . . . . .	65
Figure 6.1	Assembled Components of the Front Section . . . . .	69
Figure 6.2	Inner Cylinders of the Front Section . . . . .	69
Figure 6.3	Outer Cylinder of the Front Section with Choke Attached . .	70
Figure 6.4	Fabricated Choke . . . . .	70
Figure 6.5	Cross Section of the Back Section . . . . .	71
Figure 6.6	Screw Locations to Secure Cylinders . . . . .	72
Figure 6.7	Cross Section of Choke Showing Screw Clearances . . . . .	72
Figure 6.8	Mounting Plate for Attaching Prototypes to Testing Equipment	73
Figure 6.9	Back Section Secured to the Mounting Plate . . . . .	73
Figure 6.10	The Brass Plug . . . . .	74
Figure 7.1	Fabricated Combined Feed Line and Excitation Elements . .	76
Figure 7.2	Preparing the SMA Cables for Assembly . . . . .	77
Figure 7.3	Prepared SMA Cables . . . . .	77
Figure 7.4	Measured $ S_{11} $ for the Four Feeding Cables . . . . .	78

Figure 7.5	Assembled Feed Assembly . . . . .	79
Figure 7.6	Back View of Assembled Back Section and Mounting Plate .	80
Figure 7.7	Front View of Assembled Back Section and Mounting Plate .	80
Figure 7.8	Connections to Feed Line . . . . .	81
Figure 7.9	Excitation Structure Soldered in Position . . . . .	82
Figure 7.10	Fully Assembled Back Section . . . . .	82
Figure 7.11	Fully Assembled Back Section with 50 $\Omega$ Terminations . . .	83
Figure 7.12	Front Section Attached without Choke . . . . .	83
Figure 7.13	Front Section Attached with Choke . . . . .	84
Figure 8.1	Simulated Differential Port Test Setup with Absorbing Foam	86
Figure 8.2	Test Setup for Comparing the Performance of the Polarizations	88
Figure 8.3	Comparing the Network Analyzer Differential Source to a Single Source with Hybrid for Band One . . . . .	88
Figure 8.4	Comparing the Network Analyzer Differential Source to a Single Source with Hybrid for Band Two . . . . .	89
Figure 8.5	Comparing the Network Analyzer Differential Source to a Single Source with Hybrid for Band Three . . . . .	89
Figure 8.6	Feed Line Terminations for Bench Tests . . . . .	90
Figure 8.7	Fabricated Brass Filler Plug . . . . .	91
Figure 8.8	Brass Filler Plug Installed in Back Section . . . . .	92
Figure 8.9	Brass Filler Plug Secured with Copper Tape . . . . .	92
Figure 8.10	The Anechoic Chamber at DRAO . . . . .	93
Figure 8.11	Network Analyzer (Top) and Motor Controller (Bottom) for the Anechoic Chamber . . . . .	94
Figure 8.12	Balun Attached to the Prototype and Shielded by Radio Ab- sorbing Material . . . . .	95
Figure 8.13	Probe in the Anechoic Chamber . . . . .	96
Figure 8.14	Probe in the Anechoic Chamber with Radio Absorbing Material	96
Figure 9.1	Simulated Return Loss . . . . .	99
Figure 9.2	Experimental Return Loss Using 50 $\Omega$ Feed Line Terminations	99

Figure 9.3	Experimental Return Loss Using Short Circuit Feed Line Terminations . . . . .	100
Figure 9.4	Experimental Return Loss Using Open Circuit Feed Line Terminations . . . . .	100
Figure 9.5	Prototype Return Loss of Prototype with Feed Line Modifications . . . . .	101
Figure 9.6	Simulated Farfield Patterns . . . . .	102
Figure 9.7	Simulated Farfield Patterns . . . . .	103
Figure 9.8	Simulated Farfield Patterns . . . . .	104
Figure 9.9	Simulated Farfield Patterns . . . . .	105
Figure 9.10	Experimental Farfield Patterns – E-Plane Co-Polarization and Cross-Polarization . . . . .	106
Figure 9.11	Experimental Farfield Patterns – E-Plane Co-Polarization and Cross-Polarization . . . . .	107
Figure 9.12	Experimental Farfield Patterns – E-Plane Co-Polarization and Cross-Polarization . . . . .	108
Figure 9.13	Experimental Farfield Patterns – E-Plane Co-Polarization and Cross-Polarization . . . . .	109
Figure 9.14	Experimental Farfield Patterns – H-Plane Co-Polarization . . . . .	110
Figure 9.15	Experimental Farfield Patterns – H-Plane Co-Polarization . . . . .	111
Figure 9.16	Experimental Farfield Patterns – H-Plane Co-Polarization . . . . .	112
Figure 9.17	Experimental Farfield Patterns – H-Plane Co-Polarization . . . . .	113
Figure 10.1	Comparison of Return Loss Data . . . . .	115
Figure 10.2	Return Loss Block Diagram . . . . .	117
Figure 10.3	Near Ideal Farfield Pattern – Design Simulation – 2.05 GHz . . . . .	118
Figure 10.4	Dual-Peak Farfield Pattern – Simulation – 3.15 GHz . . . . .	119
Figure 10.5	Weak Dual-Peak Farfield Pattern – Simulation – 3.35 GHz . . . . .	120
Figure 10.6	Farfield at Frequency Band Overlap – Simulation – 4 GHz . . . . .	121
Figure 10.7	Near Ideal Farfield Pattern – Experimental – 2.1 GHz . . . . .	122
Figure 10.8	Dual-Peak Farfield Pattern – Experimental – 6 GHz . . . . .	122
Figure 10.9	Multi-Peak Farfield Pattern – Experimental – 6.35 GHz . . . . .	123
Figure 10.10	Asymmetrical Farfield Pattern – Experimental – 2.2 GHz . . . . .	123

Figure 10.11	Good Agreement in Farfield Results – 2.8 GHz . . . . .	125
Figure 10.12	Different Amplitude of Dual-Peak – 4.05 GHz . . . . .	125
Figure 10.13	Poor Agreement in Farfield Results – 4.35 GHz . . . . .	126
Figure 10.14	Sample from Extended Frequency Range of Poor Agreement in Farfield Results – 5.5 GHz . . . . .	126
Figure 10.15	Semi-rigid SMA Cable Protruding from Back Section . . . . .	128

# Acronyms

<b>ARO</b>	Algonquin Radio Observatory
<b>CNC</b>	computer numerical control
<b>CST</b>	Computer Simulation Technology, a suite of electromagnetic simulation tools, produced by a company of the same name
<b>DAO</b>	Dominion Astrophysical Observatory, an optical observatory and research site located in Victoria, BC
<b>DRAO</b>	Dominion Radio Astrophysical Observatory, a radio observatory and research site located outside Penticton, BC
<b>EVLA</b>	Expanded Very Large Array, a radio telescope in New Mexico, USA
<b>FFT</b>	fast Fourier transformation
<b>FIT</b>	finite integration technique
<b>IRAS</b>	Infrared Astronomical Satellite
<b>LNA</b>	low noise amplifier
<b>MWS</b>	Microwave Studio, a package in the CST software suite
<b>NRC</b>	National Research Council of Canada
<b>PCB</b>	printed circuit board
<b>PSD</b>	power spectral density

<b>RL</b>	return loss
<b>SKA</b>	Square Kilometre Array, a proposed radio telescope project located in Australia, New Zealand, and Southern Africa
<b>SMA</b>	subminiature version A, a common type of coaxial connector
<b>TE</b>	Transverse Electric
<b>TEM</b>	Transverse Electromagnetic
<b>TM</b>	Transverse Magnetic
<b>UBC</b>	University of British Columbia
<b>UVic</b>	University of Victoria
<b>VBA</b>	Visual Basic for Applications
<b>VLA</b>	Very Large Array, the predecessor to the EVLA
<b>VLBI</b>	very long baseline interferometry, a technique of using multiple antennas separated by very large distances to increase the angular resolution of the device

# Glossary

**Angular Resolution** The minimum angular separation between two objects that can be distinguished by the instrument.

**Back Lobe** In the farfield pattern, the side lobe that is in the opposite direction of the main lobe is the back lobe.

**Balun** A device that converts two balanced electrical signals to one unbalanced electrical signal and vice versa.

**Boresight** The direction of the main lobe of the radiation pattern which is located at  $\theta = 0^\circ$  in the antenna coordinate system.

**Choke Ring** A coaxial ring, usually  $\lambda/4$  in depth, placed around the aperture of a waveguide antenna to improve the farfield performance of the antenna by suppressing, or choking, currents flowing on the outside of the antenna.

**Co-polarization** In linear polarization, the component of the radiation parallel to the desired polarization.

**Correlator** A device, usually digital, that processes signals from one or more antennas to derive the auto-correlation or cross-correlation function. Application of the Fourier transformation can then produce the power spectrum of the signal(s).

**Cross-polarization** In linear polarization, the component of the radiation orthogonal to the desired polarization.

**Cutoff Frequency** The frequency at which a waveguide mode will propagate in an ideal waveguide without loss of amplitude, below which the wave is strongly attenuated, and is said to be cutoff.

**Directivity** The ratio of the power density in a given direction from the antenna over the power density averaged over all directions. If the direction is not specified, it is assumed to be in the direction of maximum power density [4, pp.17].

**Dominant Mode** The waveguide mode, other than the TEM mode, with the lowest cutoff frequency.

**Electrical Size** The dimensions of an object that are used for electrical calculations. Electrical size is variable and determined by a number of parameters such as dielectric material and frequency. This is in contrast to physical size which is constant.

**E-plane** The plane containing the electric field vector at the excitation source.

**Farfield Pattern** The field power amplitudes taken at an arbitrarily large distance from the antenna, such that the farfield distribution can be represented only in terms of angles from reference planes.

**Feed** An antenna designed to collect energy at the focal point of a reflector antenna or supply energy to a reflector antenna.

**Field Symmetry** Refers to how circularly symmetric the farfield pattern is. In this thesis this is measured by the similarity of the E-plane and H-plane farfield patterns.

**H-plane** The plane containing the magnetic field vector at the excitation source. In linear polarization, the H-plane is orthogonal to the E-plane.

**Main Lobe** In the farfield pattern, the lobe containing maximum power density.

**Mode** An eigenfunction that is a solution to Maxwell's field equations that satisfies the boundary conditions of the waveguide and describes a propagating wave.

**Over-moded** A waveguide with modes other than the desired mode propagating is said to be over-moded.

**Phase Centre** The centre of a sphere that is the best fit to the electromagnetic wave front radiated by an antenna.

**Polarization** Refers to the description of a wave as it propagates through space.

**Return Loss** A measure of how much power is lost as a result of a mismatched electrical load.

**Radio Interferometry** A method of using multiple antennas together simultaneously in order to increase the amount of signal collected and to increase the angular resolution of the device.

**Replication Ratio ( $\eta$ )** The scaling factor from one waveguide to the next waveguide.

**Resolving Power** The ability of a device to differentiate two objects separated by a small angular distance.

**Resonance** The increase in oscillation amplitude at certain frequencies dictated by the electrical properties of a system

**Shield** The outer conductor of a coaxial cable. Normally the shield is kept at a common electrical potential.

**Side Lobe** In the farfield pattern, any lobe that is not the main lobe is a side lobe.

**Transverse** Perpendicular to the direction of propagation.

**Waveguide** A metallic structure, that may or may not be partially or completely filled with a dielectric material, which guides electromagnetic waves from one location to another.

# Acknowledgements

This project would not be possible without the guidance, mentoring, and patience of my supervisors, Dr. Julian Cheng, Dr. Thomas Johnson, and Dr. Tom Landecker. My gratitude also goes to Dr. Bruce Veidt at DRAO who provided guidance and made significant contributions to the project.

Financial support for this project was graciously provided by NRC, Dr. Cheng, and Dr. Johnson.

I would also like to thank the staff and contractors at DRAO for their help in this project. Especially Peter Cimbaro, who set up and maintained the simulation software used in this project; as well as Dr. Rick Smegal, Dale Basnett, and Ev Sheehan for their help assembling and testing the prototype.

# Chapter 1

## Introduction

This thesis describes the concept, electrical design, and prototype design for a novel broadband feed antenna. It will present the simulated and experimental results and the analysis of the design's performance. Additional background information on radio astronomy and antenna design will be included to aid the reader in understanding the main body of the thesis.

### 1.1 Rationale

*Somewhere, something incredible is waiting to be known.*

— Carl Sagan (1934 - 1996)

Humankind has an appetite for knowledge about the universe that is rivalled in size only by the universe itself. Astronomy provides a unique opportunity to look into our past and future by looking deep into the skies. As astronomers, radio astronomers, and astrophysicists look to the sky, it falls to scientists and engineers to expand existing tools and discover new tools to expand our understanding of the universe. While conventional astronomers look at the stars with their eyes, and through lenses and digital cameras, radio astronomers explore the microwave radio range. Like most branches of science, astronomy has greatly benefited from improvements in computer technology. For radio astronomy, these improvements included faster digital signal processors, greater data bandwidth, and improved correlators. These technologies open the door for implementing broadband sys-

tems with wider frequency ranges than are currently available. Currently, radio astronomers are interested in the frequency range from 20 MHz to 800 GHz.

These technology improvements have inspired scientists to propose a grand new radio astronomy project called the Square Kilometre Array (SKA), which is on a scale orders of magnitude larger than any current system. The SKA is expected to be a telescope array composed of approximately 250 antennas in phase one and approximately 2500 antennas in phase two<sup>1</sup>.

One of the many technical challenges the SKA project faces is the need for a feed antenna able to efficiently collect signals over a broad frequency range. This project aims to develop a novel feed antenna for a parabolic antenna to fill this gap in the current technology. The proposed design is a log-periodic antenna composed of nested coaxial waveguides. The objective is to design a cost effective broadband feed with similar performance to conventional narrowband feeds. An antenna with these qualities would be ideal for a large antenna array such as the proposed SKA.

A broadband feed antenna offers additional benefits over conventional feed antennas. The broadband feed increases the simultaneous data bandwidth being collected. This means more information can be collected in the same time period. Having only one broadband feed instead of many conventional feeds to cover the same bandwidth eliminates the need to manually or mechanically change the feed on the antenna in order to observe a different frequency range. Finally, since a number of feed antennas are being replaced by one feed antenna, the number of spare parts required to maintain the telescope is reduced.

## **1.2 Background Information**

### **1.2.1 Antenna Design**

An antenna is fundamentally a device that efficiently couples radio waves from free space to a guided wave structure, such as a waveguide or a coaxial cable, and vice versa.

---

<sup>1</sup><http://www.skatelescope.org/>

### 1.2.1.1 Reciprocity Property

Many antennas, such as the design created in this project, have the reciprocity property. This means that at any given frequency the performance of the antenna is identical whether transmitting or receiving signals. This makes designing and testing antennas easier, since it is often easier to use an antenna to transmit and measure its farfield than it is to generate the farfield signal and measure the results. For this reason antenna designers often use terms derived from transmitting practice when an antenna is designed explicitly for receiving.

### 1.2.1.2 Principle of Frequency Scaling

Another interesting property of antennas is that, assuming the antenna is lossless, the performance scales with size. Specifically, the physical size of the antenna is inversely proportional to frequency. For example, let  $f_A(freq)$  be the gain of an arbitrary antenna as a function of frequency. If antenna B is created by physically scaling antenna A by a factor of  $x$ , then the gain for antenna B would ideally be

$$f_B(freq) = f_A(x \cdot freq) . \quad (1.1)$$

Unfortunately, the frequency scaling principle does not always hold precisely in practice because of material or machining constraints that may limit size, thickness, and tolerance. These constraints prevent perfect physical scaling. Further, it is often very difficult and expensive to manufacture small parts with high accuracy. As a result there is a practical limit to the frequency scaling principle when scaling down in size.

### 1.2.1.3 Periodic Antenna Structures

We now introduce the concept of periodic antenna design as it relates to broadband applications. The goal of a periodic antenna design is to achieve a significantly wider bandwidth than conventional antennas provide without compromising the performance of the antenna. A periodic antenna combines multiple conventional antennas together into a single antenna design. Often one antenna is designed, then scaled repeatedly to obtain different frequency ranges. The frequency ranges

overlap slightly such that all the antennas combine to cover a wide continuous frequency range. The frequency range overlap is demonstrated in figure 1.2. A common class of periodic antennas is the log-periodic antenna, in which every iteration of the periodic structure is created by scaling the previous iteration by a fixed scaling factor for the entire antenna. Log-periodic antennas take their name from the exponential growth in the size of the elements and the resulting logarithmic effects on the operating frequency.

The most common periodic antenna design is the log-periodic dipole array, as shown in figure 1.3. Log-periodic dipole arrays are described in detail in [15, pp. 384] and [4, pp. 231]. In a single dipole antenna with length  $l$ , resonance occurs at a wavelength of  $\lambda_c = 2l$ . This means the antenna efficiently radiates at a frequency of

$$f_c = \frac{c}{\lambda_c} = \frac{c}{2l} \quad (1.2)$$

where  $f_c$  and  $\lambda_c$  are the centre frequency and wavelength, respectively, and  $c$  is the speed of light. In a log-periodic dipole antenna, a number of dipoles are combined together in parallel, each with different resonant frequencies, in order to achieve a larger overall operating bandwidth. As discussed in [23, ch. 13], log-periodic antenna structures produce farfields with poor symmetry, and as a result are inefficient when used as a feed for a parabolic antenna.

#### 1.2.1.4 Parabolic Antenna

A parabolic antenna exploits the geometry of a parabola to collect a large amount of incoming energy and direct it to a feed antenna. The large area of the parabolic antenna increases the energy collected from free space and allows weaker signals to be detected. Additionally, from the Fourier transform, we know that large apertures produce narrow farfield radiation patterns. Specifically the width of the farfield radiation pattern is proportional to  $\lambda/D$ , where  $\lambda$  is the wavelength of the signal and  $D$  is the diameter of the parabolic antenna.

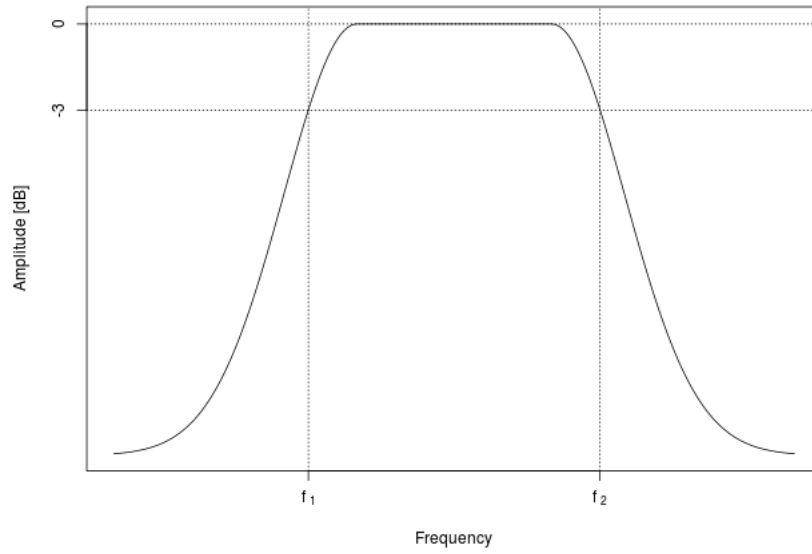


**Figure 1.1:** Operating Frequency Band of One Antenna

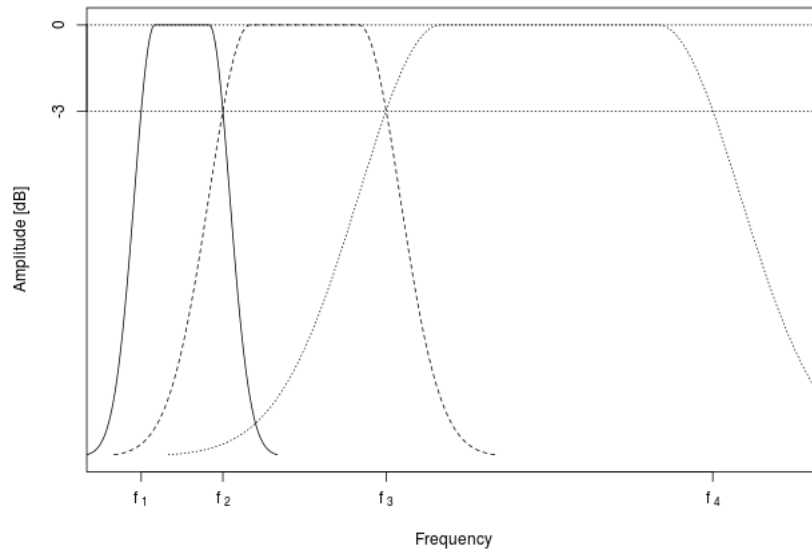


**Figure 1.2:** Operating Frequency Bands of Multiple Antennas

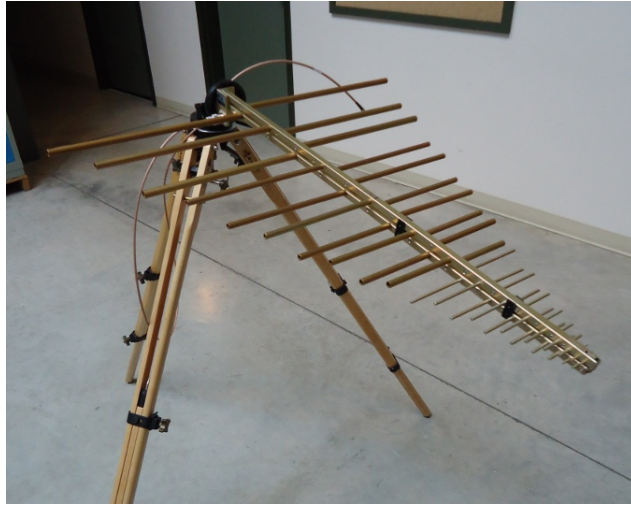


*Figure 1.3: Log-Periodic Dipole Array*

#### **1.2.1.5 Feed Antenna**

A feed antenna is designed to work with a parabolic antenna of a specific focal-length-to-diameter ( $f/D$ ) ratio. The feed antenna should ideally deliver power uniformly to the entire surface of the parabolic antenna while delivering no power outside the parabolic antenna. However this uniform step power distribution is impossible to achieve in practice. The feed antenna is located with its phase centre at the focal point of the parabolic antenna to collect the maximum amount of the incoming signal, as seen in figure 1.4. Ideally, the phase centre of an antenna should be frequency independent, although this is also often not achieved in practice.

#### **1.2.2 Radio Astronomy**

Radio astronomy is the science of studying the universe through radio waves. One of the major limitations of ground based observations is that the radio waves must be able to travel through the earth's atmosphere. As shown in figure 1.5, there are two frequency windows of low atmospheric electromagnetic opacity. One of these windows falls in the optical frequency range, which allows for optical viewing of the stars and other celestial objects from the surface of the earth. The second window of low atmospheric opacity is the frequency range used for radio astron-

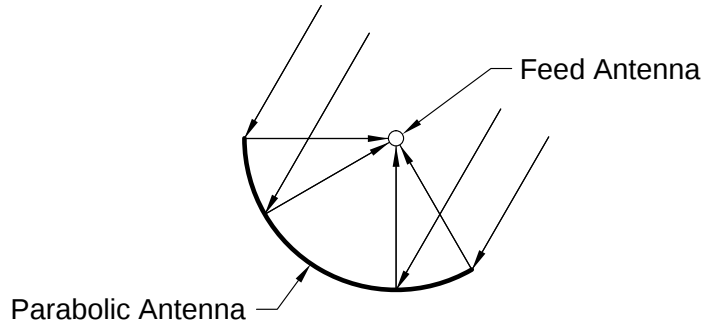


**Figure 1.4:** *Parabolic Antenna and Feed Antenna*

omy. This window allows for the use of ground based instruments, which are relatively low cost and easy to construct and maintain compared to satellite based instruments. For observations in frequency ranges with high atmospheric opacity, such as the infrared, ultraviolet, and x-ray frequency ranges, satellite based instruments are used. An example of an infrared instrument is the Infrared Astronomical Satellite (IRAS) [3] and an example of an x-ray/ultraviolet instrument is the Swift mission [2].

### **1.2.2.1 Method of Radio Astronomy**

The conventional method of radio astronomy is to use a parabolic antenna to reflect the incoming signal to a feed antenna at the focal point of the dish. The feed antenna collects the signal and couples it to a low noise amplifier (LNA) via a coaxial cable. The cable carries the signal from the feed antenna through one or more stages of LNAs to a correlator. The output of the correlator is digital and is stored for further processing and analysis.

Radio astronomy is hindered by the fact that the desired information, or signal, is very weak and much lower than background noise from natural phenomena and man-made noise sources [14, ch. 1]. To compensate for this, signal measurements are taken from the same point in space for a long period of time, 12 hours for example, and the resulting data is correlated such that the noise is averaged out and what remains is the desired signal. This procedure assumes that all the noise sources

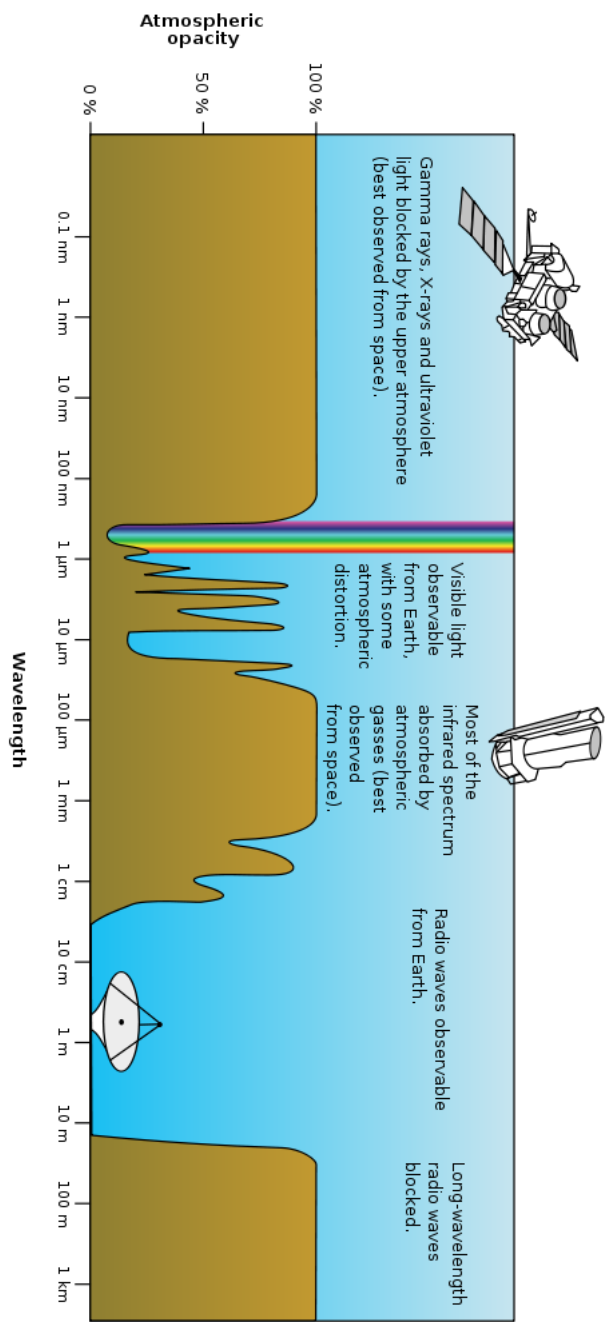


(Image Credit: <http://www.nasa.gov/multimedia/imagegallery/>)

**Figure 1.5: Atmospheric Electromagnetic Opacity**

are zero mean, such that the expected value is zero over a long time average. Not all noise sources are zero mean sources. For example, terrestrial interference from cell towers has power output based on usage, and may not be zero mean. This noise would not be removed by a simple correlator. This is the reason that radio observatories are built in regions that have low human electromagnetic activities. For example, the SKA project is to be built in Southern Africa, New Zealand, and Australia. These regions have very low levels of terrestrial noise.

### **1.2.2.2 Radio Interferometry**

Radio interferometry is a family of techniques used to combine signals from multiple antennas to improve antenna performance. The idea being that the resulting signal has properties that can be used to gain information about the signal source. One of the common methods of radio interferometry is aperture synthesis.

### **1.2.2.3 Aperture Synthesis**

For a single parabolic antenna, the angular resolution is determined by the diameter of the antenna dish. In 1946, a technique called aperture synthesis was developed by Sir Martin Ryle [15, p. 520]. Aperture synthesis allows an array of small antennas to be used together to yield the same performance as a single much larger antenna. In this way, a larger aperture is synthesized through computation, thus the technique's name. The additional antenna dish surface area in the array will collect more energy which allows weaker signals to be detected. More importantly, the angular resolution can be significantly improved by the larger synthesized aperture.

If an aperture synthesis array records data over time, the orientation of the array will change relative to the object being observed as the earth rotates. This change in orientation allows the array to act as additional antenna locations, resulting in additional observations to apply aperture synthesis to. This is why observations for aperture synthesis arrays are often taken over a period of 12 hours as this is the longest observational period that will produce unique observations.

The largest aperture synthesis array telescope in use today is the Expanded Very Large Array (EVLA) in New Mexico. The EVLA, which uses 27 steerable

25 metre antennas<sup>2</sup>, is an upgrade to the 30 year old Very Large Array (VLA). Part of the upgrade was a new correlator that was designed and built at the Dominion Radio Astrophysical Observatory (DRAO).

#### **1.2.2.4 Very Long Baseline Interferometry**

A more advanced form of radio interferometry is very long baseline interferometry (VLBI). VLBI was developed in 1967 by Canadian researchers working at DRAO, the National Research Council of Canada (NRC), and at various universities. VLBI uses multiple antennas, often hundred of kilometres apart, to collect data. The data is then correlated using high precision clocks to synchronize the data. The first successful VLBI observation was made using the 26 metre telescope at DRAO located outside Penticton, British Columbia and the 46 metre telescope at the Algonquin Radio Observatory (ARO) located in Algonquin Provincial Park, Ontario<sup>3</sup>. Both antennas were used to make simultaneous observations. The observed signals from each site were sampled by separate atomic clocks and recorded onto magnetic tape. The magnetic tape and atomic clock from DRAO were taken by train to ARO where the DRAO data and ARO data were synchronized using their two atomic clocks. By combining the two sets of observation data with an accurate time base, very high angular resolution was obtained.

#### **1.2.3 Maxwell's Equations**

Maxwell's equations are fundamental to all applications of electromagnetic theory. In 1865, James Clerk Maxwell (1831 – 1879) published the paper “A Dynamical Theory of the Electromagnetic Field” [19], which contained 20 formulae that are now considered to be a corner stone of electromagnetic theory. Maxwell's original 20 equations were later reduced to the familiar four vector equation form by Oliver Heaviside (1850 – 1925) [21, pp. 108-112] and concurrently by Willard Gibbs (1839 – 1903) and Heinrich Hertz (1857 – 1894) [8, p. 194]. Because of these concurrent discoveries, Maxwell's equations are also known as the Maxwell-Heaviside equations, the Hertz-Heaviside equations, or the Maxwell-Hertz equations.

---

<sup>2</sup><http://www.nrao.edu/index.php/about/facilities/vlaevla>

<sup>3</sup><http://www.nrc-cnrc.gc.ca/eng/facilities/hia/radio-astrophysical/highlights-of-drao.html>

The vector form of Maxwell's can be written in either integral or differential form. The differential form is

$$\nabla \times \bar{E} = -\frac{\partial \bar{B}}{\partial t} \quad (1.3)$$

$$\nabla \times \bar{H} = \frac{\partial \bar{D}}{\partial t} + \bar{J} \quad (1.4)$$

$$\nabla \cdot \bar{D} = \rho \quad (1.5)$$

$$\nabla \cdot \bar{B} = 0 \quad (1.6)$$

where

$\bar{E}$  is the electric field intensity vector, in V/m,

$\bar{H}$  is the magnetic field intensity vector, in A/m,

$\bar{D}$  is the electric flux density vector, in Coul/m<sup>2</sup>,

$\bar{B}$  is the magnetic flux density vector, in Wb/m<sup>2</sup>,

$\bar{J}$  is the conduction current density, in A/m<sup>2</sup>,

$\rho$  is the electric charge density, in Coul/m<sup>3</sup>.

### 1.2.3.1 Boundary Conditions

A boundary condition is a constraint on the electromagnetic condition that occurs at the boundary between two materials. These conditions create simple rules that electromagnetic fields must follow which are useful in interpreting Maxwell's equations.

An important boundary condition for metal waveguides is the interface with metal walls. For ease of calculation, we assume that the conductive walls are perfect electric conductors, also known as electric walls. An electric wall has infinite skin depth and no conductive losses ( $\sigma \rightarrow \infty$ ). With these assumptions, equations 1.3 to 1.6 imply that

$$\hat{n} \cdot \bar{D} = \rho_s \quad (1.7)$$

$$\hat{n} \cdot \bar{B} = 0 \quad (1.8)$$

$$\hat{n} \times \bar{E} = 0 \quad (1.9)$$

$$\hat{n} \times \bar{H} = \bar{J}_s \quad (1.10)$$

where

$\rho_s$  is the electric surface charge density, in Coul/m<sup>2</sup>,

$\bar{J}_s$  is the electric surface current density, in A/m<sup>2</sup>.

For this project, equation 1.9 is relevant and states that the electric field must be strictly normal to conducting walls at the conducting walls. This result becomes especially significant when considering the mode cutoff frequencies of a waveguide.

## 1.2.4 Waveguides

Waveguide antennas have very low conduction losses because of their large surface area [24, pp. 154]. This property is very useful for radio astronomy applications which are very sensitive to noise and losses.

### 1.2.4.1 Waveguide Modes and Cutoff frequency

The electromagnetic field inside a waveguide is a superposition of multiple attenuating and propagating waveguide modes. These modes correspond to solutions for Maxwell's equations. There are three types of waveguide modes:

**Transverse Electric (TE) Modes** characterized by no electric field component in the direction of propagation

**Transverse Magnetic (TM) Modes** characterized by no magnetic field component in the direction of propagation

**Transverse Electromagnetic (TEM) Modes** characterized by no electric or magnetic field component in the direction of propagation

Depending on the waveguide shape and dimensions, there may be multiple possible TE and TM modes, each with its own cutoff frequency. The cutoff frequency is the frequency above which the propagation constant is real and the wave can propagate without attenuation assuming ideal conductors and loss-free dielectric materials. Losses caused by either the conductors or the dielectric materials will cause attenuation regardless of whether or not the mode is cutoff. The TEM mode has no cutoff frequency and will not attenuate at any frequency, but will only propagate in waveguides with at least two conductors.

The cutoff frequencies for a coaxial waveguide can be found by solving Maxwell's equations for the waveguide dimensions and applying boundary conditions. The solutions to Maxwell's equations also provide expressions for the magnetic and electric fields inside the waveguide for each mode.

For this project, we only need to consider TE modes, since they have much lower cutoff frequencies than TM modes for the structure we are considering. The TEM mode will be suppressed through the design of the excitation structure. In this thesis, only circularly symmetric coaxial metal waveguides are discussed. Elliptical waveguide structures are discussed in [18, pp. 80]. For a circularly symmetric coaxial metal waveguide, the family of solutions to Maxwell's equations for TE modes are [24, pp. 128]

$$E_\phi = \frac{j\omega\mu}{k_c} [A \sin(n\phi) + B \cos(n\phi)] [CJ'_n(k_c\rho) + DY'_n(k_c\rho)] e^{-j\beta z} \quad (1.11)$$

$$H_\phi = [A \sin(n\phi) + B \cos(n\phi)] [CJ'_n(k_c\rho) + DY'_n(k_c\rho)] e^{-j\beta z} \quad (1.12)$$

where  $A$ ,  $B$ ,  $C$ , and  $D$  are constants,  $k_c$  is the cutoff wave number, and  $J'_n$  and  $Y'_n$  are the  $n$ th order of the Bessel functions of the first kind and second kind, respectively.

Additionally,

$$J'_n(k_c a) Y'_n(k_c b) = J'_n(k_c b) Y'_n(k_c a) \quad (1.13)$$

where  $a$  and  $b$  are the inner conductor radius and the outer conductor radius. The functions for the exact values for cutoff wavelength can be found in [18, pp. 72-80]. The approximate cutoff frequencies are

$$\text{TE}_{m1}: \lambda_{ci} \approx \frac{\pi(a+b)}{m} \quad \text{for } m = 1, 2, 3, \dots \quad (1.14)$$

$$\text{TE}_{mn}: \lambda_{ci} \approx \frac{2(a-b)}{(n-1)} \quad \text{for } n = 2, 3, 4, \dots \quad (1.15)$$

$$\text{TM}_{mn}: \lambda_{ci} \approx \frac{2(a-b)}{n} \quad \text{for } n = 1, 2, 3, \dots \quad (1.16)$$

We define the waveguide ratio,  $\zeta$ , as the ratio of the outer conductor radius to the inner conductor radius,  $b/a$ . For the TE modes in a coaxial waveguide, a very good approximation of cutoff wavelength is given by [18, pp. 77]

$$\lambda_{ci}'' = \frac{2\pi}{(\zeta + 1)x'_{m1}}(a+b). \quad (1.17)$$

The values for  $x'_{m1}$  are given in table 1.1.

**Table 1.1:** Values of  $x'_{m1}$  for TE Modes in Coaxial Waveguides. From [18]

$\zeta$	$x'_{m1}$		
	11	21	31
1.0	2.000	4.000	6.000
1.1	2.001	4.001	6.002
1.2	2.002	4.006	6.008
1.3	2.006	4.011	6.012
1.4	2.009	4.015	6.017
1.5	2.013	4.020	6.018
1.6	2.018	4.025	6.011
1.8	2.024	4.026	5.986
2.0	2.031	4.023	5.937
2.5	2.048	3.980	5.751
3.0	2.056	3.908	5.552
3.5	2.057	3.834	5.382
4.0	2.055	3.760	5.240

For reasons that will be explained in chapter 5,  $\zeta$  is set to 1.8 resulting in the following cutoff wavelengths:

$$\text{TEM: } \lambda_c = \infty \quad (1.18)$$

$$\text{TE}_{11}: \lambda_c = \frac{2\pi}{(2.8)2.024} (a+b) \quad (1.19)$$

$$\text{TE}_{21}: \lambda_c = \frac{2\pi}{(2.8)4.026} (a+b) \quad (1.20)$$

$$\text{TE}_{31}: \lambda_c = \frac{2\pi}{(2.8)5.986} (a+b) \quad (1.21)$$

As before,  $a$  is the inner waveguide wall radius,  $b$  is the outer waveguide radius.

#### 1.2.4.2 Mode Suppression and Decoupling

For this project, the desired mode is  $\text{TE}_{11}$  because it is known to produce the best farfield patterns. The excitation structure needed to generate the  $\text{TE}_{11}$  mode in a coaxial waveguide will theoretically achieve suppression of both the TEM and  $\text{TE}_{21}$  modes. This suppression is demonstrated in figure 1.6 which shows that the electric field of the  $\text{TE}_{11}$  mode is incompatible with the electric field of the TEM and  $\text{TE}_{21}$  modes, and cannot be excited simultaneously. This natural mode suppression is very convenient, since this allows a coaxial waveguide to operate from the cutoff frequency of the  $\text{TE}_{11}$  mode to the cutoff frequency of the  $\text{TE}_{31}$  mode. As can be seen from equation 1.14, this is a bandwidth ratio of approximately 3:1.

#### 1.2.5 Farfield

The farfield of an antenna is the electromagnetic field power taken at an arbitrarily large distance from the antenna such that the field distribution can be represented only in terms of  $\phi$  and  $\theta$  and not in terms of the distance from the antenna. The distance from the antenna required for the electromagnetic field to be considered the farfield is dependant on the size of the antenna. For  $D$  being the largest dimension of an antenna, if the antenna is electrically small ( $D < \lambda/2$ ) the farfield begins

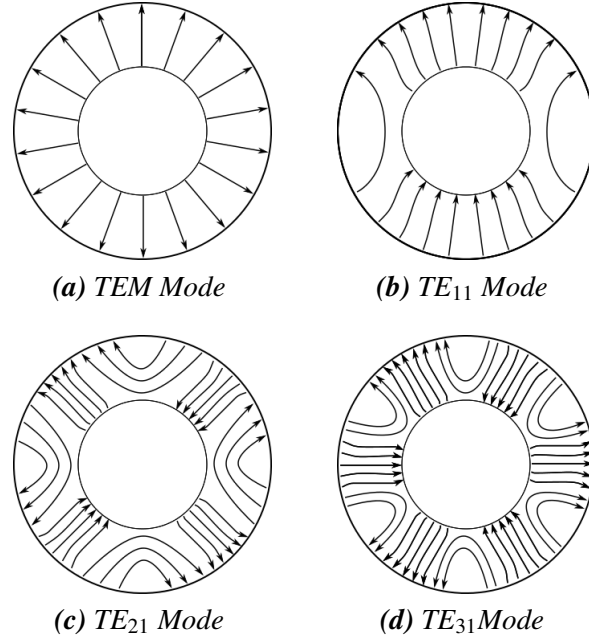


**Figure 1.6:** Electric Fields of Modes in a Circular Coaxial Waveguide

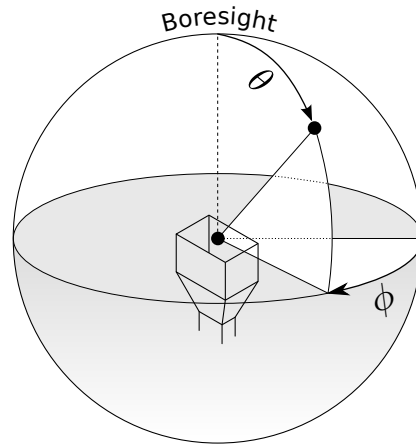
at a distance of  $2\lambda$  from the antenna. If the antenna is electrically large ( $D > \lambda/2$ ), the farfield begins at the Fraunhofer distance. The farfield pattern is one of the performance criteria considered in this project.

$$\text{Fraunhofer Distance: } d_f = \frac{2D^2}{\lambda} \quad (1.22)$$

Given  $d_f \gg D$  and  $d_f \gg \lambda$ .

### 1.2.5.1 Antenna Coordinate System

Farfield data is represented in the antenna coordinate system. The antenna coordinate system is similar to the horizontal coordinate system used in astronomy. Figure 1.7 shows the coordinate system. The coordinate system is oriented such that the antenna is located at the origin of the system and the boresight of the farfield pattern is located at  $\theta = 0^\circ$ .



Original Image: TWCarlson / Wikimedia Commons / CC-BY-SA 3.0

*Figure 1.7: Farfield Coordinate System*

### 1.2.5.2 Polarization

The term “polarization” refers to the description of a wave as it propagates through space. If the wave is linearly polarized, it oscillates in one direction while travelling in an orthogonal direction. Figure 1.8 shows two linearly polarized waves, one with vertical polarization and the other with horizontal polarization. In antenna design, the definitions of the vertical and horizontal polarizations are the choice of the designer, although the E-plane is normally aligned with either the vertical or horizontal polarization. If the wave oscillates in both the vertical and horizontal directions and there is a phase difference between the vertical and horizontal oscillations, the wave is said to be elliptically polarized because the electric field vector traces an ellipse as it travels through space. If the vertical and horizontal oscillations have the same amplitude and are  $90^\circ$  out of phase, the electric field vector traces out a circle as it travels through space and the wave is said to be circularly polarized as shown in figure 1.9.

Once the reference polarization of a wave is defined, the wave can be broken into two components: the co-polarization component and cross-polarization component. Similarly, the farfield pattern can be broken down into these two components. The definitions for co-polarization and cross-polarization are ambiguous for linearly and elliptically polarized waves [4, pp. 219]. There are a number of

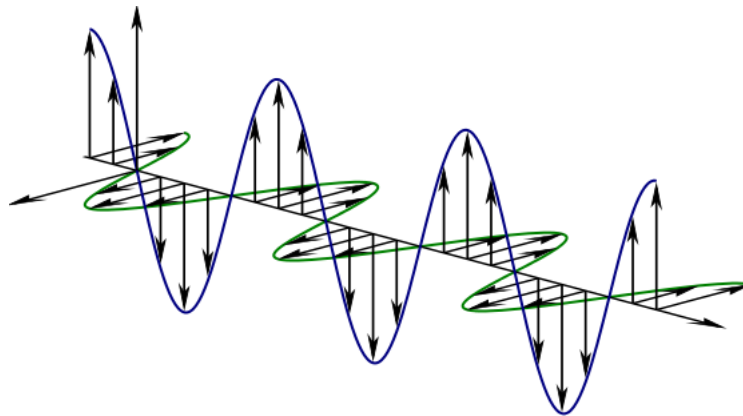


**Figure 1.8:** *Linearly Polarized Waves*

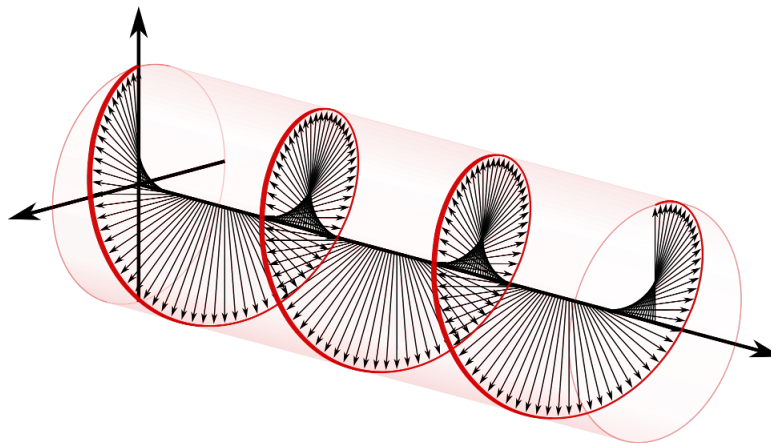
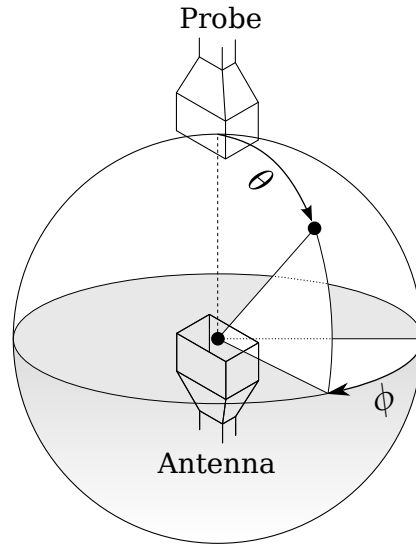


**Figure 1.9:** *Circularly Polarized Wave*

definitions for the co-polarization and cross-polarization components. One of the most common definitions is Ludwig's third definition [4, 17, pp. 219], which corresponds to the co-polarization and cross-polarization components of the farfield generated when an antenna is tested in the conventional way. In order to obtain measurements that use Ludwig's third definition two series of measurements are required. For the first polarization, a probe is placed at the boresight of the antenna being tested then held stationary as shown in figure 1.10. The antenna is then held at a constant angle  $\phi$  while being rotated in the  $\theta$  direction. This process is re-

peated for multiple values of  $\phi$  to collect multiple cross-sections of the radiation pattern until all the required measurements are taken. To measure the second polarization, all that is required is to rotate the probe by  $90^\circ$  and repeat the same testing procedure as before.



Original Image: TWCarlson / Wikimedia Commons / CC-BY-SA 3.0

**Figure 1.10:** Test Setup for Ludwig's Third Definition of Polarization

### 1.2.6 Return Loss

Return loss (RL) is an important measure of performance used in this project. In general terms it is a measure of the power reflected as a result of the mismatch between an electrical system and its electrical load. In the context of this project, this can also mean a mismatch between different components of the design or between the antenna and free space. The formal definition of return loss is given in terms of the reflection coefficient ( $\Gamma$ ):

$$RL = -20 \log |\Gamma| \quad \text{dB} \quad (1.23)$$

The reflection coefficient can be defined using the ratio of the reflected voltage wave ( $V_0^-$ ) and the incidental voltage waves ( $V_0^+$ ):

$$\Gamma = \frac{V_0^-}{V_0^+} \quad (1.24)$$

Another way to define the reflection coefficient is to use the characteristic impedance of the transmission line ( $Z_0$ ) and the impedance of the load ( $Z_L$ ):

$$\Gamma = \frac{Z_L - Z_0}{Z_L + Z_0} \quad (1.25)$$

This second definition shows the relation between the impedance mismatch and the return loss. A large return loss is desirable as it indicates good impedance matching in the design.

## Chapter 2

# Related Work

This chapter describes the existing research related to this design. It will discuss the current designs for feed antennas with a brief summary of the benefits and shortcoming of each design.

### 2.1 Coaxial Waveguide

A significant amount of theoretical work has been done on the radiating properties of coaxial waveguides. Most work shows that although the coaxial waveguides have good farfield patterns [16], they suffer from an input mismatch with free space. A number of approaches have been used to solve this problem. Bird showed that the mismatch could be addressed by extending the centre conductor and adding a flat flange to the aperture of the antenna [5, 6]. The use of irises inside the waveguide to match to free space is discussed in [11] and [25, pp. 211]. The technique of adding a quarter wavelength choke to the outside of the waveguide to improve the farfield pattern is demonstrated in [13].

Work has also been done on nested waveguides structures. An antenna that has three separate narrowbands is analyzed in [27]. This antenna uses multiple independent excitation structures and a separate set of quarter-wave chokes for each band. An ultra-wideband antenna with a bandwidth ratio of 70:1 is proposed in [12]. This design achieved good theoretical return loss, however [12] makes no attempt to predict the farfield patterns. [26] refines this design and gives both

analytic and experimental results for the return loss and the farfield patterns. The design given in [26] achieves a bandwidth ratio of 60:1 with good return loss. This design's weaknesses are the lack of a common excitation structure and the wide farfield patterns that vary with frequency.

## 2.2 Circular Waveguide Antenna

A common feed antenna used for radio astronomy is described in [30]. This antenna is composed of a single circular waveguide with a number of small chokes located approximately 0.4 wavelengths behind the aperture. Over a narrow bandwidth, the farfield patterns for the antenna have good symmetry, low backlobes, and most notably, a large flat region near the boresight. The desired bandwidth of 60 MHz at 2695 MHz was achieved with a return loss above 25 dB and a 10 dB beamwidth of  $159.3^\circ$ . This feed antenna is commonly used with deep parabolic antennas ( $f/D < 0.35$ ), including the 26 m radio telescope located at DRAO.

## 2.3 Corrugated Feed Horn Antenna

The corrugated feed horn is a waveguide antenna design with very good farfield symmetry and high aperture efficiency [15, pp. 341-343]. The only shortcoming of this design is the limited bandwidth. The best feed horn antennas have at most a continuous bandwidth ratio of 2.2:1 [4, pp. 889]. A thorough discussion of corrugated feed horns can be found in [23, ch. 9].

## 2.4 Eleven Antenna

The Eleven Antenna is an experimental broadband feed antenna designed by Per-Simon Kildal and his team at Chalmers University of Technology in Sweden [22, 33]. It uses a number of dipole antennas in a log-periodic array to achieve a wide bandwidth. As shown in figure 2.1, the antenna takes the form of four wings located over a ground plane. The eleven antenna exhibits a 10 dB half beamwidth of  $55^\circ \pm 10^\circ$  over the operating band [22, 32]. The return loss of the initial antenna initial design was marginal, as high as 5 dB at some frequencies [22]. This was improved to 10 dB across most of the operating bandwidth in later iterations of the design

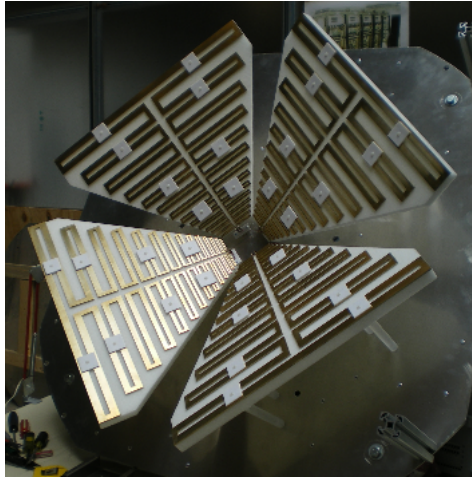


*Figure 2.1: An Eleven Antenna Built at DRAO*

[34]. The Eleven Antenna is likely to exhibit a significant problem with conductor loss because of the series configuration of the dipoles which results in very long signal paths. This would be especially true for low frequencies that operate in the outer regions of the antenna. In this project we hope to remedy the issues with conductor loss and return loss.

## **2.5 Log-Periodic Spiral Antenna**

Another periodic antenna design is the log-periodic spiral antenna. A log-periodic spiral antenna is a wideband antenna created by cutting a zig-zag pattern out of sheet metal. This method of creating antennas benefits greatly from low cost and ease of construction. Figure 2.2 shows a log-periodic spiral antenna that was built by a team at the Dominion Astrophysical Observatory (DAO) in collaboration with the University of Victoria (UVic). As described in [20], the farfield patterns of this antenna have good main lobes with the 10 dB half beamwidth around  $\theta = \pm 60^\circ$ . The side lobes for this antenna are poor, reaching as high as -5 dB relative to the power at the boresight. A bandwidth ratio of 6:1 was achieved with a return loss of approximately 5 dB. The shortcomings of this design are the poor side lobes and the low return loss when the bandwidth is extended beyond a ratio of 6:1.

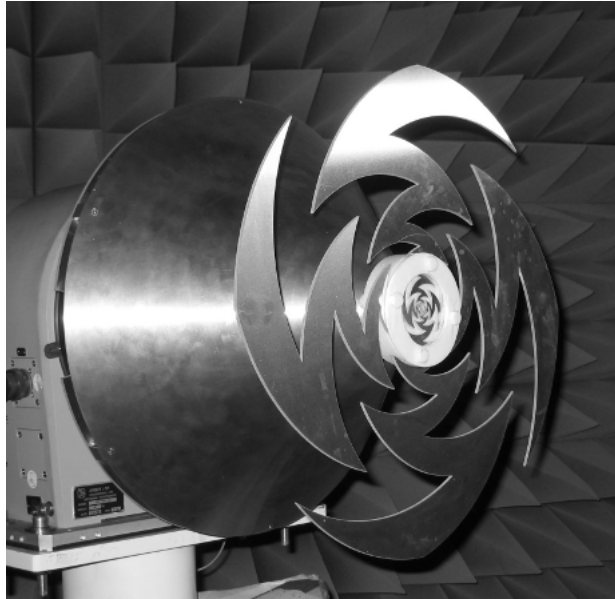


*Figure 2.2: Log-Periodic Spiral Antenna Designed and Built at DAO*

## Chapter 3

# Tools Used

A number of computer tools were used in this project. They will be briefly described in this chapter.

### 3.1 Computer Simulation Technology

Computer Simulation Technology is a company that produces the electromagnetic simulation software “Computer Simulation Technology (CST) Studio Suite”. In this thesis, as well as in industry, this software is referred to simply by its acronym: CST. CST includes multiple modules designed for an array of electromagnetic applications. Each module supports multiple solvers and grid configurations. Each solver applies a different computation method to the model. For this project, the Microwave Studio (MWS) module of CST with hexahedral gridding was used. The MWS module is designed to simulate microwave and radio frequency components in three dimensions.

#### 3.1.1 Transient Solver

At the time of the project, DRAO had a license for only the transient solver which uses the finite integration technique (FIT) method [1]. The FIT method is based on the integral form of Maxwell’s equations and is able to maintain the physical properties of an electric field while using a discrete spatial system [29].

### **3.1.2 Frequency Analysis**

To obtain the power spectral density (PSD) and return loss, CST performs a fast Fourier transformation (FFT) on the time-domain data generated by the simulator. The calculated PSD is compared to the PSD of the source in order to obtain the S-parameter results.

### **3.1.3 Hexahedral Gridding**

CST offers a number of grid configurations. At the time of the project DRAO had a license for only the hexahedral gridding option. Normally using a hexahedral grid to represent a circular model would lead to staircasing, which is the representation of a curved object using small steps. CST solves this problem by using a proprietary algorithm call the “perfect boundary approximation” [29].

### **3.1.4 Parameter Sweeps and Optimization**

One advantage of using simulators is that they allow parameters to be easily changed. The effects of these changes can be analyzed to gain insight into the simulated model. There are two classes of operations used to analyze the effects of altering parameters: sweeps and optimizations. CST includes built-in tools for both parameter sweeps and optimizations.

In a parameter sweep, the user sets a number of fixed values for each parameter. Often these fixed values are linearly distributed over a range, but this is not required. A simulation is then run for every permutation of the parameters and the results are recorded. The recorded results can be compared side by side and then analyzed by the user. Alternatively, the user can create a goal function and have CST calculate the goal values and plot them against the parameters. This procedure can result in a large number of simulations if multiple parameters are swept simultaneously.

In contrast, optimization tries to iterate to the optimal solution using various algorithms. In an optimization, an initial value and range are set for each parameter and one or more goal functions are defined. The simulator then iterates with different values for the parameters in an attempt to have the goal function converge to a minimum. A class of algorithms called local optimization algorithms converge

to a local minimum near the initial value. This means that the performance of the algorithm is very dependent on the choice of initial values. A second class of algorithms are global optimization algorithms, which find the global minimum within the defined parameter range. CST MWS has five optimization algorithms listed in table 3.1.

**Table 3.1:** Comparison of Optimization Algorithms Used by CST

	Scope	Notes
Interpolated Quasi-Newton	Local	<ul style="list-style-type: none"> <li>• Fast but reduced accuracy because of interpolation</li> </ul>
Classic Powell	Local	<ul style="list-style-type: none"> <li>• Slower but more accurate than Newton</li> <li>• Uses no interpolation</li> </ul>
Nelder Mead Simplex	Local	<ul style="list-style-type: none"> <li>• Good for many optimization parameters</li> <li>• Uses no interpolation</li> </ul>
Genetic	Global	<ul style="list-style-type: none"> <li>• Mimics the process of natural selection</li> </ul>
Particle Swarm	Global	<ul style="list-style-type: none"> <li>• Uses multiple candidate solutions</li> <li>• Allows for few assumptions about problem</li> </ul>

For this project, the Interpolated Quasi-Newton optimizer was used since it is the default optimizer for CST. The Interpolated Quasi-Newton optimizer worked well because parameter sweeps were run prior to the optimization to find a good set of initial values for the optimization parameters. However, due to the number of parameters in the full model that need to be optimized, either the Nelder Mead Simplex or Particle Swarm algorithm may be more efficient than the Interpolated Quasi-Newton algorithm for optimizing the full model.

### 3.1.5 Time vs Accuracy Trade-Off

The primary limitation of the CST simulator is the time it takes to perform a simulation. The amount of time the simulation requires is directly proportional to the number of grid points in the simulation which is affected by the size of the model, the largest frequency simulated, and the grid density settings specified by the user. Simulation time can be reduced by decreasing the grid density and by limiting the frequency range. The trade-off is that grid density determines the result stability. Result stability is how consistent the results are with minor changes to grid density.

As the grid density is increased, the simulation results converge to a stable set of results. It is assumed that this set of results is an accurate approximation of how the model would perform experimentally. In other words, it is assumed that the simulation result accuracy increases with grid density. This assumption should be tested, especially for new antenna designs, such as the one developed in this thesis.

It is not always optimal to have high grid density because of the increased time required to perform simulations. A balance must be struck between run time and simulation result accuracy. Simulation time is particularly important when performing optimizations. Depending on the number of physical variables in the model, it may require hundreds of simulation runs to perform an optimization.

### **3.1.6 Simulation Limitations of CST**

Since CST is a simulator, there is a fundamental limitations on how well it can model real world phenomena. To account for this, all simulation results that were inconsistent with the expected results were closely examined and justified to see if they were accurate or were artifacts created by the simulator.

### **3.1.7 Assumptions Adopted to Reduce Simulation Time**

The design discussed in this thesis is a nested waveguide structure and it is assumed that only the adjacent waveguides will affect the results of the excited waveguide. This assumption means that only part of the antenna needs be simulated instead of the whole antenna which reduces the simulation time. Furthermore, since antenna performance scales with frequency, the performance of all typical waveguides can be determined from one simulation. Similarly, all typical waveguides can be optimized with one optimization run. The outermost waveguide requires separate simulations because there is no waveguide beyond it. A similar argument applies to the innermost waveguide.

Field symmetry can also be exploited to reduce simulation time. When defining symmetries, a few conditions must be met. Primarily, the electromagnetic field must exhibit symmetry. Secondly, CST will not let two excitation sources be on different sides of a symmetry plane. To verify a symmetry assumption is correct for a new model, a simulation should be run twice, once with the symmetry condition

and once without the symmetry condition. If the results from these two simulations agree, then the symmetry assumption being tested is valid. CST offers two forms of symmetry, E-symmetry and H-symmetry. E-symmetry is defined as having no electric field component tangential to the plane of symmetry, and similarly, H-symmetry is defined as having no magnetic field component tangential to the plane of symmetry. For every symmetry condition used, the simulation time can be reduced by approximately 50%.

Assumptions were also made in CST about the material properties of the model. It was assumed that all metals were ideal conductors and that the background material was a vacuum. This saves the simulator from having to calculate material losses. The ramifications of these material assumptions are discussed in chapter 10.

### **3.1.8 Blackbox Simulator**

CST is proprietary software and should be treated as a black box simulator. This means that the algorithms, assumptions, and approximations that the simulator makes are trade secrets and unknown to the user. As a result it is difficult to verify the results of the simulator algebraically. To account for this, a physical prototype must be constructed and tested in order to validate the simulation model.

## **3.2 Solidworks**

Solidworks was used to convert the electrical design into a physically realizable design to be constructed. Solidworks is the industry standard for designing industry parts and the preferred format for transferring designs to the machinist for fabrication.

## **3.3 AutoCAD / Gimp / Inkscape**

Three pieces of software were used to create figures for this report: AutoCAD, Gimp, and Inkscape. AutoCAD is the industry standard for 2D drawings. Gimp and Inkscape are free image editors that were used to create graphics.

### **3.4 Matlab / Octave / Excel**

Matlab is a commonly used program for manipulating large data sets. The name is an abbreviation for matrix laboratory. Octave is a open source clone of Matlab. It was used in place of Matlab when a computer with a license for Matlab was unavailable. Excel is a standard spreadsheet program with a full Visual Basic for Applications (VBA) backbone for programming. In this project, these programs were all used to parse, analyze, and plot simulated and experimental data.

### **3.5 R**

R is a scripting language primarily used for statistical computer and graphics [10]. For this project, R was used to produce high quality graphs.

## Chapter 4

# Design Goals

### 4.1 Overall Design Goals

As discussed in section 1.1, the goal of this project is to design a feed antenna that has much wider bandwidth than conventional feed antennas without a significant loss in performance. The target bandwidth ratio for this project is 10:1 with a frequency range from 1 GHz – 10 GHz. Over the bandwidth of the antenna, the goal for the return loss ( $RL$ ) is to be greater than 10 dB. In terms of material loss, no explicit goal was set, however the design should attempt to minimize all sources of loss. The overall design goals are summarized in table 4.1.

*Table 4.1: Design Goals for the Overall Antenna*

Frequency Range	1 GHz – 10 GHz
Bandwidth Ratio	10:1
Return Loss ( $RL$ )	> 10 dB

### 4.2 Waveguide Coupling Design Goals

As described later in chapter 5, a feed antenna consisting of a nested coaxial waveguide structure is proposed. The design has a common excitation structure that couples the signal into each waveguide. Each waveguide is designed to operate over a specific frequency range. To facilitate this, the excitation structure should

have frequency selective coupling to each waveguide. The specifications for the coupling to a waveguide is summarized in table 4.2. In the table,  $f_{min}$  and  $f_{max}$  delimit the frequency range of the waveguide. Inside this frequency range, coupling to other waveguides should be minimized.

**Table 4.2:** Coupling Design Goals

	$f < f_{min}$	$f_{min} < f < f_{max}$	$f_{max} < f$
Return Loss ( $RL$ )	> 10 dB		
Coupling to Waveguides	< -10 dB	0 dB	< -10 dB
Coupling to Other Waveguides		< -10 dB	

### 4.3 Farfield Design Goals

The desired beamwidth of a feed antenna is determined by the focal-length-to-diameter ( $f/D$ ) ratio of the parabolic antenna the feed antenna will used with. For this design the  $f/D$  ratio was 0.4 and the angle subtended by the parabolic antenna seen from the focal point was  $120^\circ$ . As a result the goal for the 10 dB half beamwidth was set to  $60^\circ$ . The angular resolution of a parabolic antenna is determined by the Fourier transform of the signal illumination of the surface on the antenna [7, pp. 407]. Ideally, the illumination should have equal amplitude across the parabolic antenna and zero amplitude elsewhere. This is can be represented as a rectangular function. The Fourier transform of a rectangular function produces a sinc function in the farfield pattern of the parabolic antenna. This farfield pattern has small side lobes and a very small angular resolution.

To produce even illumination of the dish, the feed antenna needs to have a rectangular farfield pattern. In practice, a rectangular farfield pattern cannot be produced. Instead an achievable goal for the farfield pattern is a bell-like shape with the parameters given in table 4.3.

After simulating different designs for the antenna it was found that the farfield pattern specifications could not be met without compromising the bandwidth. A better compromise between farfield patterns and bandwidth was achieved by relaxing the tolerances to  $\pm 4$  dB as shown in table 4.4.

**Table 4.3:** Design Goals for the Farfield Pattern

Description	Goal
E-Field Magnitude at $\theta = \pm 60^\circ$	$-10 \text{ dB} \pm 3 \text{ dB}$
H-Field Magnitude at $\theta = \pm 60^\circ$	$-10 \text{ dB} \pm 3 \text{ dB}$
Maximum Backlobe / Sidelobe Magnitude	$< -15 \text{ dB} + 2 \text{ dB}$
Maximum Cross Polarization Magnitude	$< -15 \text{ dB} + 2 \text{ dB}$

Note 1: All values relative to the E-Field magnitude at the boresight

Note 2: Cross polarization is measured at  $\phi = 45^\circ$

**Table 4.4:** Relaxed Design Goals for the Farfield Patterns

Description	Goal
E-Field Magnitude at $\theta = \pm 60^\circ$	$-10 \text{ dB} \pm 4 \text{ dB}$
H-Field Magnitude at $\theta = \pm 60^\circ$	$-10 \text{ dB} \pm 4 \text{ dB}$
Maximum Backlobe / Sidelobe Magnitude	$< -15 \text{ dB} + 4 \text{ dB}$
Maximum Cross Polarization Magnitude	$< -15 \text{ dB} + 4 \text{ dB}$

Note 1: All values relative to the E-Field magnitude at the boresight

Note 2: Cross polarization is measured at  $\phi = 45^\circ$

## 4.4 Physical Constraints

In a parabolic centre-fed antenna, the feed is directly in the path of the incoming signal from space. In this configuration, the feed reduces the total energy being collected by the parabolic antenna. The energy blocked is

$$E_{blocked} \propto \pi \cdot r_{feed}^2 \quad (4.1)$$

where  $r_{feed}$  is the outer radius of the feed antenna. For this reason the total radius of the feed antenna should not be unnecessarily large.

## Chapter 5

# Design Procedure

This chapter describes the overarching methodology for the electrical design of the prototype. The novel nature of the design meant that the design procedure was not strictly iterative, specifically a design decision made for one part of the design often required another part of the design to be reanalyzed and modified. In addition, a significant amount of learning occurred throughout the course of the project, which often resulted in the need to go back and modify the previously made assumptions and decisions.

To aid the reader in understanding the design methodology, the design procedure will be presented in a logically iterative fashion and not in chronological order. Attempts will be made to note when a design decision occurred in a significantly different order than presented.

All simulations done during the design procedure were conducted in CST. For all simulations, assumptions were made that the simulation model was made of a perfect (lossless) conductor and that the background material was a vacuum.

### 5.1 Concept

The concept for this project was developed by Dr. Tom Landecker and Dr. Bruce Veidt at DRAO. The concept documents created at DRAO are included in appendices A, B, and C. The concept was to use a log-periodic waveguide structure to address some of the shortcomings of existing designs for broadband feed antennas.

Since radio astronomers are interested in the polarization of the received signal, the design includes two sets of orthogonal excitation structures to collect both polarizations.

## 5.2 Choosing the General Waveguide Shape

The concept documents for this project outlined multiple forms of log-periodic waveguide structures. The first step in the design procedure was to determine which waveguide structure should be used for the design. The primary criterion used to decide on the structure was the quality of the farfield patterns each structure produced. Two initial designs from the concept documents were considered: a nested coaxial waveguide design and a parallel rectangular waveguide design with each iteration containing four rectangular waveguides, as shown in figure 5.1.

For the rectangular design, the waveguides have to be a distance of at least half a wavelength ( $\lambda/2$ ) apart to allow space for the second set of waveguides to be included for the orthogonal polarization. With each pair of waveguides separated by an electrical distance of  $\lambda/2$ , the farfield patterns were too narrow for the parabolic antenna specified for this project.

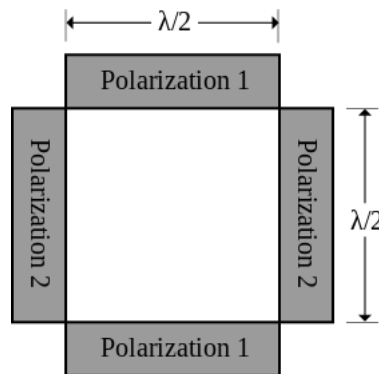


**Figure 5.1:** *Generic Layout of Rectangular Waveguide Antenna*

For the nested coaxial waveguide design, the antenna is circularly symmetric, so the same waveguide can be used for both polarizations. The preliminary tests for the nested coaxial design showed good farfield patterns over a reasonably large bandwidth. On the basis of these tests, the nested coaxial waveguide design was

chosen for further development.

### 5.3 Farfield Bandwidth of Coaxial Waveguides

To determine how feasible coaxial waveguides are for broadband applications, the maximum achievable bandwidth ratio in terms of farfield patterns needs to be determined. Bandwidth can be written as a frequency range  $f_{min}$  to  $f_{max}$  or as a ratio  $W = f_{max}/f_{min}$ . For example, the frequency range 1 GHz – 2 GHz can be expressed as a bandwidth ratio of  $W = 2:1$  or simply  $W = 2$ . Both notations are used throughout this thesis. In order to find the bandwidth ratio, we define a number of parameters as follows:

**Table 5.1:** Parameters Used to Define Waveguide Geometry

Parameter	Description
$a_n$	outer radius of the inner conductor of waveguide $n$
$b_n$	inner radius of the outer conductor of waveguide $n$
$t_n$	thickness of the outer conductor of waveguide $n$

$$\text{Waveguide Ratio} = \zeta \triangleq \frac{b_n}{a_n} = \frac{\text{outer conductor radius}}{\text{inner conductor radius}} \quad (5.1)$$

$$\text{Replication Ratio} = \eta \triangleq \frac{b_n + t_n}{a_n} = \frac{a_n \cdot \zeta + t_n}{a_n} = \frac{a_{n+1}}{a_n} \quad (5.2)$$

The replication ratio ( $\eta$ ) is the scaling factor used when creating the log-periodic structure. The bandwidth of a waveguide in the log-periodic structure can be found by scaling the bandwidth of the previous waveguide by a factor of  $1/\eta$ . For a log-periodic design to be feasible it must not have any “holes” in the bandwidth. To achieve this, the replication ratio must be less than or equal to the bandwidth ratio ( $\eta \leq W$ ). This condition ensures that there is some overlap between the bandwidth of each waveguide. In order for the antenna to be constructable, the waveguide ratio must be less than the replication ratio ( $\zeta < \eta$ ) in order for the waveguide walls to have positive thickness ( $t$ ). For simplicity,  $t$  is initially assumed to be arbitrarily thin, which makes  $\zeta \approx \eta$  and reduces the condition  $\zeta < \eta \leq W$  to  $\zeta < W$ .

Farfield performance goals were established in section 4.3. The bandwidth of waveguide  $n$  ( $W_n$ ) is defined as the continuous frequency range over which the farfield performance goals are met for waveguide  $n$ .

With this criterion set, a simulation was set-up to determine the best scaling ratio for the waveguides. The trade-off between bandwidth and the quality of the farfield patterns was evaluated. A model was created in CST of a single coaxial waveguide with the dimensions shown in table 5.2. The choice of  $b_1$  has no effect on bandwidth ratio because of the principle of frequency scaling.  $b_1$  was chosen to be 32 mm because this value was used in later stages of the design. The waveguide was excited with the  $TE_{11}$  mode by an ideal waveguide port. In CST, an ideal waveguide port matches the impedance of the waveguide, which prevents reflection at the port.

**Table 5.2:** *Model Dimensions for Waveguide Ratio Farfield Test*

Inner Wall Radius	$a_1$	$b_1/\zeta$
Outer Wall Radius	$b_1$	32 mm
Wall Thickness	$t_1$	$\approx 0$
Waveguide Length	$L$	$> \lambda$
Waveguide Ratio	$\zeta$	Variable

The simulations showed good farfield patterns at values of  $\zeta$  as low  $\zeta = 1.15$ . Table 5.3 shows the bandwidth ratio in regards to the farfield patterns goals given in table 4.3 for each value of  $\zeta$  simulated. This data shows that the criterion that  $\zeta < W$  was only met for  $\zeta = 1.15$ . It was noted that for all values of  $\zeta$ , the backlobes and sidelobes had a high magnitude. In conventional circular and coaxial waveguides, chokes or flanges are often used to reduce sidelobes and backlobes. No chokes or flanges were used in this series of simulations. Simulations on values of  $\zeta < 1.15$  were not done because they would require an impractically large number of concentric waveguides to reach the desired bandwidth ratio of 10:1. The conclusion of this series of test was that coaxial waveguide can produce good farfield patterns although with limited bandwidth.

**Table 5.3:** Bandwidth Results for Single Waveguide Ratio Tests

$\zeta$	$W_n$ [GHz]	$W$
1.15	1.55 – 1.8	1.15:1
1.2	1.5 – 1.75	1.16:1
1.3	1.4 – 1.65	1.17:1
1.4	1.35 – 1.65	1.22:1
1.5	1.35 – 1.6	1.18:1

### 5.3.1 Effect of Nested Waveguides on Farfield Bandwidth

Up to this point, simulations were conducted for only a single coaxial waveguide. The next phase of testing incorporated the nested waveguide structure. The goal of these tests was to determine what effect the nesting structure had on the farfield patterns. A model was created in CST with three nested coaxial waveguides as shown in figure 5.2. The middle ( $2^{nd}$ ) waveguide in the model had the same dimensions as the model in the single waveguide tests and the inner and outer waveguides were copies of the middle waveguide scaled by  $1/\eta$  and  $\eta$  respectively. The  $TE_{11}$  mode was excited in the middle waveguide using an ideal waveguide port. The resulting farfield patterns were examined and a second set of bandwidth data was taken as shown in table 5.4.

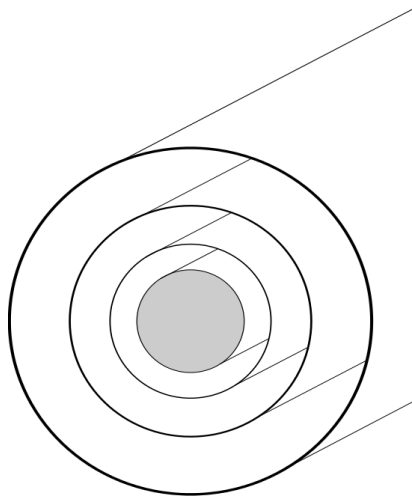


**Figure 5.2:** CST Model for Testing Nested Waveguides

**Table 5.4:** Bandwidth Results for Nested Waveguide Simulations

$\zeta$	$W_n$ [GHz]	$W$
1.15	1.8 - 2.2	1.22:1
1.2	1.7 - 2.3	1.35:1
1.3	1.5 - 2.2	1.47:1
1.4	1.4 - 2.1	1.50:1
1.5	1.3 - 2.15	1.65:1
1.6	1.2 - 2.05	1.71:1
1.8	1.15 - 1.8	1.56:1
2.0	1.15 - 1.8	1.56:1

Overall, the farfield patterns for the nested waveguides exhibited reduced back lobe and side lobe magnitude as well as significantly improved beamwidth of the main lobe. The reduction in the back lobe and the side lobes can be attributed to the increased width of the antenna. The improvements in all sections of the farfield pattern resulted in an increase in the overall bandwidth and an increase in the maximum value of  $\zeta$  that met the requirement that  $\zeta < W$ . Specifically, the maximum allowable value of  $\zeta$  was increased from  $\zeta = 1.15$  to  $\zeta = 1.6$  with a bandwidth ratio  $W = 1.71:1$ . In addition, it was noted that for  $\zeta = 1.8$  the farfield pattern from 0.95 GHz - 1.15 GHz was good except that its beamwidth was slightly wider than the goals shown in table 4.3. For reasons described in section 5.7, it is preferable for  $\zeta$ , and by association  $\eta$ , to be as large as possible. To achieve the maximum value of  $\zeta$ , the tolerances for the farfield goals were increased to  $\pm 4$  dB as shown in table 4.4. The bandwidths are significantly increased with this change as shown in table 5.5. It is interesting to note that for  $\zeta = 1.8$ ,  $\eta = 1.8$  the bandwidth ratio is 1.8:1, which meets the criterion  $\eta \leq W$ ; while the case for  $\zeta = 2$ ,  $\eta = 2$  doesn't meet this criterion. This indicates that  $\zeta = 1.8$  is approximately the maximum value of  $\zeta$  which meets the  $\eta \leq W$  criterion.

A second set of simulations was run for  $\zeta = 1.8$ , in which  $t$  was swept and the effect on the bandwidth was observed. Extending the wall thickness such that  $\eta = 2$  increased the bandwidth ratio to 2:1, which satisfies  $\eta \leq W$ . Based on these results the maximum achievable value for  $\eta$  with regard to farfield patterns is achieved with the dimensions listed in table 5.6.

**Table 5.5:** Comparing the Bandwidth under the Original and Relaxed Farfield Goals

$\zeta$	$\eta$	Farfield Goals	$W_n$ [dB]	$W$
1.8	$\approx 1.8$	Original	1.15 - 1.8	1.56:1
1.8	$\approx 1.8$	Relaxed	1 - 1.8	1.8:1
2	$\approx 2$	Original	1.15 - 1.8	1.56:1
2	$\approx 2$	Relaxed	0.95 - 1.8	1.89:1
1.8	2	Original	1.25 - 1.9	1.52:1
1.8	2	Relaxed	0.95 - 1.9	2:1

**Table 5.6:** Parameters for Maximum Replication Ratio with Regards to Farfield Patterns

$\zeta$	1.8
$\eta$	2
$W$	2:1

Based on these simulations, we concluded that a nested coaxial structure generates acceptable farfield patterns for sufficiently large replication ratios, and that the nesting structure improves the farfield performance over that of a single waveguide. These preliminary results indicated that a nested coaxial waveguide design was feasible for this project and a full electrical design was developed around the nested coaxial waveguide model.

## 5.4 Four Section Piece-Wise Design

For ease of design and optimization, the model was broken into four sections as shown in figure 5.3. The first two sections designed were the aperture section and the excitation section. Initially, these two sections had the same waveguide ratio. After a number of simulations in CST, it was found that it was suboptimal to have the same waveguide dimension for both the aperture section and excitation section. As a result, the two waveguide sections were decoupled and an aperture matching section (shown in figure 5.3) was inserted to provide a transition from the excitation section to the aperture section. Additionally, an aperture alignment section was inserted between the excitation section and the aperture matching section, as

discussed in section 5.9. All of these sections were assumed to act independently. This assumption was made because it allows the waveguide sections to be designed and optimized independently. The interactions between the sections will be considered at a later stage of the design. The excitation section and the aperture section also have to be designed to have the same operating bandwidth. This condition created a design loop between the excitation section and the aperture section, in which both sections had to be designed separately, but have the same bandwidth and have dimensions that fit together in the overall design. This design loop is not discussed at length in this thesis. The aperture matching section was designed after the aperture and excitation section designs were complete. Finally, the aperture alignment section was designed, which completed the electrical design procedure.

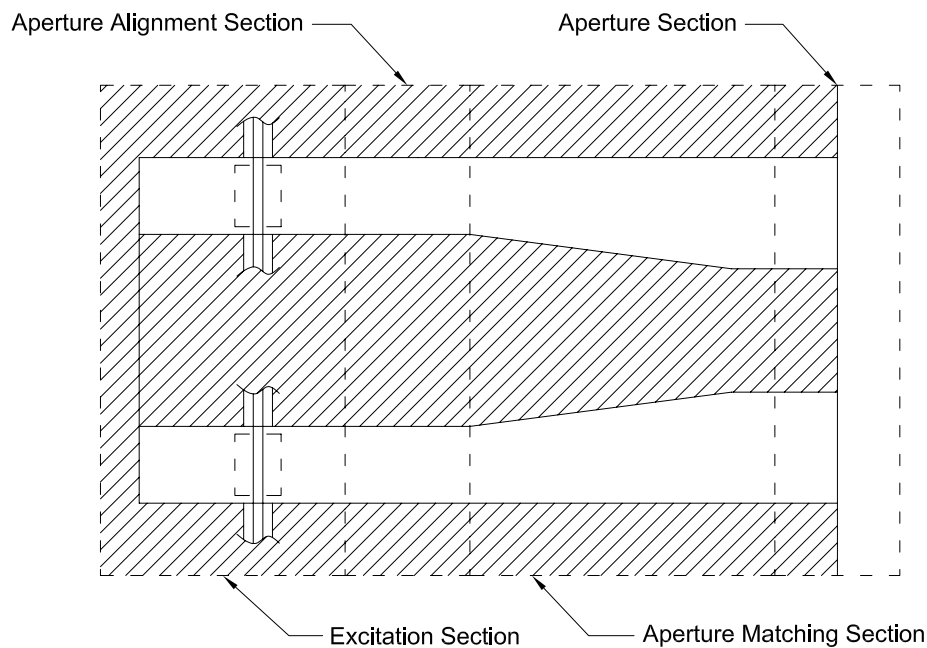


**Figure 5.3:** *Four Section Design*

## 5.5 Designing the Aperture

The aperture is the interface between the waveguides and free space. The primary design goal for the aperture is to simultaneously meet the farfield and bandwidth

requirements. The secondary design goal is to maximize the return loss (RL) as a result of reflections at the aperture, which in turn reduces the requirements on the aperture matching structure.

Based on section 5.3.1, we know that values of  $\zeta$  from 1.15 to 1.8 give acceptable farfield performance. This result is expanded by considering the effects of energy coupling from one waveguide to another. In general, coupling can be either beneficial or detrimental to the farfield patterns. Over a large bandwidth, it is likely that both beneficial and detrimental coupling will occur at different frequencies. To avoid any detrimental coupling, a design goal was set to minimize all coupling. In order to minimize coupling, the wall thickness  $t$  was varied, which in turn varies  $\eta$  according to equation 5.2. In CST, a three-waveguide model was built similar to the model used in section 5.3.1. For a fixed  $\zeta$ , the value for  $t$  was swept for all values such that  $\eta \leq W$ . The electric field amplitude was measured in the non-excited waveguides and the results were analyzed. The simulation sweep found that minimal coupling occurred with the maximum allowable waveguide wall thickness.

The return loss caused by the aperture was then considered. One issue with CST, and indeed waveguides operating in modes other than TEM in general, is that the concept of characteristic impedance is somewhat ambiguous. For coaxial waveguides propagating the  $TE_{11}$  mode, CST provides the return loss as a function of frequency. The return loss at the aperture for various values of  $\zeta$  with  $t \approx 0$  was found using CST and is shown in table 5.7.

**Table 5.7:** Return Loss for Various Values of  $\zeta$  when  $t \approx 0$

$\zeta$	RL [dB]
1.4	2.15
1.5	2.625
1.6	3.32
1.7	3.766
1.8	4.466

The goal for the return loss is to be greater than 10 dB, meaning very little energy is being reflected at the aperture. The simulations conducted in CST show that within the range of  $\zeta$  considered, waveguides with larger values of  $\zeta$  have better return loss. In section 5.3.1 it was found that the maximum allowable value

of  $\zeta$  is 1.8 with a bandwidth ratio of  $W = 2:1$ . The waveguide ratio in the simulation model was fixed at  $\zeta = 1.8$  and the wall thickness was swept to find the value that achieves maximum return loss. As with the previous results, having thick waveguide walls improves the performance. The final aperture design parameters are shown in table 5.8 which had a return loss of 4.55 dB when simulated in CST.

**Table 5.8:** *Final Aperture Design Parameters*

$\zeta$	1.8
$\eta$	2
$W$	2:1

## 5.6 Designing the Excitation Structure

The excitation structure is an essential part of the design. The goal of the excitation structure is to efficiently excite the desired  $TE_{11}$  mode in the waveguide while suppressing other modes. Additionally, the excitation structure needs to be matched with the source to maximize return loss. A loose design constraint was to achieve a  $50\Omega$  impedance for the feed line. This constraint can be adjusted to improve the return loss at the excitation structure, however  $50\Omega$  is an industry standard impedance, and most of the available parts have  $50\Omega$  interfaces.

The excitation structure is composed of the feed line, the excitation elements, and the excitation matching structure. The feed line is a coaxial line that passes through all the waveguides. In each waveguide, an excitation element is attached to the centre conductor of the feed line. Selecting the shape of this element was a significant challenge in this project. The excitation matching structure is a section of the coaxial waveguide located behind the feed line and is terminated with an electrical short. The length of the excitation matching structure ( $l_e$ ) was determined as part of the design procedure for the excitation elements.

In order to excite the  $TE_{11}$  mode, shown in figure 5.4, the optimal excitation structure is symmetric about the H-plane, with the two excitation structures being excited  $180^\circ$  out of phase. A second set of orthogonal excitation structures is not shown in the this section, but it is included during construction.

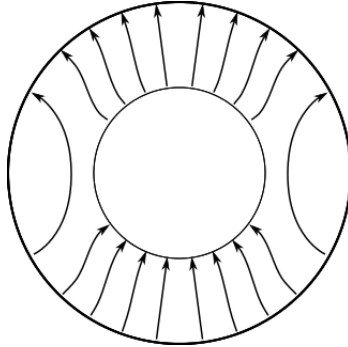


**Figure 5.4:** Electric Field of the  $TE_{11}$  Mode in a Coaxial Waveguide

### 5.6.1 Excitation Structure Goals

Using a simulator allows the excitation structure to be subdivided into the excitation structures that excite each waveguide. The substructures can be designed and optimized individually or in groups. The individual excitation structures can be treated like a three-port system in CST using the port definitions in figure 5.5. CST separates the power going into port 3 into the different modes at the port, which allows goals to be set for each mode. Table 5.9 defines a set of design goals for each individual excitation structure, with  $f_{min}$  being the minimum operating frequency of the excitation structure and  $f_{max}$  being the maximum operating frequency of the excitation structure. Each excitation structure is intended to work as a lowpass filter, allowing signals with frequencies lower than the operating band of the excitation structure to travel through, while radiating signals with frequencies within the operating band.

**Table 5.9:** Design Goals for Individual Excitation Structures

	$f < f_{min}$	$f_{min} < f < f_{max}$	$f_{max} < f$
Return Loss (RL)	> 10 dB		
Coupling to Waveguide: $TE_{11}$ Mode	< -10 dB	0 dB	< -10 dB
Coupling to Waveguide: Other Modes	< -10 dB		
Energy Travelling to Next Excitation Element	0 dB	< -10 dB	< -10 dB

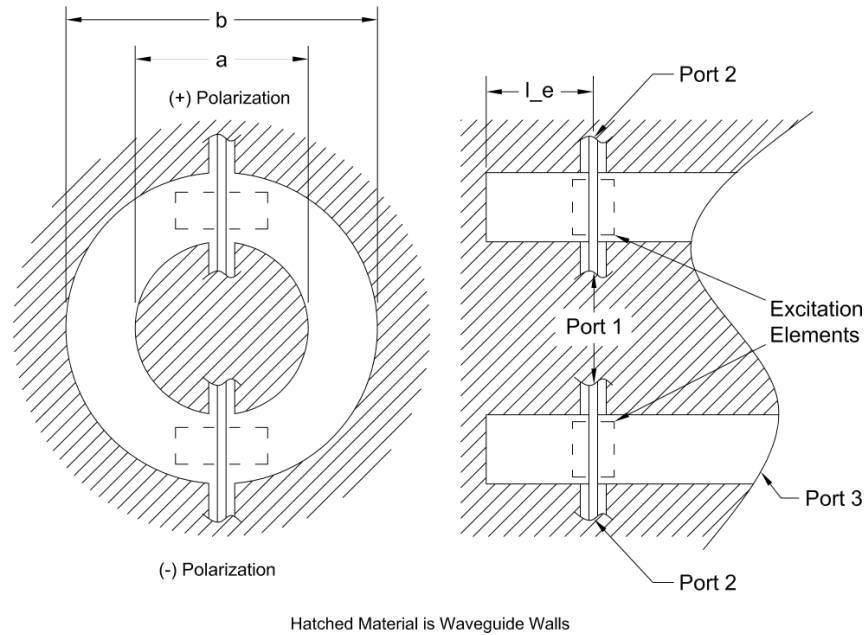


**Figure 5.5:** Port Definitions for Individual Generic Excitation Structure

### 5.6.2 Feed Line Design

The feed line passes through the waveguide walls connecting the excitation elements to a common input terminal. The feed line has a rectangular centre conductor and uses a rectangular feed gap cut out of the waveguide walls as the outer conductor. Rectangular components are used because they are easier to simulate and fabricate. To obtain a high characteristic impedance in the feed line, air is used as the dielectric.

The impedance of a general rectangular waveguide with the dimensions shown in 5.6 that is operating in the TEM mode can be approximated using Bräckelmann's approximation [9, pp. 24]:

$$Z_0\sqrt{\epsilon_r} = 59.952 \ln \left( \frac{1 + W'/b}{W/b + t/b} \right) \quad (5.3)$$

where the variables are defined in figure 5.6.

The desired characteristic impedance of the feed line is determined in the design process of the excitation structure. The feed line was designed according to

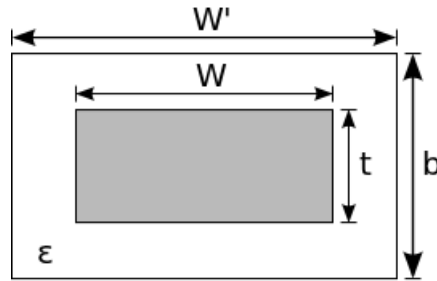


**Figure 5.6:** Parameters for Finding the Characteristic Impedance of a Rectangular Coaxial Waveguide

formula 5.3 and verified in simulation.

Two simulation models for the feed line were used for this project. The first model was a small square coaxial waveguide ( $W' = b, W = t$ ). This model performed well in simulation and was used for the crossbar, frisbee, and hybrid excitation design simulations (see section 5.6.3). The small feed line would have notable conductive losses and would have difficulty supporting the weight of the excitation elements. To address these issues, a larger feed line model was designed. The simulated performance of the hybrid excitation structure with the larger feed line was compared to the performance with the small feed line. With the larger feed line, the performance of the innermost waveguide was significantly reduced and the performance of the middle waveguide was notably reduced. This loss of performance was attributed to the feed line creating a hole in the waveguide wall that had an electrically significant size. These holes disrupt the electromagnetic fields inside the waveguide. To correct for this effect, the square feed line was discarded and a narrow rectangular feed line was designed to replace it. The long dimension of the feed line was oriented in the transverse direction to the electric field of the  $TE_{11}$  mode in order to minimize the disruption to the electromagnetic field.

As shown in equation 5.3, the characteristic impedance of a feed line is defined by the relative dimensions of its centre conductor and walls, not the absolute dimension. In order to reduce the size of the feed line gaps, and thus reduce the disturbance to the electromagnetic field, the centre conductor size should be small. Conversely, the centre conductor should be relatively large to reduce conductor

loss and increase the structural strength of the feed line.

To compromise between these requirements, a stepped excitation structure was proposed as shown in figure 5.7. A small feed line was used in the high frequency waveguides which transitioned into larger feed lines for the lower frequency waveguides. For ease of construction, the height of the feed line conductor and gap was kept constant and the widths varied to achieve the desired characteristic impedance. The centre conductor height was chosen to be 3.18 mm ( $1/8''$ ) as a compromise between surface area and strength.  $1/8''$  is also a readily available thickness of sheet metal. The capacitance gaps, shown as  $cg$  in figure 5.7, were varied until no filtering effects were observed in the operating frequency range of the antenna.

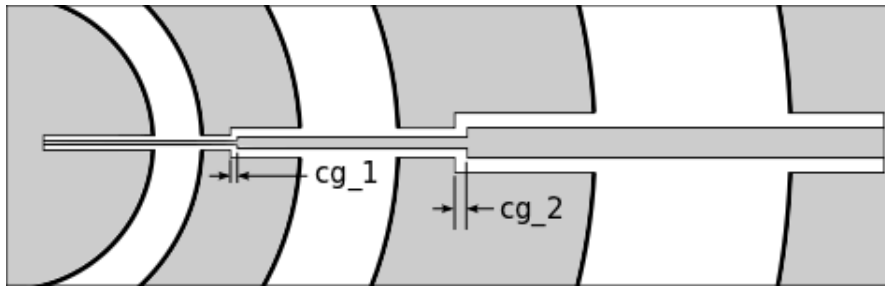


**Figure 5.7:** Stepped Feed Line

The stepped feed line was used for the three-angle excitation design (section 5.6.3.4) and the prototype design (chapter 6). The dimensions of the stepped feed line structure are shown in table 5.10.

**Table 5.10:** Design Dimensions for Redesigned Feed Line

Section	1	2	3
Feed Gap Width	4 mm	5.5 mm	7.5 mm
Feed Gap Height	10 mm		
Centre Conductor Width	1.15 mm	2.2 mm	3.5 mm
Centre Conductor Height	3.18 mm		
Characteristic Impedance	49.25 $\Omega$	49.05 $\Omega$	49.17 $\Omega$

### 5.6.3 Excitation Element Design

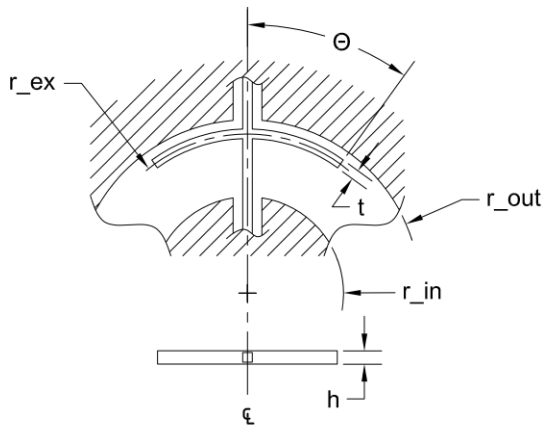
The starting point for the excitation structure was to have the same waveguide dimension as the aperture and no excitation element other than the feed line in the waveguide. Simulations showed that this design radiated very poorly, and that a more complicated excitation element was required. During the design procedure, four designs for the excitation elements were created and optimized. They were created iteratively, with each design improving over the previous design.

#### 5.6.3.1 Crossbar Excitation Design

The initial design for the excitation element was a narrow thin strip of metal concentric to the waveguide wall with radius  $r_{ex} < r_{out}$  and  $r_{ex} \gg r_{in}$ . Figure 5.8 shows the crossbar excitation structure. The initial waveguide ratio ( $\zeta$ ) at the excitation structure was set to  $\zeta = 1.8$  to match the aperture. A model with a single waveguide was created for this design and simulated in CST. This model excited the  $TE_{11}$  mode well, and exhibited beneficial frequency filtering behaviours similar to a lowpass filter. This model was optimized but performance limitations were found. Upon analysis of the results, it was determined that this limit was caused by an impedance mismatch in the excitation structure. The waveguide ratio was reduced at the excitation structure to a value of  $\zeta = 1.3$ . This change yielded significantly improved performance, although there was still a moderate impedance mismatch. The cutoff frequency for the  $TE_{11}$  mode was also affected by the change in waveguide ratio. The model was scaled to bring the operating band back to the design bandwidth.

Design parameters and the performance after another optimization are shown in table 5.11 and figure 5.9. The design bandwidth for this model is 1.1 GHz to 2 GHz. The coupling to the  $TE_{11}$  mode in the waveguide was near the design goal of 0 dB but the return loss was only mediocre, being as low as 5 dB within the design bandwidth.

The model was then expanded to include three nested waveguides and the simulation was performed again. The results were examined and the return loss was found to have severely reduced performance. A simulation for the single waveguide model was conducted for a larger frequency range with the results shown in



Hatched Material is Waveguide Walls

In the transmitting case, a broadband signal enters at the centre. The excitation structure couples signals to the waveguide that can propagate along that waveguide. Signals at lower frequencies pass beyond the waveguide that is shown and are radiated from further waveguides.

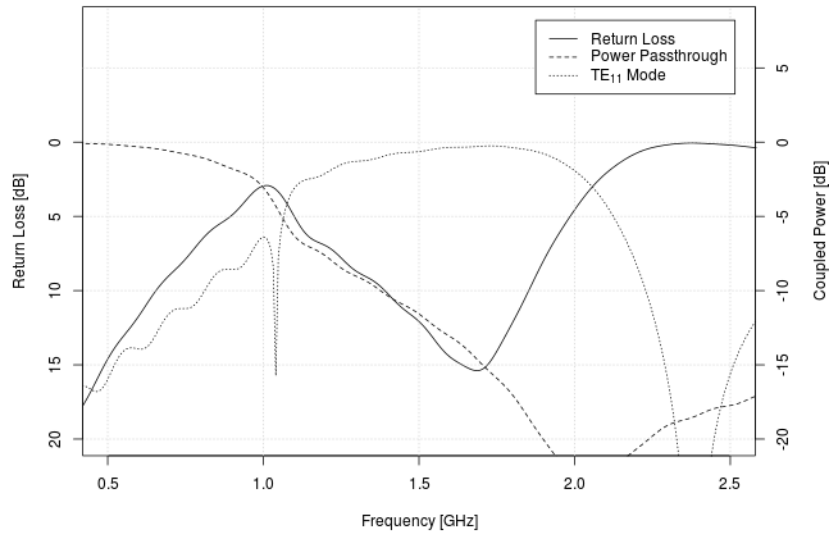
**Figure 5.8:** Crossbar Excitation Design

**Table 5.11:** Parameter Results for the Partially Optimized Crossbar Excitation Design

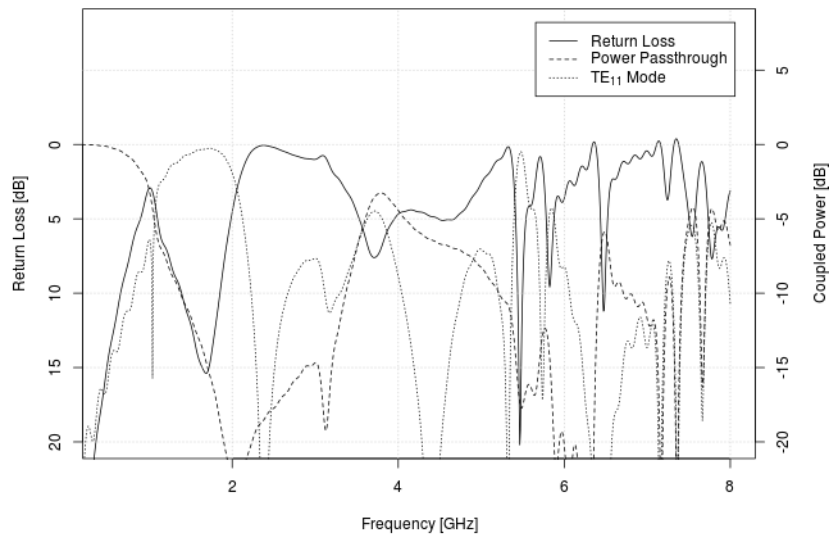
Symbol	Description	Result
	Frequency Range	1 GHz – 2 GHz
$r_{in}$	Waveguide Inner Wall Radius	40 mm
$r_{out}$	Waveguide Outer Wall Radius	52 mm
$\zeta$	Waveguide Ratio	1.3
$r_{ex}$	Radius of Crossbar	40 mm
$\theta$	Excitation Element Angle	45.84°
$h$	Height of Crossbar	1 mm
$t$	Thickness of Crossbar	1 mm
$l_e$	Length From Back of Waveguide	70 mm
$Z_{0_{feed}}$	Feed Line Characteristic Impedance	50.4Ω

figure 5.10. The return loss for the single waveguide model is very poor outside the frequency band of the specific waveguide. As a result of this, when multiple excitation structures are combined in series, the overall return loss will be poor. The three-waveguide model was optimized in an attempt to remove this issue but the optimization did not find a solution that met the design goals.

Because of this poor return loss, the crossbar excitation element was ruled out. Further, because of the inconsistencies between the one-waveguide model



**Figure 5.9:** Simulated Crossbar Excitation Design Results



**Figure 5.10:** Simulated Crossbar Excitation Design Results – Extended Frequency Range

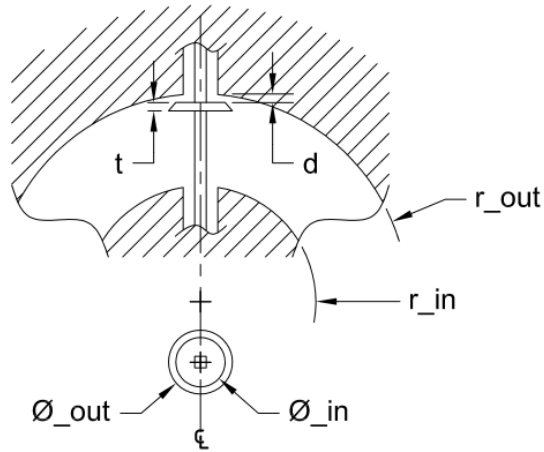
results and the three-waveguide model results, only the three-waveguide model was considered for the remainder of the excitation design phase.

The return loss issue was likely related to the long excitation elements which have significant electric length. At higher frequencies, the long elements begin to resonate like monopoles. This resonant behaviour is consistent with the frequency dependent variations displayed in figure 5.10. To combat this effect, a more compact excitation element was required. It is likely that the good coupling to the waveguide was created by the capacitance between the excitation element and the waveguide wall. An effort was made to maintain similar capacitance while altering the excitation element design.

### 5.6.3.2 “Frisbee” Excitation Design

The next design considered was the “Frisbee” design. The “Frisbee” excitation element is a disk with sloped edges as shown in figure 5.11. The flat surface of the disk produces the capacitance required to excite the mode in the waveguide. The sloped edges increase the bandwidth of the model by varying the distance from the disk to the waveguide wall. In the frequency domain, this is equivalent to having constant electrical distance over a frequency range. The “Frisbee” design was expected to have issues achieving the same impedance as the crossbar design.

The “Frisbee” design was modelled with a three nested waveguide structure. The initial simulated results were promising and the model was optimized with the disk dimensions and the waveguide ratio as optimization parameters. In addition, to allow the optimizer to find a better impedance match, the feed line dimensions were used as additional optimization parameters. This allowed  $Z_{0_{feed}}$  to be indirectly controlled by the optimizer. The optimization results, shown in table 5.12, produced good electrical performance as shown in figure 5.12. Figure 5.13 shows that the desired mode,  $TE_{11}$ , was coupling well to the waveguide; and the undesired mode,  $TE_{31}$ , had an amplitude 6 dB below the  $TE_{11}$  mode.



Hatched Material is Waveguide Walls

**Figure 5.11:** “Frisbee” Excitation Design

**Table 5.12:** Parameter Results for the Optimized “Frisbee” Excitation Design

Symbol	Description	Result
	Frequency Range	2 GHz – 4 GHz
$r_{out}$	Waveguide Outer Wall Radius	32 mm
$r_{in}$	Waveguide Inner Wall Radius	25.6 mm
$\zeta$	Waveguide Ratio	1.25
$d$	Distance from Waveguide Wall to Disk	1.6 mm
$t$	Disk Thickness	1.2 mm
$\varnothing_{in}$	Frisbee Inner Diameter	3 mm
$\varnothing_{out}$	Frisbee Outer Diameter	6 mm
$l_e$	Length From Back of Waveguide	26 mm
$Z_{0_{feed}}$	Feed Line Characteristic Impedance	60.4 $\Omega$

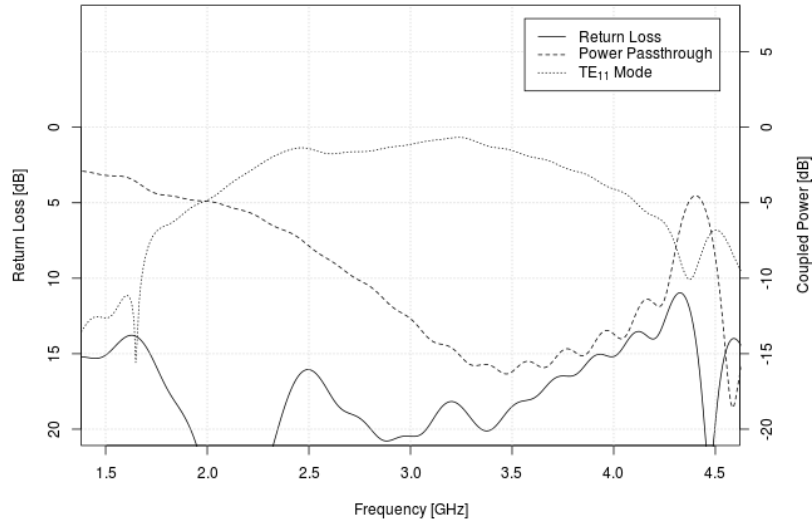


**Figure 5.12:** Simulated “Frisbee” Excitation Design Results

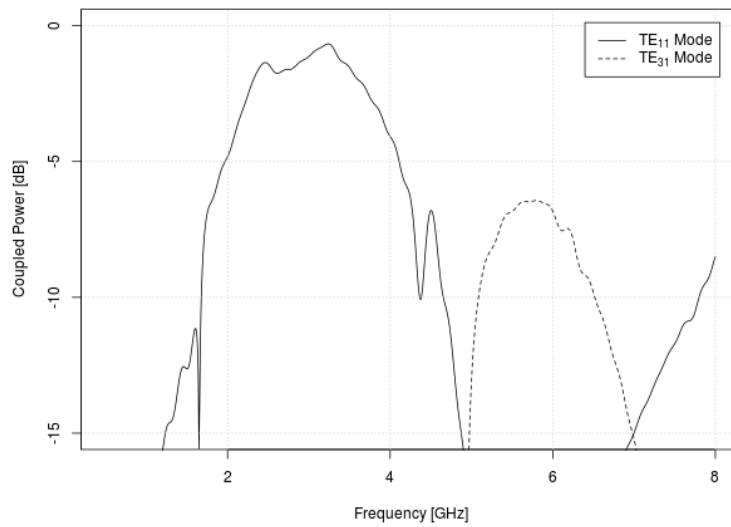


**Figure 5.13:**  $TE_{11}$  and  $TE_{31}$  Modes in Simulated “Frisbee” Excitation Design Results

### 5.6.3.3 Hybrid Excitation Design

As discussed in section 5.6.4, the “Frisbee” excitation design resulted in some farfield issues. It was believed that one solution to these issues was to further suppress the  $TE_{31}$  mode. This was done through another iteration of the excitation structure design. A wider excitation element should not generate the  $TE_{31}$  mode as readily as a compact structure such as the “Frisbee” model. It was proposed that a hybrid of the crossbar and “Frisbee” excitation models might fulfil this need. A series of models ranging from a compact model to a wide, thin model were simulated. All of these models maintained approximately the same surface area for each excitation element. The best model was found to be a square sheet of metal bent into an arc as shown in figure 5.14. The centre of the arc is slightly offset from the centre of the waveguide such that it bends away from the waveguide wall to increase the bandwidth. This model was put through an optimization and the resulting parameters are shown in table 5.13. The electrical performance for the optimized design is shown in figure 5.15 and figure 5.16.

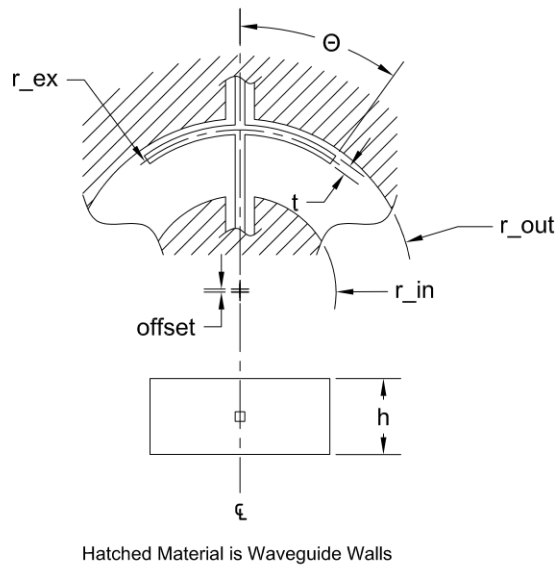


**Figure 5.14:** Hybrid Excitation Design

**Table 5.13: Parameter Results for the Optimized Hybrid Excitation Design**

Symbol	Description	Result
	Frequency Range	2 GHz – 4 GHz
$r_{out}$	Waveguide Outer Wall Radius	32 mm
$r_{in}$	Waveguide Inner Wall Radius	25.6 mm
$\zeta$	Waveguide Ratio	1.25
$r_{ex}$	Radius of Excitation Element	30.225 mm
$\theta_{ex}$	Angle of Excitation Arc	17.5°
$t$	Disk Thickness	1 mm
$h$	Excitation Element Height	3 mm
$offset$	The Distance from the Centre of the Waveguide to the Centre of the Excitation Element Arc	13.18 mm
$l_e$	Length From Back of Waveguide to Excitation Element	30.365 mm
$Z_{0_{feed}}$	Feed Line Characteristic Impedance	71.31 $\Omega$

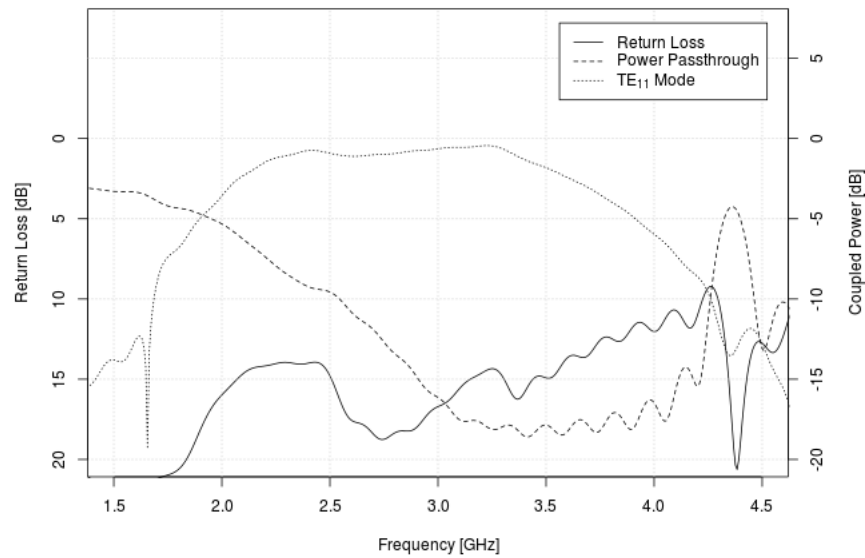


**Figure 5.15: Simulated Hybrid Excitation Design Results**

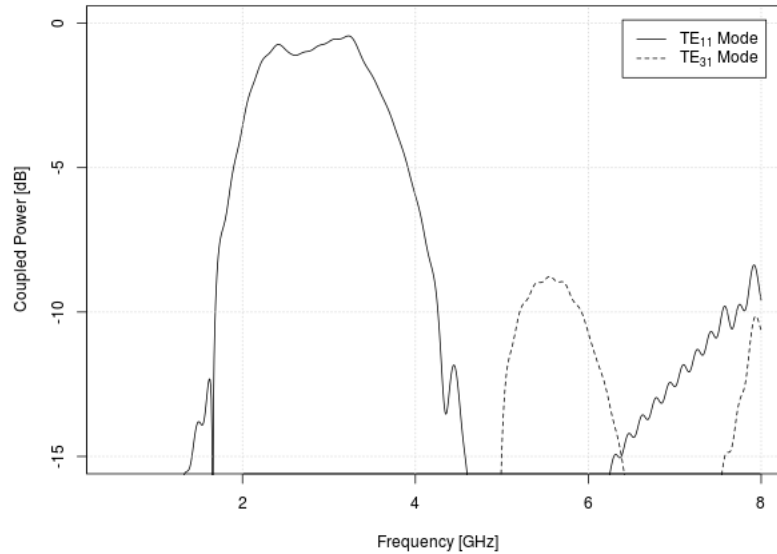


**Figure 5.16:**  $TE_{11}$  and  $TE_{31}$  Modes in Simulated Hybrid Excitation Design Results

#### 5.6.3.4 Three-Angle Excitation Design

As shown in figure 5.14, the hybrid excitation elements were designed to be a thin sheet of copper that ran concentric to the waveguide walls. The design required copper sheets to be cut into the correct shape, then soldered to the feed line at the designed locations before the feed lines are installed into the antenna. Cutting the thin sheets of copper to the correct size and then bending them to the correct radius was very difficult. To simplify the construction, the excitation element was redesigned to be the same height as the thickness of the centre conductor of the feed line. This meant that the feed line and the excitation element could be combined into one piece, which could be fabricated using a water-jet cutting machine.

When this change was made, the back section had already been fabricated, so the excitation structure had to be redesigned within the constraints of the existing feed line and excitation matching structure. This limited the effectiveness of the design but simplified the optimization process.

The height constraint for the excitation element meant that the excitation design returned to the crossbar design described in section 5.6.3.1. Another solution to the problem of poor return loss had to be found. It was proposed that since the wide-angle crossbars seemed to cause poor return loss, while the narrow-angle crossbars created over-moding issues, that the crossbar should be wide-angle in the waveguides with over-moding issues and narrow-angle otherwise. The resulting three-angle excitation design is shown in figure 5.17. While this is a departure from the frequency scaling philosophy of the antenna design, it does significantly improve the overall performance. The excitation elements were re-optimized allowing the angle of each element to be changed independently, resulting in the dimensions shown in table 5.14. The piece-wise electrical results for the new excitation design are shown in figure 5.18. This design had good return loss but the coupling into the waveguides, especially the first waveguide, was lower than it was in the other excitation designs.

**Table 5.14:** *Parameter Results for the Optimized Three-Angle Excitation Design*

Symbol	Description	Waveguide		
		1	2	3
$r_{out}$	Waveguide Outer Wall Radius	16 mm	32 mm	64 mm
$r_{in}$	Waveguide Inner Wall Radius	12.8 mm	25.6 mm	51.2 mm
$\zeta$	Waveguide Ratio	1.25		
$r_{ex}$	Radius of Excitation Element	15.25 mm	30.5 mm	61 mm
$\theta_{ex}$	Angle of Excitation Arc	15°	17°	28°
$t$	Crossbar Thickness	0.5 mm	1 mm	2 mm
$h$	Excitation Height	3.18 mm		
$l_e$	Length From Back of Waveguide to Excitation Element	15.635 mm	31.27 mm	62.54 mm
$Z_{0_{feed}}$	Feed Line Impedance	$\approx 50 \Omega$		

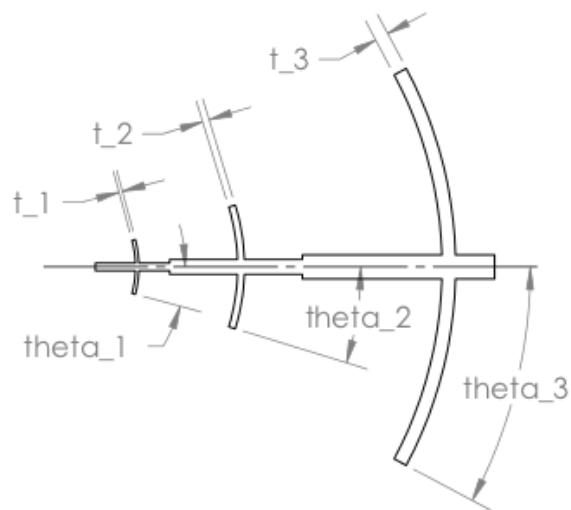
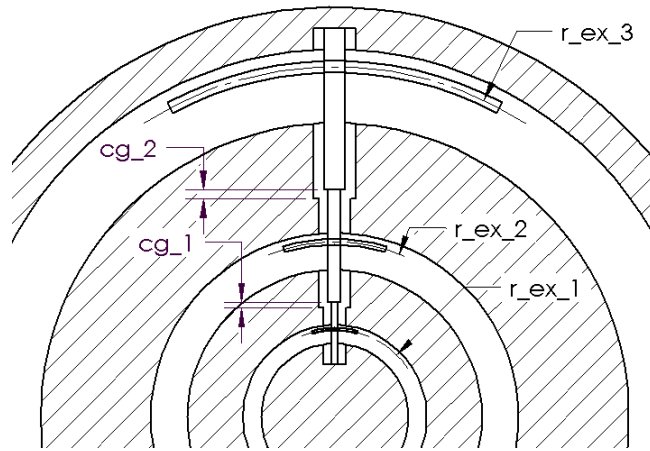


**Figure 5.17:** Three-Angle Excitation Design

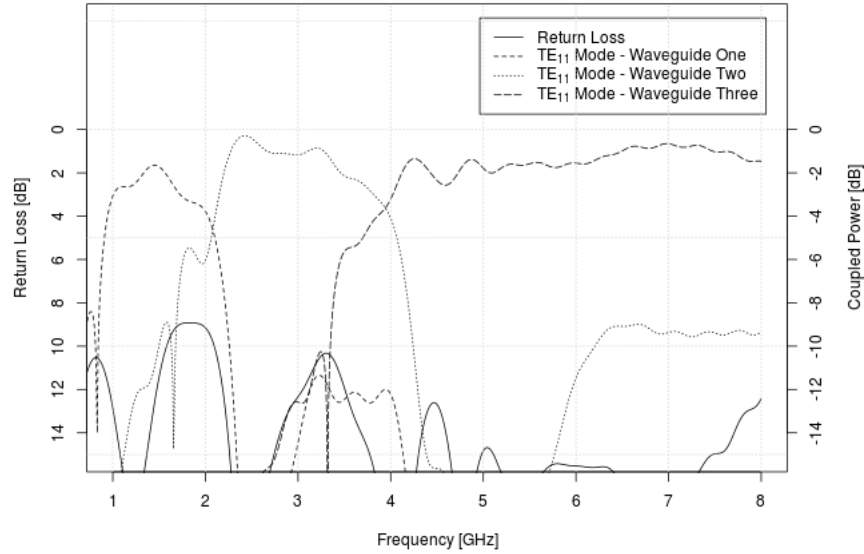


**Figure 5.18:** *Electric Performance of Three-Angle Excitation Design*

#### 5.6.4 Analyzing the Farfield of the Partial Model

In order to determine the effect of the excitation structure on the farfield pattern, a partial model had to be simulated. A model was created using the optimized “frisbee” excitation structure with the previously defined aperture geometry and a simple gradient aperture matching structure. The model was excited using ideal waveguide ports on the feed line to emulate an ideal differential source.

The simulated farfield patterns were observed to have significant two-peak pattern at specific frequencies. Two-peak farfield patterns can be indicative of higher order modes being present in the antenna. The electromagnetic field in the waveguides was analyzed in CST and it was confirmed that the TE<sub>31</sub> mode was present in the antenna at frequencies where two-peak farfield patterns were observed. At the frequencies studied, the TE<sub>31</sub> mode was detected in waveguides other than the waveguide that should have been excited. This phenomenon is expected in a log-periodic design. While each waveguide is designed to only allow the desired mode to propagate, if fed with energy at a frequency well above the design frequency, it

may generate additional unwanted waveguide modes.

In order to verify that the  $TE_{31}$  mode was being generated at the excitation structure and not by coupling at the aperture, the model was modified by placing a simulated waveguide port at the aperture, thus removing any aperture effects. The electromagnetic fields were examined again and the  $TE_{31}$  mode was still present, though at a lower amplitude. The amplitude of the  $TE_{31}$  mode was affected by both the excitation structure and the aperture.

### 5.6.5 Suppressing the $TE_{31}$ Mode

One possible solution to the  $TE_{31}$  issue is to suppress the mode. In a conventional antenna, mode suppression can be achieved by altering the waveguide structure to cutoff the higher order modes at the design frequency. However, because the higher order modes are occurring in waveguides designed to operate at lower frequencies, it would be impossible to cause the higher order modes to be cutoff without also cutting off the desired modes at lower frequency.

A multi-pronged approach was used to address the  $TE_{31}$  issue. First, a method to prevent high frequencies from travelling to the outer waveguides was sought. It was hoped that if the excitation structure coupled energy to the waveguide efficiently in its operating bandwidth, there would be no energy left in the frequency range to travel to the outer waveguides and cause modes to be excited in those waveguides. An attempt was also made to model the feed line passing through the waveguide wall as an RLC filter, but this is a difficult modelling problem and beyond the scope of the project. Next, an attempt to suppress the  $TE_{31}$  mode after it was excited was made. As shown in figure 5.19, there is an electric field line at a  $\pm 60^\circ$  offset from centre. It was hypothesized that the electric field could be disrupted by placing metal walls parallel to the magnetic field. The metal walls would force the electric field to be normal to the walls, thus eliminating the mode. To accommodate both polarizations, the metal walls are placed at  $\pm 45^\circ$  off centre as shown in figure 5.20. Simulations showed that this fundamentally changed the waveguide structure. The cutoff frequency of the  $TE_{11}$  mode and the electric field pattern of the new structure indicated that the structure was acting like a bent rectangular waveguide, not a coaxial waveguide. While this did address the  $TE_{31}$

issue, it also increased the cutoff frequency of each waveguide, and as a result the farfield pattern became too narrow. Finally, a set of models was created using posts or irises to suppress the  $TE_{31}$  mode, but these models resulted in highly resonant behaviour at the aperture, reducing the overall return loss of the model. No satisfactory method of mode suppression was discovered during this project.

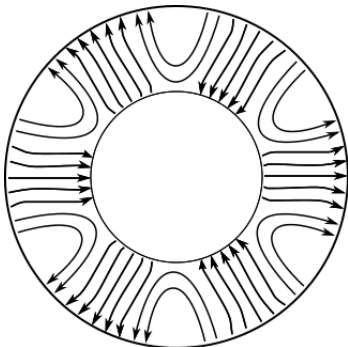


*Figure 5.19: Electric Field for the  $TE_{31}$  Mode in a Coaxial Waveguide*

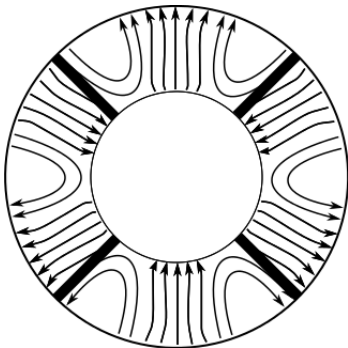


*Figure 5.20: 45° Walls with the  $TE_{31}$  Mode Overlaid*

The solution to the  $TE_{31}$  issue used in the prototype was to design the excitation structure to reduce the coupling of the  $TE_{31}$  mode to the waveguides, but this was achieved at some cost to the overall performance of the excitation structure.

## 5.7 Designing the Aperture Matching Structure

The objective of the aperture matching section is to provide a transition from the waveguide dimensions at the excitation structure to the waveguide dimensions at the aperture and to maximize return loss at the aperture. In waveguide antennas, this task is normally achieved by slowly widening the waveguide such that it is a good match to free space. This technique often results in a very large aperture. In this design, the dimensions of the waveguide at the aperture are constrained by farfield requirements and the nested coaxial structure, thus a more complex matching design is required.

To achieve a lossless match between two waveguides of different dimensions, a smooth and slow transition would suffice in the form of either a sloped or a parabolic geometry. In this design it was found that although it was possible to have high return loss at the transition from one waveguide geometry to the other, the overall return loss including the aperture reflections was poor. To achieve better overall performance, free space was used as the matching target instead of the aperture geometry. A bandpass matching structure was required to match the waveguide geometry at the excitation structure to free space over the operating band of the waveguide. A stepped structure inspired by a Chebyshev or binomial matching structure was considered.

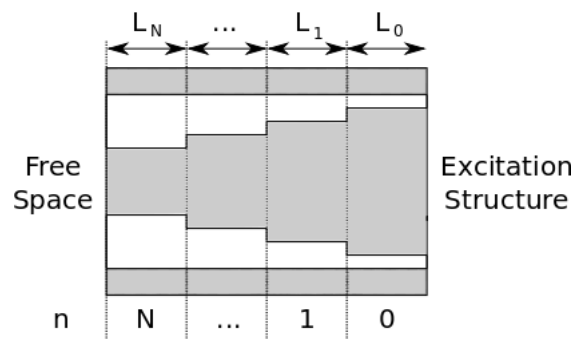


**Figure 5.21:** Cross Section of a Generic Stepped Matching Structure

The lengths of the steps,  $L_1, L_2, \dots, L_N$ , were initially set to a value of  $\lambda/4$ , where  $\lambda$  is the free space wavelength for the centre of the waveguide's frequency band. To isolate the performance of the aperture matching structure, an ideal wave-

guide port was used in place of the excitation structure to excite the  $TE_{11}$  mode. Using this ideal source, the length of the waveguide from the excitation structure to the first step,  $L_0$ , was found to have no effect on the return loss and will be optimized later as described in section 5.9. Because wavelengths are longer in a waveguide than they are in free space, the initial values for  $L$  were too short. The simulation results were examined and the centre frequency of the match was found by evaluating the frequency at which the return loss was maximized. Using this information, the values of  $L$  were altered to shift the centre frequency of the match to the centre of the frequency band.

CST models were created for both a two step ( $N = 2$ ) and a three step ( $N = 3$ ) matching structure. Both models were initially set to have linear physical step sizes and then optimized. The optimizations resulted in the  $N = 2$  model with the dimensions in table 5.15 having the best performance. Figure 5.22 shows the return loss of the optimized aperture matching structure.

**Table 5.15:** Results of Aperture Matching Structure Design

$n$	0	1	2
$L$ [mm]		28	28
$d_{in}$ [mm]	64	64	64
$d_{out}$ [mm]	51.2	47.42	35.56
Freq [GHz]	2 – 4		

## 5.8 Designing the Choke

The purpose of the choke in this design is to reduce the side lobes in the lowest frequency band of the antenna. Although the choke will also affect the return loss, this effect was assumed to be minor and was not considered in the design process.

The side lobes of the radiation pattern are partially created by surface currents on the sides and back of the antenna. The choke reduces these surface currents by creating a long current path between the aperture and the sides of the antenna. Chokes usually have a length of  $\lambda/4$  which causes the choke to be electrically open at its aperture. It has been shown in [23, pp. 212] that a quarter wavelength choke improves the farfield pattern of a coaxial waveguide antenna.

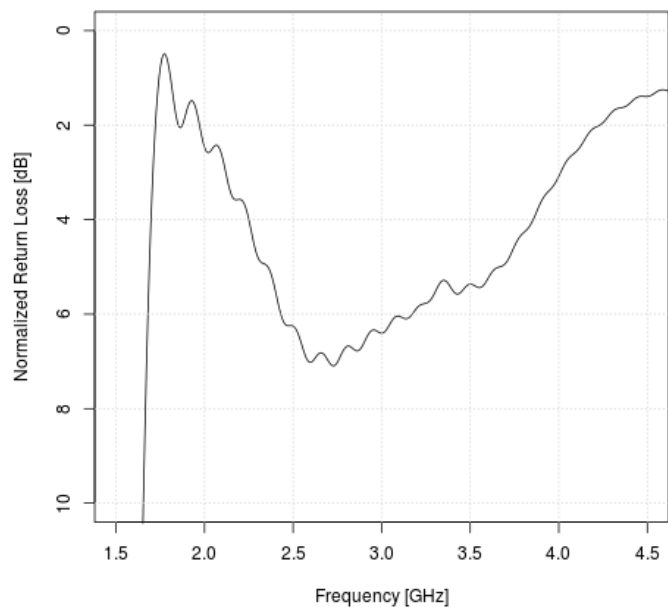


**Figure 5.22:** Return Loss for Optimized Aperture Matching Structure

A model with parameters shown in figure 5.23 was created to simulate the choke. Initially, the choke was designed to operate at the centre frequency of the lowest frequency band, 1.5 GHz. The initial dimensions of the choke for the simulation sweep were  $L_{choke} = \lambda/4$  with arbitrary width ( $W_{choke}$ ) and wall thicknesses ( $t_{choke}$ ). Twenty farfield pattern snapshots were taken evenly spaced across the frequency range for each simulation in the sweep.  $W_{choke}$  and  $L_{choke}$  were swept and the farfield data was exported then parsed and plotted in Excel. The plots were evaluated manually to determine the dimensions that produce the best farfield patterns across the entire frequency band. Finally,  $t_{choke-in}$  and  $t_{choke-out}$  were swept and again farfield patterns were analyzed to determine the value that produced the best farfield patterns. It was found that for reasonably low values of  $t_{choke}$  there was relatively little change in the farfield patterns. The final choke dimension are shown in table 5.16.

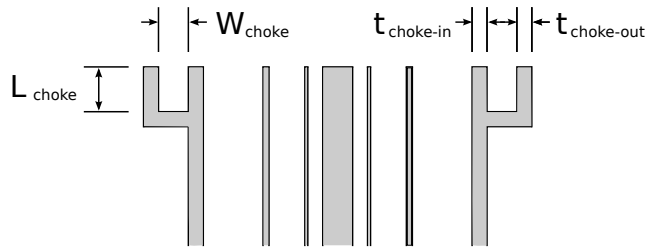


**Figure 5.23:** Cross Section of a Generic Choke

**Table 5.16:** Design Dimensions for Choke

$W_{choke}$	32.5 mm
$L_{choke}$	25 mm
$t_{choke-in}$	7.4 mm
$t_{choke-out}$	7.4 mm

## 5.9 Aperture Alignment Section Length Sweep

The apertures of all the waveguides are on one plane, and the excitation structure is on another plane. Since all the aperture matching structures have different lengths, an extra length of waveguide is required to allow the aperture of each waveguide to be in a common plane. We call this extra length of waveguide the aperture alignment section. If both the excitation structure and the aperture matching structure were matched properly to the waveguide, the length of the aperture alignment section would have little effect on the performance of the antenna except for a slight increase in conduction losses due to the increased lengths of the waveguides. However, because both the excitation structure and the aperture matching structure are imperfectly matched to the waveguide, the length of the aperture alignment section creates a phase shift between the aperture matching structure and the excitation structure and thus can affect the return loss. The amount of phase shift varies based on the frequency and the length of the aperture alignment section.

Since the lengths of the aperture alignment section in each waveguide are interdependent, the only way to design this region is to simulate the whole antenna and sweep the length of the front section. The front section is described in chapter 6 and contains the aperture, aperture matching structures, and aperture alignment sections. Since the lengths of the aperture and aperture matching structures are

fixed, this procedure will directly vary the lengths of the aperture alignment sections. Given the available materials, the longest possible lengths of the aperture alignment sections produces the best overall return loss. The performance improvement created by extending the lengths of the aperture alignment sections was minor, and it may be preferable to choose shorter aperture alignment sections in order to save on materials and weight. Additionally, the importance of the aperture alignment sections as a method of improving the return loss could be reduced if the aperture matching is improved.

## Chapter 6

# Physical Prototype Design

The simulation model that was designed in CST needed to be turned into a physically realizable model. The drafting and design package SolidWorks was used to design the physical model. A significant task was to determine how to break the design into smaller components that could be fabricated and combined to create a prototype of the antenna. Additionally, the feed line had to be serviceable to allow the excitation structure to be installed. The simplest way to achieve this was to break the model at the feed line. This split the design into the back section, which contains the feed gap and the excitation matching structures, and the front section, which contains the aperture alignment section, the aperture matching structures, and the choke.

### 6.1 Front Section

The front section of the design, shown in figure 6.1, is composed of a number of concentric cylinders. The three inner cylinders, shown in figure 6.2, have a constant inner diameter and a stepped outer diameter which forms the aperture matching structures when the antenna is assembled. The outer cylinder, shown in figure 6.3, has constant inner radius and a step cut out of the outside to allow the choke, shown in figure 6.4, to be easily seated. The radius of the step is designed to be the inner radius of the choke. This simplifies the manufacturing of the choke by allowing the outer cylinder to act as the inner wall of the choke. All the components of the

front section are circularly symmetric and can be produced on a lathe. Note that the piece of copper tape on the top of the smallest cylinder is to correct a machining error.

## **6.2 Back Section**

The front and back sections are designed such that the excitation structure is located on the top surface of the back section. This allows the feed line gap and the excitation matching structure to be milled out of the back section without the need to reposition the back section on the milling machine. As discussed in section 5.6.2, each feed gap is composed of three sections. To simplify the fabrication of the feed line, the centre conductor of the feed line and feed line gap were designed to have a consistent depth with only the width of the centre conductor and gap being varied.

The excitation matching structure is composed of cylindrical slots cut out of the front face of the back section. The depths and widths of these cuts were designed during the electrical design procedure. Because the cuts are relatively shallow and sufficiently wide, they can be cut with a computer numerical control (CNC) milling machine.

To allow SMA cables to excite the feed line, a gap was bored out of the centre of the back section for the SMA cables to pass through. This bore was designed to be as wide as possible, while allowing enough metal thickness between the gap and the innermost waveguide for the machine screw clearances. The cross section of the back section is shown in figure 6.5.

### **6.2.1 Feed Line Termination**

The feed lines had to be electrically terminated. Open circuit and short circuit terminations were considered, but neither provided a high return loss with the  $50 \Omega$  feed line. A  $50 \Omega$  load connected to an SMA port was chosen to terminate the feed line. The SMA termination provided good physical support for the excitation structure because it was attached to the body of the antenna and provides an additional port for testing the excitation structure.

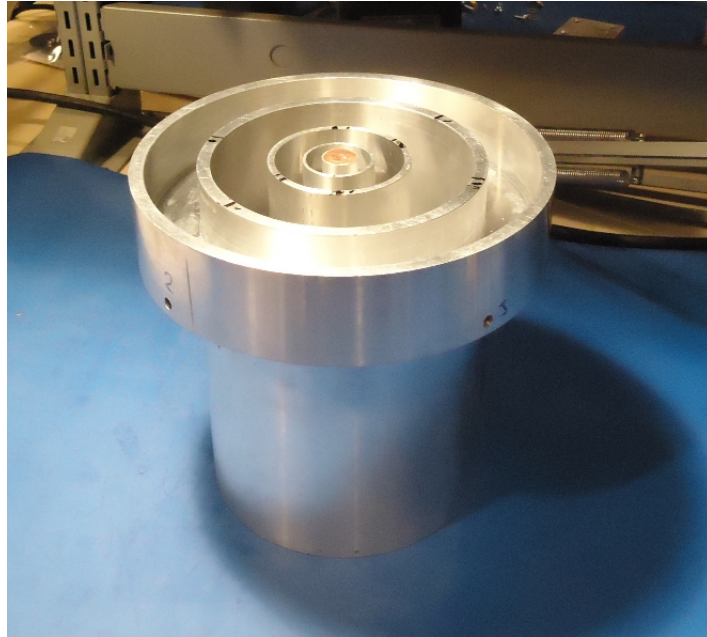


*Figure 6.1: Assembled Components of the Front Section*



*Figure 6.2: Inner Cylinders of the Front Section*

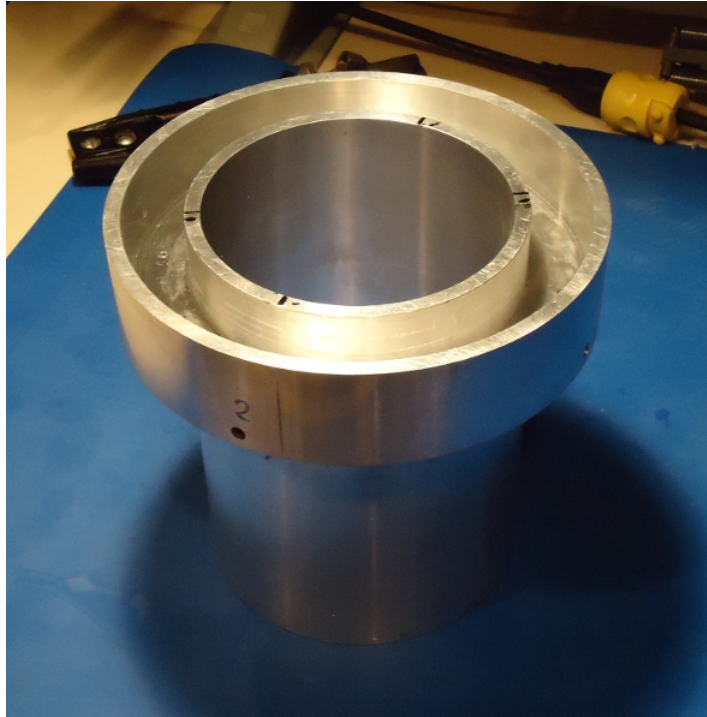


*Figure 6.3: Outer Cylinder of the Front Section with Choke Attached*

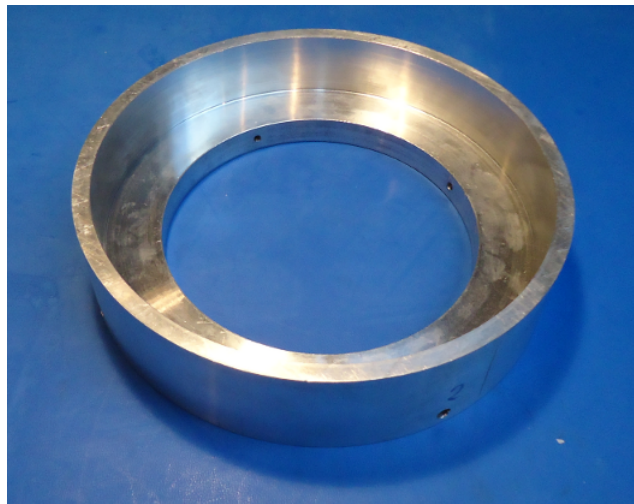


*Figure 6.4: Fabricated Choke*

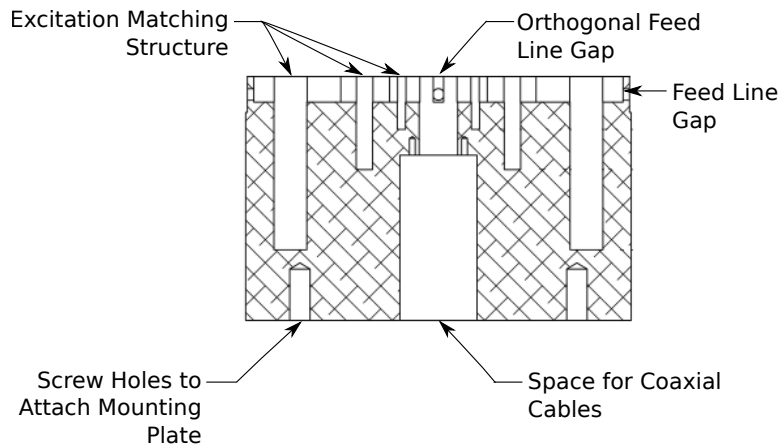


*Figure 6.5: Cross Section of the Back Section*

### 6.3 Assembling the Components

Two factors had to be considered in the design to facilitate the assembly of the prototype. First, the separate components had to be accurately positioned and aligned, and second, the components had to be secured together.

For positioning, three options were considered. The first option was to install pins into the front face of the back section and drill corresponding pin holes in the back face of the cylinders. The second option was to use either linear or concentric circular slots for positioning. The final option considered was to use no position mechanism and instead rely on the accuracy of the fasteners. For securing the components, two options were considered. One option was to use machine screws, and the other option was to use friction fit components. Friction fit components can use heat (thermal expansion) to aid in the assembly and ensure a tight fit once the components are cooled. Friction fastening methods require high precision machining of the components. Since this was a first prototype, the machine screw option was chosen for both positioning and fastening because this was the simplest option considered.

Screw sizes were determined largely by the thickness of the waveguide walls. The screw threads and clearances were selected to prevent cutting into adjacent waveguides. Number 6 coarse machine screws were chosen because they would fit between most waveguides. Number 6 coarse machine screws have 32 threads per

inch and are written as #6-32 in short hand. For inside the innermost waveguide wall, which is too narrow for the #6-32 screws, number four coarse (#4-40) machine screws were used as fasteners. Each cylinder was secured by four screws that were inserted from the back of the antenna. The screws were offset from the feed lines by 45° as shown in figure 6.6.

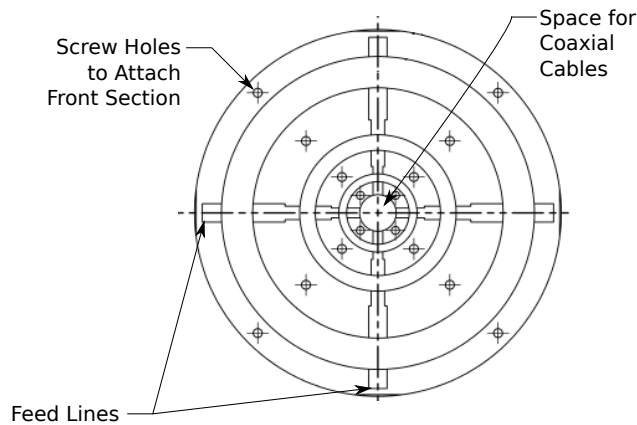


**Figure 6.6:** *Screw Locations to Secure Cylinders*

To attach the choke, #6-32 machine screws went through the choke and fastened into the sides of the outer cylinder. The thickness of the back wall of the choke was increased to allow room for clearance holes as shown in figure 6.7.



**Figure 6.7:** *Cross Section of Choke Showing Screw Clearances*

To mount the antenna for testing, a mounting plate like the one shown in figure 6.8 was used. 3/8" diameter coarse (#3/8-16) machine screws were used to attach the prototype to the mounting plate, as shown in figure 6.9. The back wall of the back section was increased in thickness to provide enough depth for the screw threads to be cut into the back face without cutting into any of the waveguides.



*Figure 6.8: Mounting Plate for Attaching Prototypes to Testing Equipment*

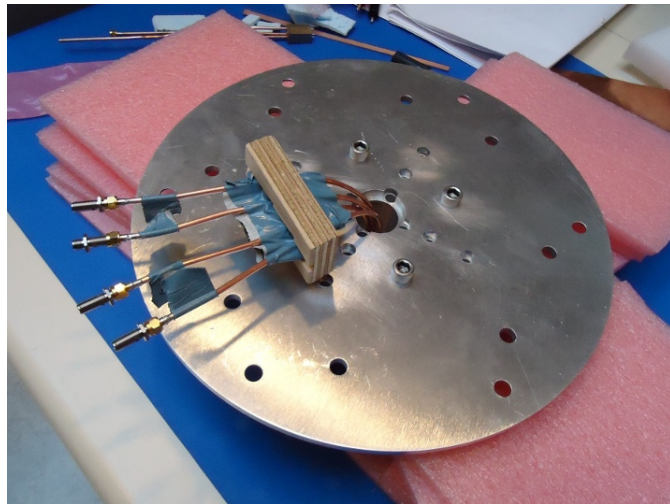


*Figure 6.9: Back Section Secured to the Mounting Plate*

## 6.4 The Feed Centre Assembly

The feed lines are connected to coaxial cables that run from the antenna to a balun, which provides the differential signal for the excitation structure. 0.141" Semi-rigid SMA cables with uninsulated copper shields were used for these connections.

SMA cables are run through the gap in the back of the antenna and connected to the feed lines in the centre of the antenna. A method was required to secure and ground the SMA cables to the body of the antenna. A plug was designed to be inserted into the centre of the back section and secured with machine screws. Brass was chosen as the material for the plug because it is easy to machine and can be soldered to. The plug, which is referred to as the "brass plug" in this thesis, is shown in figure 6.10. The plug has holes which the cables passed through and the outside shield of the cables is soldered to the plug. After the SMA cables are soldered, the resulting component is referred to as the "feed centre assembly". A flange with holes for securing the plug to the back section was added to the base of the plug. The centre conductor of the SMA cables extends beyond the plug to be connected to the feed line centre conductor with solder.

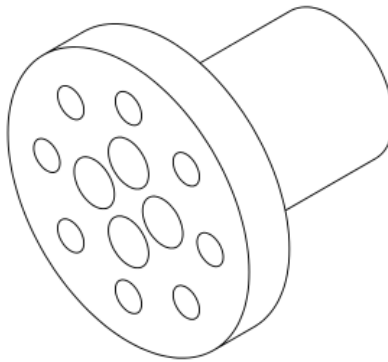


*Figure 6.10: The Brass Plug*

## Chapter 7

# Prototype Fabrication and Assembly

This chapter describes the process and equipment used to fabricate and assemble the prototype.

### 7.1 Fabricating the Components

The main components of the antenna were fabricated in the University of British Columbia (UBC) Okanagan Campus engineering machine shop. The front cylinders, choke, and back section were fabricated out of solid cylinders of aluminum. For the back section, the raw aluminum block was reduced to the correct radius and depth on an automated lathe machine (auto-lathe). The resulting block was then mounted on a CNC milling machine, and the excitation matching structure and the excitation gaps were milled out. The block was remounted to drill the screw holes and screw clearances for the mounting screws. The screw threads were tapped out by hand.

For the front cylinders, an auto-lathe was used to reduce the outside radius, bore out the centre of the cylinder, and cut out the matching steps to the correct radii. The CNC milling machine was used to drill the screw holes into the cylinders and the screw threads were tapped out by hand. Since the choke did not have an inner wall, it was also machined out using an auto-lathe.

The brass plug was machined with the auto-lathe and CNC milling machine. The combined feed line and excitation elements were fabricated from 1/8" sheet copper. Complex shapes can be easily cut from sheet metal using a CNC water-jet machine. One concern with the water-jet cutter was its ability to create parts as thin as 0.5 mm. Tests showed that the water-jet cutter could easily cut the narrow parts with very high accuracy. The parts cut with the water-jet cutting machine had a fine grainy feel to them and it was assumed this would not affect the results over the design frequency range. One of the excitation structures created with the water-jet cutter is shown in figure 7.1.



*Figure 7.1: Fabricated Combined Feed Line and Excitation Elements*

## **7.2 Building the Feed Centre Assembly**

As discussed in section 6.4, the feed lines are connected to four coaxial cables that run through the back of the antenna. 0.141" semi-rigid SMA cable was used because this cable is easy to work with and was readily available. Figure 7.2 and figure 7.3 show the cable preparation process. Four sections of this cable were cut to approximately the same length. The outer shield and insulation were stripped away from both ends of each cable using a device specifically designed for this type of cable. Male SMA connectors were then attached to one end of each cable using a jig to prevent the dielectric in the cables from expanding during soldering. The cables were then bent 90° for reasons that will become clear later.



*(a) Stripped SMA Cables*



*(b) SMA Connectors Attached on the Cables*

**Figure 7.2:** Preparing the SMA Cables for Assembly



**Figure 7.3:** Prepared SMA Cables

### 7.2.1 Testing the Feeding Cables

Each cable was marked with a number for tracking and then tested using a network analyzer.  $S_{11}$  was measured for each open circuit cable. Figure 7.4 shows the cables are well matched in  $S_{11}$  magnitude and it is difficult to see any significant difference between them. There is also good phase matching between the cables. All the cables exhibited resonant behaviour, which was caused by the stripped section at the end of each cable. The stripped sections were acting like quarter-wave monopole antennas. The frequencies that the resonance peaked at was consistent with the lengths of stripped cable. Since all the cables had similar responses, es-

pecially in the operating bandwidth of 1 GHz to 8 GHz, it was concluded that the mechanical shaping of the cables did not affect the impedance and phase match of the cables.

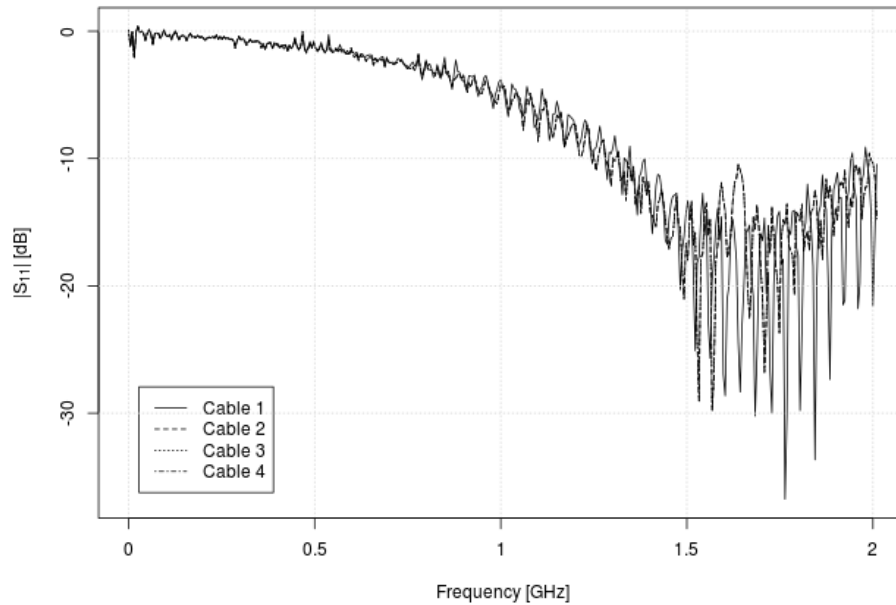


*Figure 7.4: Measured  $|S_{11}|$  for the Four Feeding Cables*

### 7.2.2 Assembling the Feed Centre Assembly

Assembling the feed centre assembly was a significant challenge. Assembly required that the shield of the feeding cables be soldered to the plug. The plug has significant thermal mass and it was difficult to heat it up enough to make good solder joints. A test plug was fabricated and used to evaluate different methods for soldering. All the evaluated methods either did not produce enough heat or caused the dielectric in the cables to expand significantly.

Instead, silver epoxy was used as a conductive adhesive to bond the cables to the plug and create a good electrical connection without the use of heat. The open end of the cables were coated with epoxy and inserted into the plugs. The free ends

of the cables were held in position while the epoxy set. After the epoxy set, the epoxy bonds were tested for physical strength. The bend in the cables acted like a lever and any force put on the end of the cables put significant torque on the epoxy bonds. There was insufficient physical strength in the epoxy bonds to support the baluns. This may have been because the epoxy used was near the end of its shelf life. Reinforcement of the bonds was required to mitigate the risk of the feeding cables becoming loose during testing. Due to time constraints, a rig was quickly made of wood and duct tape to reinforce the feed centre assembly. The completed feed centre assembly is shown in figure 7.5.

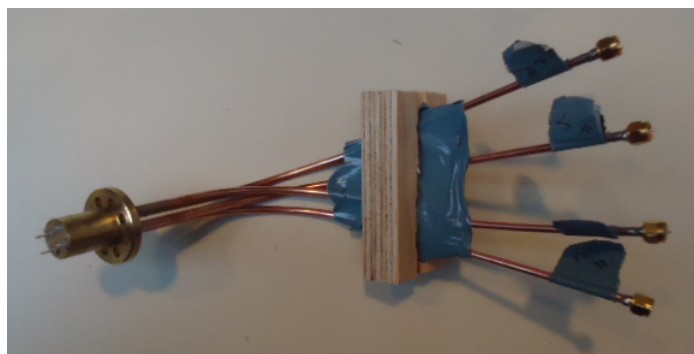


*Figure 7.5: Assembled Feed Assembly*

$S_{11}$  was measured again on the network analyzer and it was found that all four cables had comparable performance. This verified that each cable's shield had a good electrical connection to the plug and none of the cables' centre conductors were shorted by the epoxy.

### **7.3 Assembling the Full Prototype**

The next step in the assembly process was to attach the mounting plate to the back section. Before the mounting plate was attached, holes were drilled in the mounting plate that aligned with the screw clearances in the back section. The mounting plate was then secured with machine screws and the feed centre assembly was inserted into place and temporarily secured. This is shown in figure 7.6 and figure 7.7. The SMA connectors were placed on the sides of the back section and secured with screws.

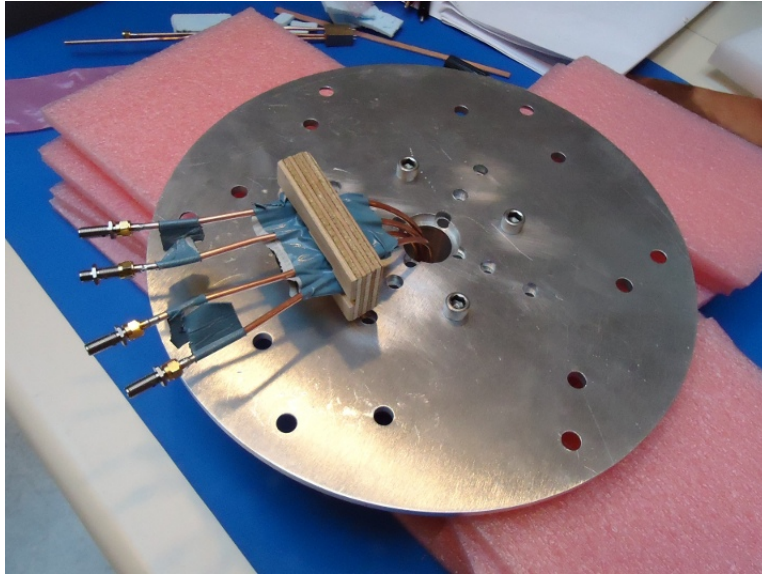


*Figure 7.6: Back View of Assembled Back Section and Mounting Plate*

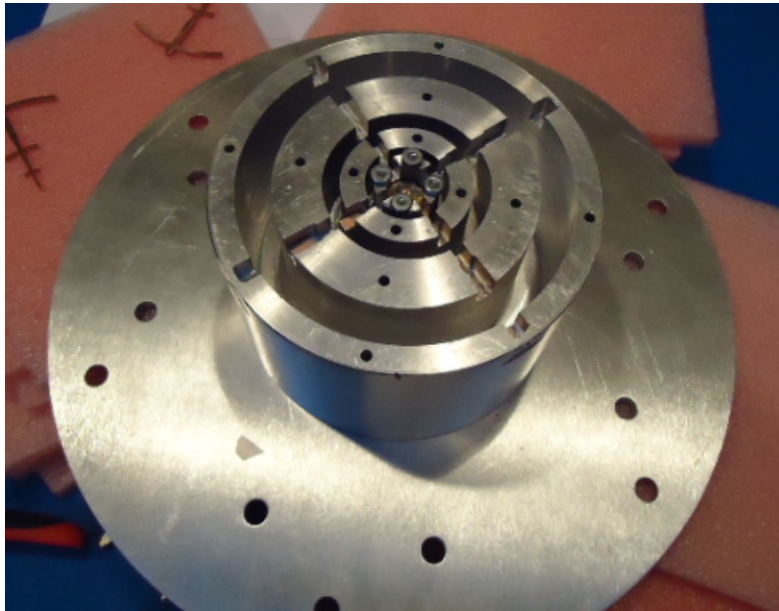


*Figure 7.7: Front View of Assembled Back Section and Mounting Plate*

To position the excitation structures correctly, spacers that could withstand the heat from soldering were needed. To achieve the correct distance from the cross pieces to the waveguide walls, drill bits were used as spacers. To position the excitation structure at the correct height in the feed gap, spacers were constructed out of small pieces of printed circuit board (PCB) wrapped in ruban tape until it reached the correct thickness. Once the spacers were in place, the excitation structure was inserted then centred in the feed gap. The excitation structure was held in place by hand while the two ends of the feed line were soldered to the connection points. The spacers were then removed. This procedure was repeated for the other three excitation structures and the positions were verified using a caliper. The solder connection to the feed centre assembly are shown in figure 7.8 and the completed back section is shown in figures 7.9 to 7.11.

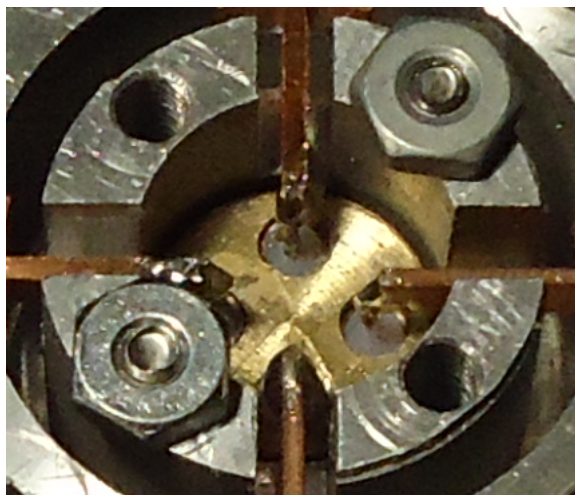


*Figure 7.8: Connections to Feed Line*

The final step of the assembly procedure was to secure the front cylinders and the choke. The front cylinders were positioned by hand and secured in place with machine screws. Since the cylinders are circularly symmetric, the only position requirement is that the screw holes line up. After all the cylinders were attached, the choke was seated on the outermost cylinder and was secured with machine screws, as shown in figure 7.12 and figure 7.13. This completed the prototype assembly procedure.



*Figure 7.9: Excitation Structure Soldered in Position*

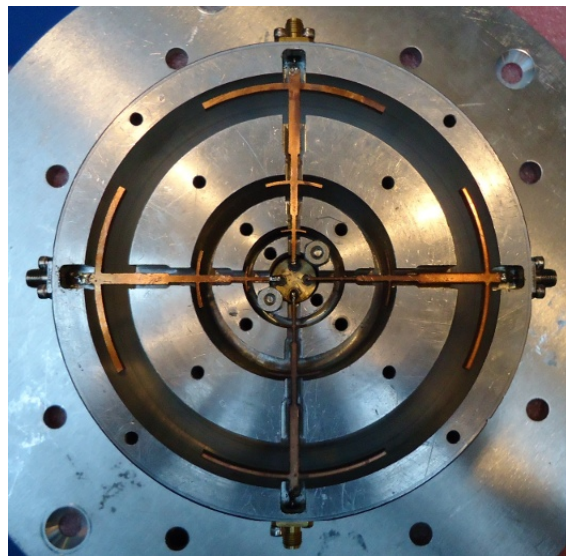


*Figure 7.10: Fully Assembled Back Section*

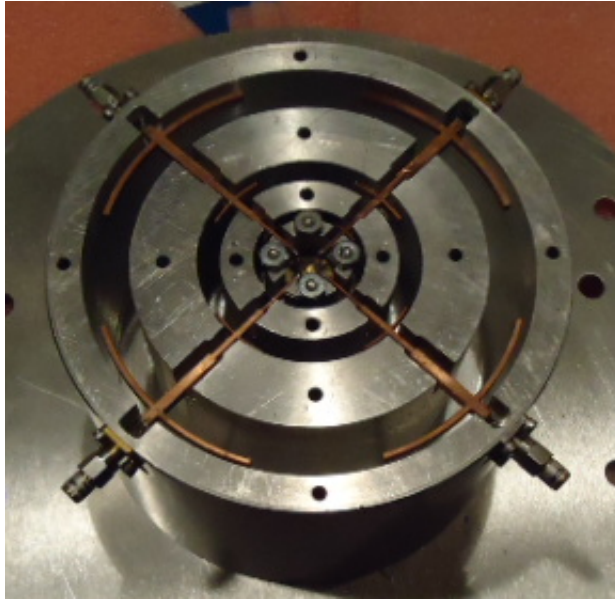


*Figure 7.11: Fully Assembled Back Section with 50  $\Omega$  Terminations*

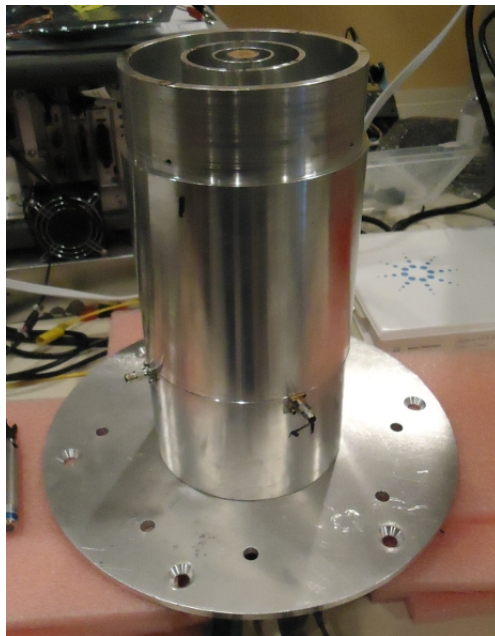


*Figure 7.12: Front Section Attached without Choke*

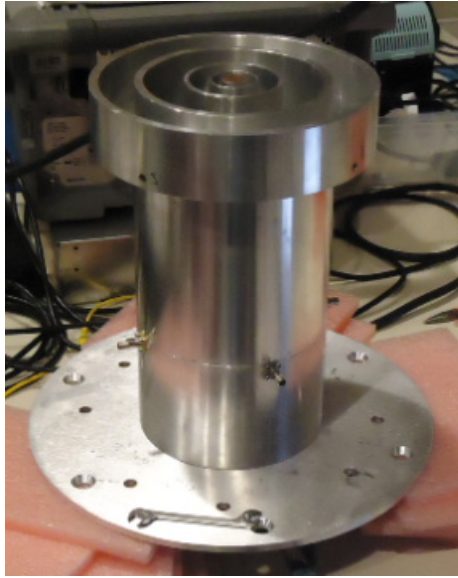


*Figure 7.13: Front Section Attached with Choke*

## Chapter 8

# Prototype Testing

This chapter outlines the testing procedures used during this project. The purpose of constructing and testing the prototype was to verify the accuracy of the simulation software for this design, specifically in regard to farfield patterns and return loss. A series of bench tests was conducted using a network analyzer to measure the input return loss of the prototype. Subsequently, a large number of nearfield radiation patterns were measured in a nearfield anechoic chamber. The farfield radiation patterns were then derived.

### 8.1 Network Analyzer Tests

The electrical performance of the prototype was tested with an Agilent model N5230A network analyzer. Figure 8.1 shows the test setup. A block of electromagnetically transparent foam was placed at the aperture of the waveguide to give the electromagnetic field space to form. Several blocks of radio absorbing foam were then placed on top of the electromagnetically transparent foam. The radio absorbing foam provided a way to measure the input return loss of the operating prototype without having to move the prototyping into an anechoic chamber.

The network analyzer has a feature that configures a pair of ports into a simulated differential port. The differential port provides two oppositely phased signals to drive the excitation structure. To verify this function, an experiment was conducted comparing the performance of the differential port to the performance of a

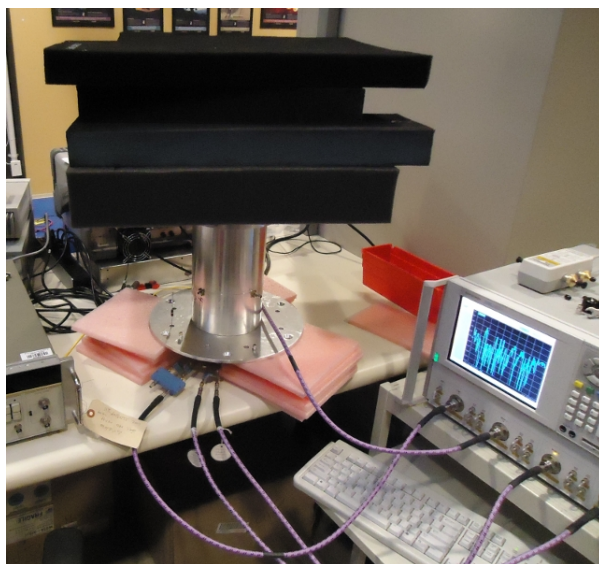


**Figure 8.1:** Simulated Differential Port Test Setup with Absorbing Foam

single port with a balun.

For this experiment, a number of Pulsar Microwave Corporation hybrid devices were used. A hybrid is a four port device that can split power equally to two output ports either in phase (SUM) or  $180^\circ$  out of phase (DELTA). Since hybrids are passive devices, they can also sum power in either the SUM or DELTA configuration. The manufacturer's specifications for the baluns are shown in table 8.1. It was a coincidence that the bandwidth of the hybrids exactly matched the bandwidth of each waveguide in the antenna.

The first step in the experiment was to verify that both polarizations of the prototype have equivalent performance. This was done by exciting both polarizations with simulated differential ports as shown in figure 8.2. The performance of the two polarizations were similar, within  $\pm 0.5$  dB for most frequencies, implying that the excitation structures for both polarization were physically very similar.

A side by side test was then performed by exciting one polarization using a hybrid, and the other polarization using a simulated differential port. This set up is shown in figure 8.1. The results for each frequency band are shown in figures 8.3 to 8.5.

**Table 8.1:** *Manufacturer's Specification for Hybrids*

Frequency Band	Frequency Range (GHz)	Insertion Loss (dB)MIN	Amplitude Balance ( $\pm$ dB) MAX	Phase Balance ( $\pm$ Deg) MAX	VSWR	P/N
Band 1	1 – 2	0.6	0.5	8.0	1.40:1	JSO-01-465/3S
Band 2	2 – 4	0.6	0.5	10.0	1.60:1	JSO-02-465/1S
Band 3	4 – 8	0.6	0.5	10.0	1.90:1	JSO-03-465/5S

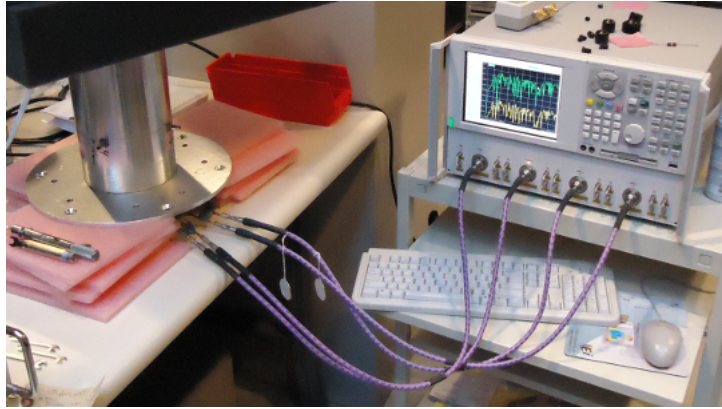


**Figure 8.2:** Test Setup for Comparing the Performance of the Polarizations

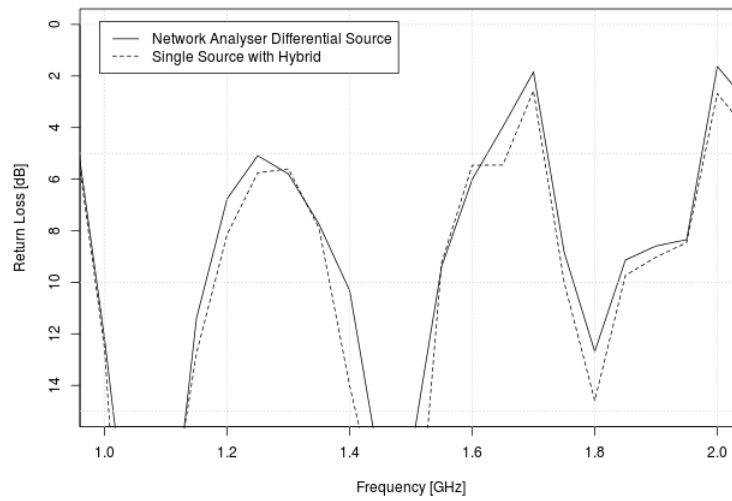


**Figure 8.3:** Comparing the Network Analyzer Differential Source to a Single Source with Hybrid for Band One

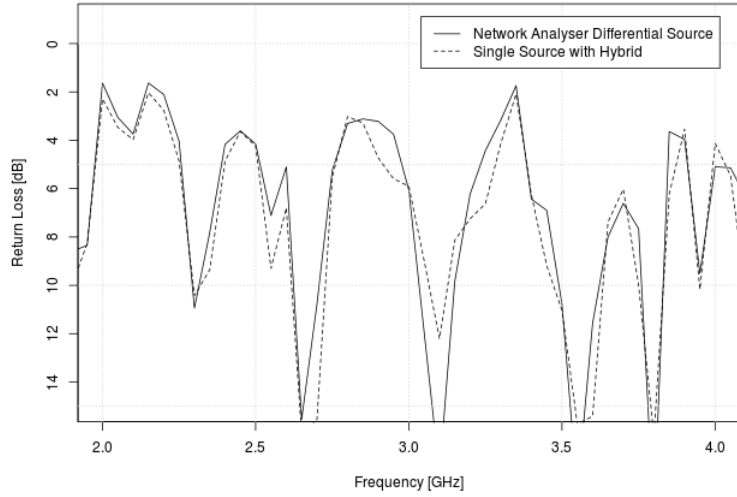


**Figure 8.4:** Comparing the Network Analyser Differential Source to a Single Source with Hybrid for Band Two

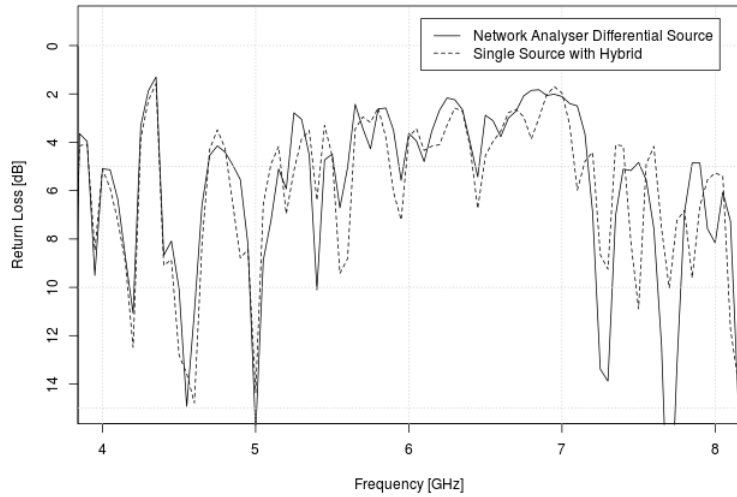


**Figure 8.5:** Comparing the Network Analyser Differential Source to a Single Source with Hybrid for Band Three

These figures demonstrate that the network analyzer's simulated differential port successfully emulates a balun. The only notable differences are a slight change in the amplitude and some resonance spikes at high frequency. These can be attributed to the performance of the hybrids themselves and the physical difficulties in producing radio frequency components that operate at high frequencies.

Since the network analyzer's simulated differential ports were found to have equivalent performance to that of the hybrids, the differential ports were used for all remaining network analyzer tests.

### 8.1.1 Alternative Feed Line Termination Tests

During the network analyzer tests, multiple feed line terminations were tested. For matched terminations, conventional 50  $\Omega$  SMA loads (figure 8.6a) were used. Short circuit terminations were created by modifying SMA ports (figure 8.6b) and then tested. Finally, open circuit terminations, which require no additional hardware, were tested.



(a) 50  $\Omega$   
Termination



(b) Short-Circuit  
Termination

**Figure 8.6:** Feed Line Terminations for Bench Tests

### 8.1.2 Addressing the Return Loss Shortfall

In testing, it was determined that the return loss magnitude was significantly below the expected value. One possible reason for this shortfall was the empty space at the centre of the excitation structure (see figure 7.8). The feed line connections

and this open space were not included in the electrical design simulations. After the prototype was fully tested in the anechoic chamber, the prototype was modified in an attempt to remove this space. A filler plug was machined out of brass and installed into the back section, as shown in figure 8.7 and figure 8.8. The filler plug was held in place using copper tape as shown in figure 8.9. In addition to securing the filler plug, the copper tape serves to form a solid electrical connection between the filler plug and the back section.



*Figure 8.7: Fabricated Brass Filler Plug*

## **8.2 Farfield Testing**

To test the farfield patterns of the prototype, nearfield patterns were measured in an anechoic chamber located at DRAO. A computational transformation was then applied to the nearfield data to derive the farfield patterns. More information on nearfield antenna measurements and the nearfield-to-farfield transformation can be found in [28] and [31]. The anechoic chamber used for the test is shown in figure 8.10.

An anechoic chamber is a room designed to simulate free space. To achieve this, the chamber minimizes the reflection of signals by covering the floor, walls,

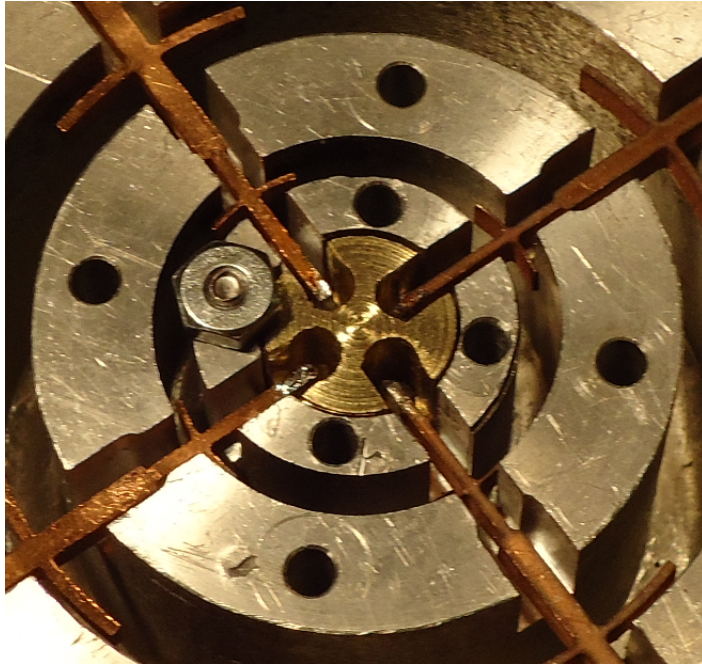


*Figure 8.8: Brass Filler Plug Installed in Back Section*

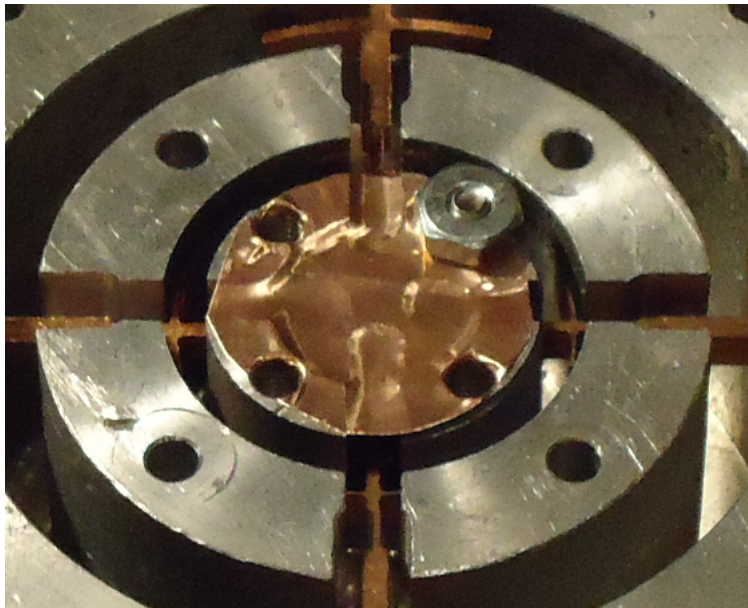


*Figure 8.9: Brass Filler Plug Secured with Copper Tape*

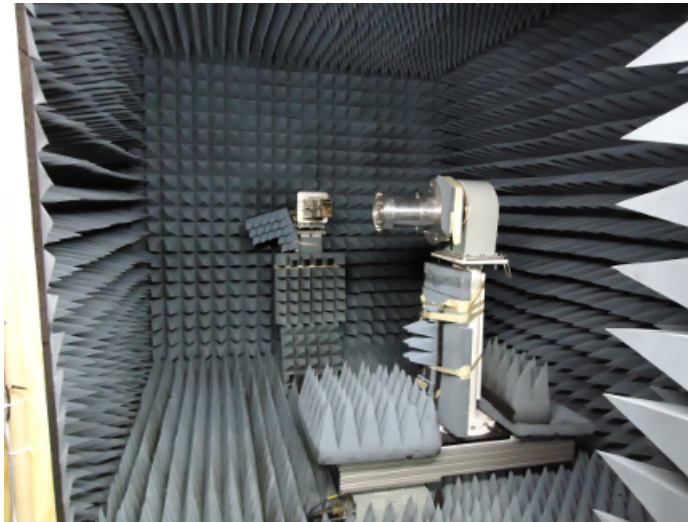


*Figure 8.10: The Anechoic Chamber at DRAO*

and roof with radio absorbing material. The absorbing material is not completely effective at absorbing all signals that strike it. To increase the absorbing efficiency, the material is shaped into pyramids that are angled such that the signal strikes and reflects back into the material multiple times before being reflected back into the chamber. The anechoic chamber is equipped with two positioners, a prototype positioner with two degrees of freedom (azimuth and roll) and a probe positioner with one degree of freedom (roll). The prototype is mounted onto the prototype positioner using a mounting plate. One of a set of interchangeable test probes is mounted onto the probe positioner.

A computer outside the anechoic chamber controls the movements of the positioners and collects data directly from a network analyzer. The network analyzer is located outside the anechoic chamber and is connected to both the prototype and the probe through cables embedded inside the positioners.

As shown in figure 8.11, the network analyzer used by the anechoic chamber is not as advanced as the network analyzer used in the bench tests and only has two ports. To provide the required differential signal to the prototype, the hybrids specified in table 8.1 were used. Figure 8.12 shows one of the hybrids feeding the prototype antenna with radio absorbing material attached to prevent signals

reflected off the hybrid.



**Figure 8.11:** Network Analyzer (Top) and Motor Controller (Bottom) for the Anechoic Chamber

The probes used for testing this prototype were rectangular waveguides with the specifications shown in table 8.2. A mounting plate was used to secure the probe onto the probe positioner. The SMA cable embedded in the positioner was connected to the probe as shown in figure 8.13. The probe mounting plate was covered with a piece of radio absorbing material as shown in figure 8.14.

The computer in the antenna laboratory uses the proprietary software listed in table 8.3 to control the positioners and collect the nearfield data. The 959Spectrum software reads the network analyzer data for each position of the prototype and probe, and records the signal amplitude at the frequencies specified by the user. These measurements are the nearfield data for the prototype. The SpectrumAnalysis software takes the nearfield data and using a number of physical parameters entered by the user performs a computational transformation that translates the nearfield data to the corresponding farfield data. The nearfield data and farfield data can be shown graphically in SpectrumAnalysis, but for this project the data

was exported into an ASCII format. The ASCII files were parsed, analyzed, and plotted using scripts.



*Figure 8.12: Balun Attached to the Prototype and Shielded by Radio Absorbing Material*

*Table 8.2: Specification of Probes Used for Nearfield Measurements*

Make / Model	SN / PN	Frequency Range [GHz]	Length [mm]
Orbit/FR AL-PRB-770	SN: 770-1001	0.95 – 1.45	595
Orbit/FR AL-PRB-510	SN: 510-1001	1.45 – 2.2	595
NSI-RF-WR340	N/A	2.2 – 3.3	677
NSI-RF-WR229	N/A	3.3 – 4.9	522
NSI-RF-WR159	N/A	4.9 – 7.05	403
MI-6970-WR112	SN: 2484 PN: 584800-007	7.05 – 10.0	N/A

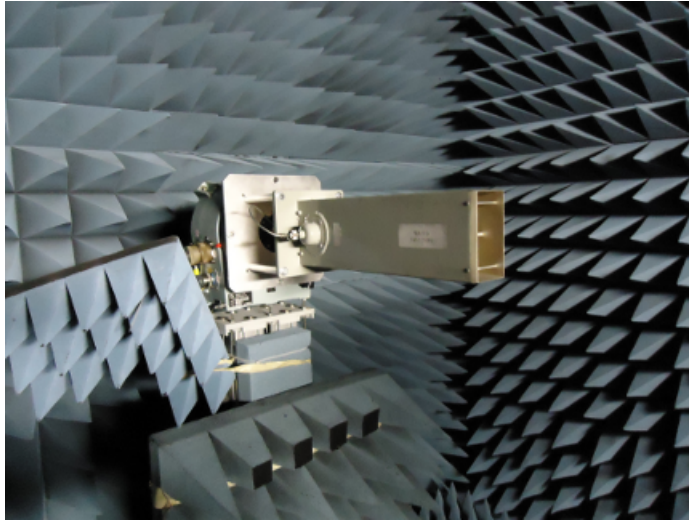


*Figure 8.13: Probe in the Anechoic Chamber*

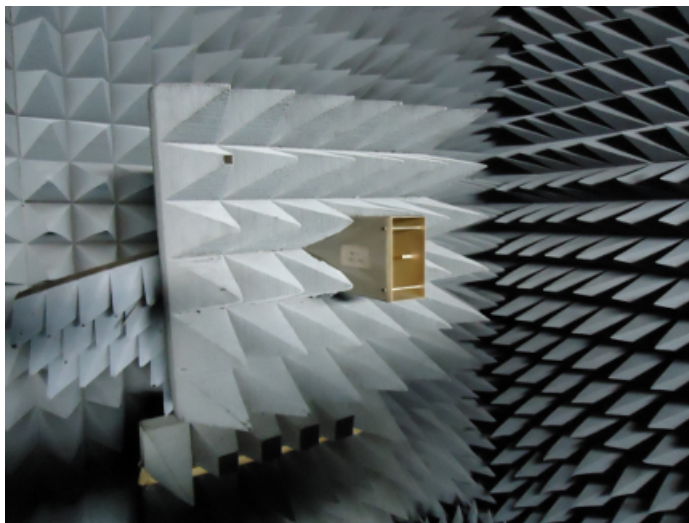


*Figure 8.14: Probe in the Anechoic Chamber with Radio Absorbing Material*

**Table 8.3:** *Software Used in the Antenna Laboratory*

Program	Provider	Version	Purpose
959Spectrum	Orbit/FR	5.0.6	Controls Positioners and Collects Data
SpectrumAnalysis	Orbit/FR	50.806.15	Converts Nearfield Data to Farfield

# Chapter 9

## Results

This chapter summarizes the data collected for the feed antenna design. Data includes simulation results as well as experimental results for the prototype.

### 9.1 Return Loss

The return loss for the simulated electrical design is shown in figure 9.1. Figure 9.2 shows the experimental return loss for the prototype. For comparison, the return loss of the prototype is shown with short circuit feed line terminations (figure 9.3) and open circuit feed line terminations (figure 9.4). As discussed in section 8.1.2, a modification was made to the centre of the excitation structure to try to bring the experimental return loss closer to the simulated result. The return loss after this modification is shown in figure 9.5.

### 9.2 Farfield Results

The farfields are plotted using the E-plane and H-plane cuts to present the co-polarization component of the farfield, and the  $\phi = 45^\circ$  cut to present the cross-polarization component of the farfield. In linearly polarized antennas, the E-plane is defined as the plane containing the electric field vector at the excitation source, which was  $\phi = 90^\circ$  in both the simulation and experimental setups. The H-plane is defined as the plane perpendicular to the E-plane, which was  $\phi = 0^\circ$  in both the simulation and experimental setups. These three cuts are the conventional views

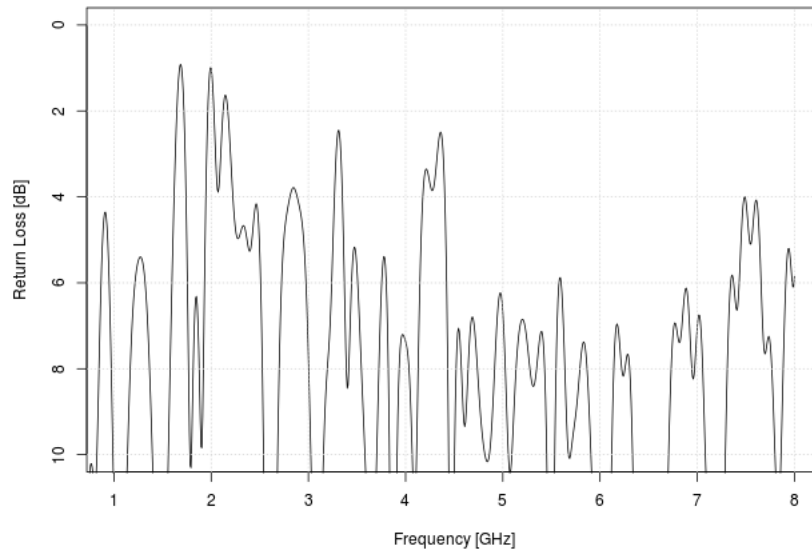


**Figure 9.1:** *Simulated Return Loss*

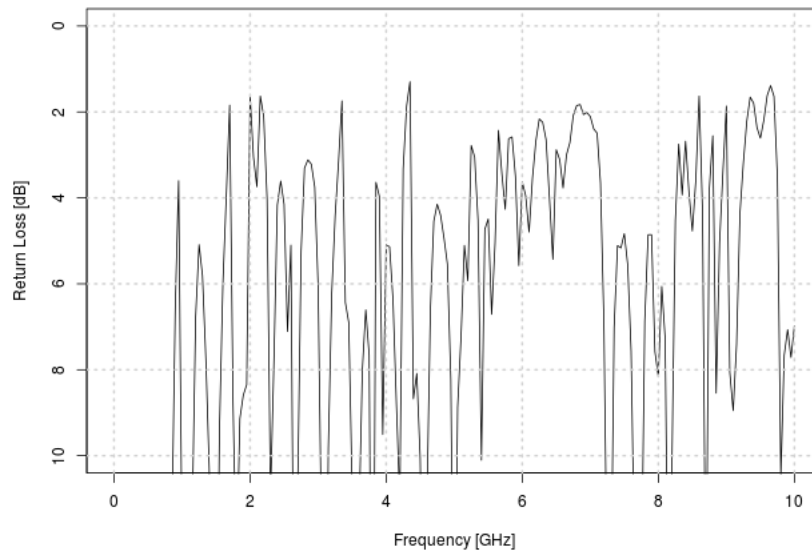


**Figure 9.2:** *Experimental Return Loss Using 50 Ω Feed Line Terminations*

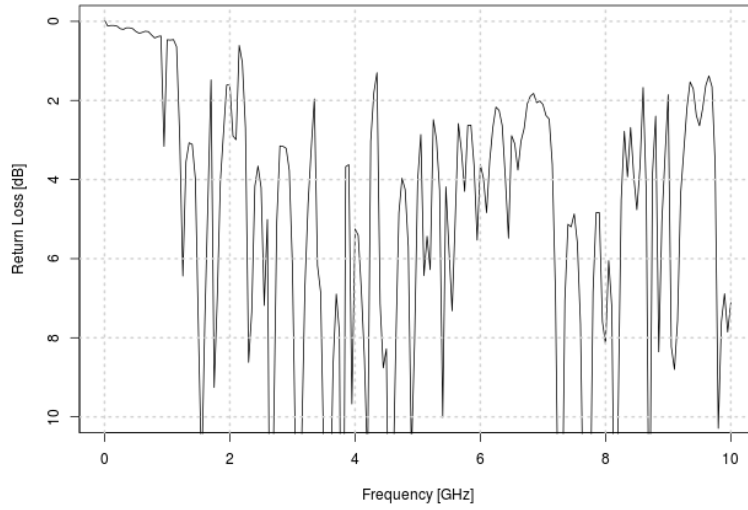


**Figure 9.3:** *Experimental Return Loss Using Short Circuit Feed Line Terminations*

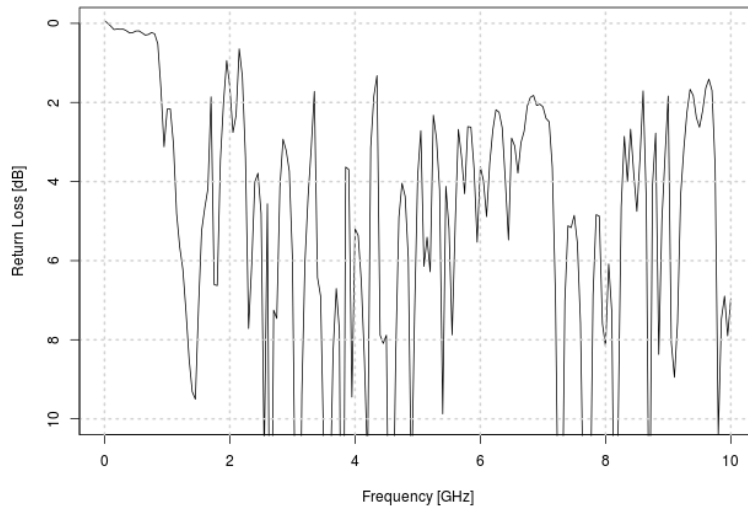


**Figure 9.4:** *Experimental Return Loss Using Open Circuit Feed Line Terminations*

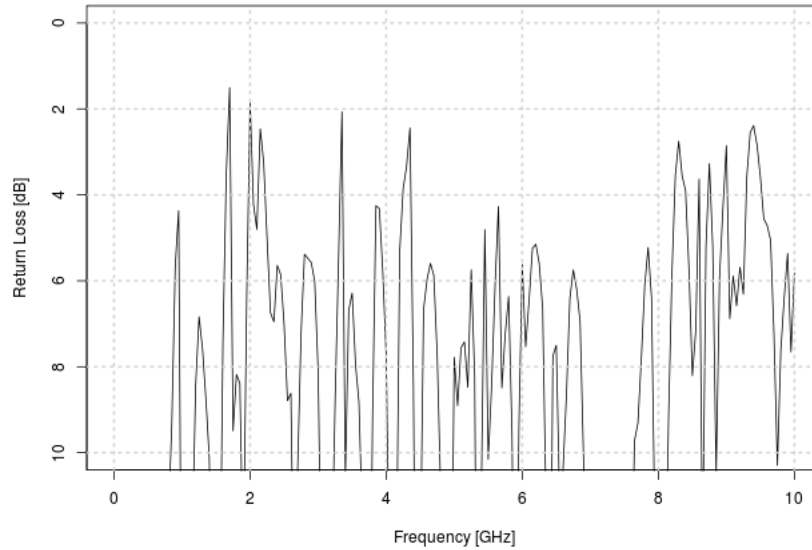


**Figure 9.5:** *Prototype Return Loss of Prototype with Feed Line Modifications*

for antenna farfields, as they normally contain the extrema of the farfield patterns. Additionally, all the farfield patterns are normalized to the magnitude of the E-plane at the boresight.

Figures 9.6 to 9.9 shows the results from the simulations of the electrical design. Since the simulated patterns are symmetric about  $\theta = 0^\circ$ , only half of each pattern is shown to allow all three cuts to be shown on the same figure. In order to save space, four frequency samples are shown per figure.

The experimental farfield patterns are shown in figures 9.10 to 9.17. Unlike the simulation results, the experimental farfield patterns are not symmetric, and are broken into two sets of figures; one showing the E-plane and cross-polarization graphs, and the other showing the H-plane graphs.

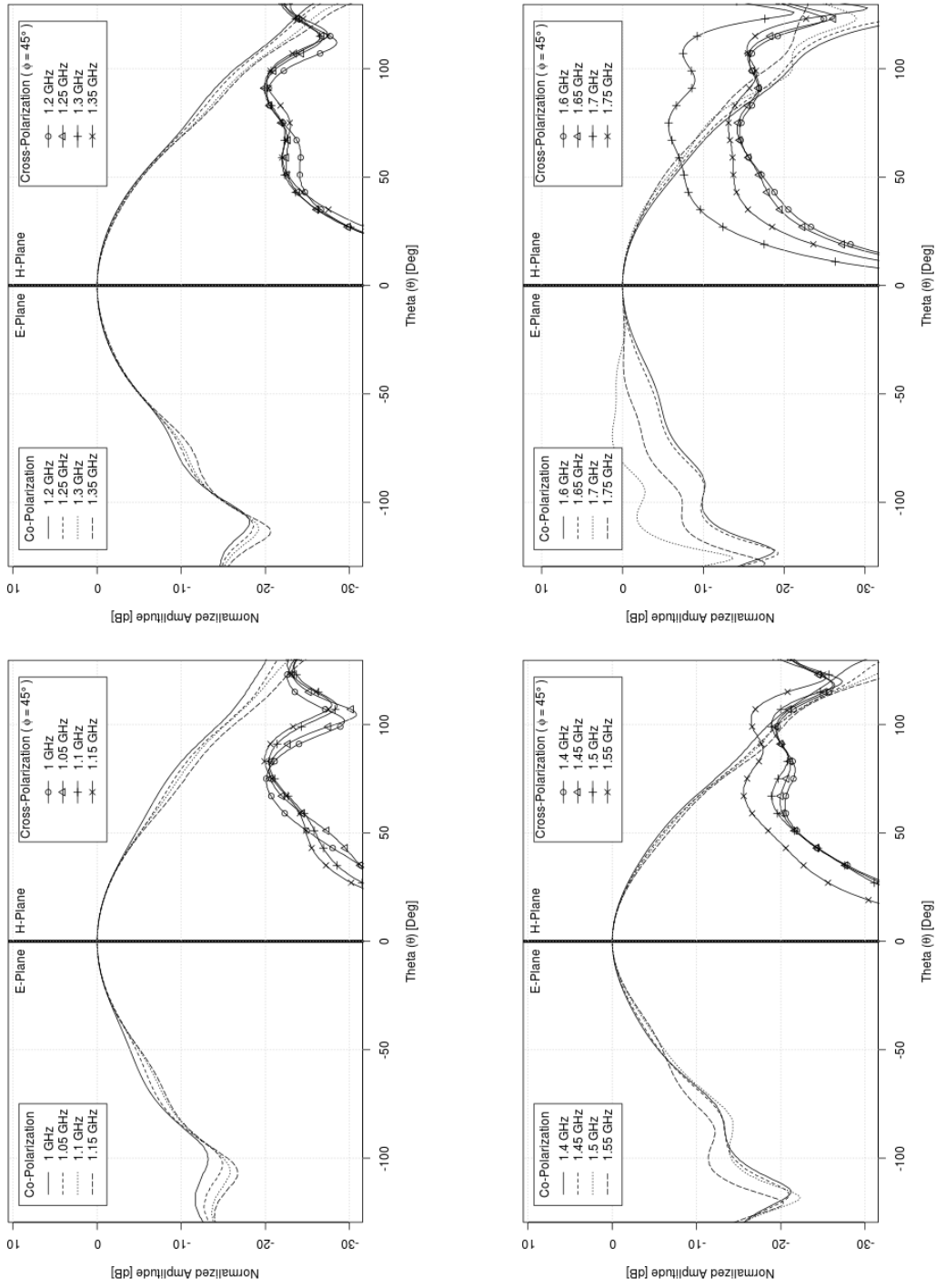


Figure 9.6: Simulated Farfield Patterns

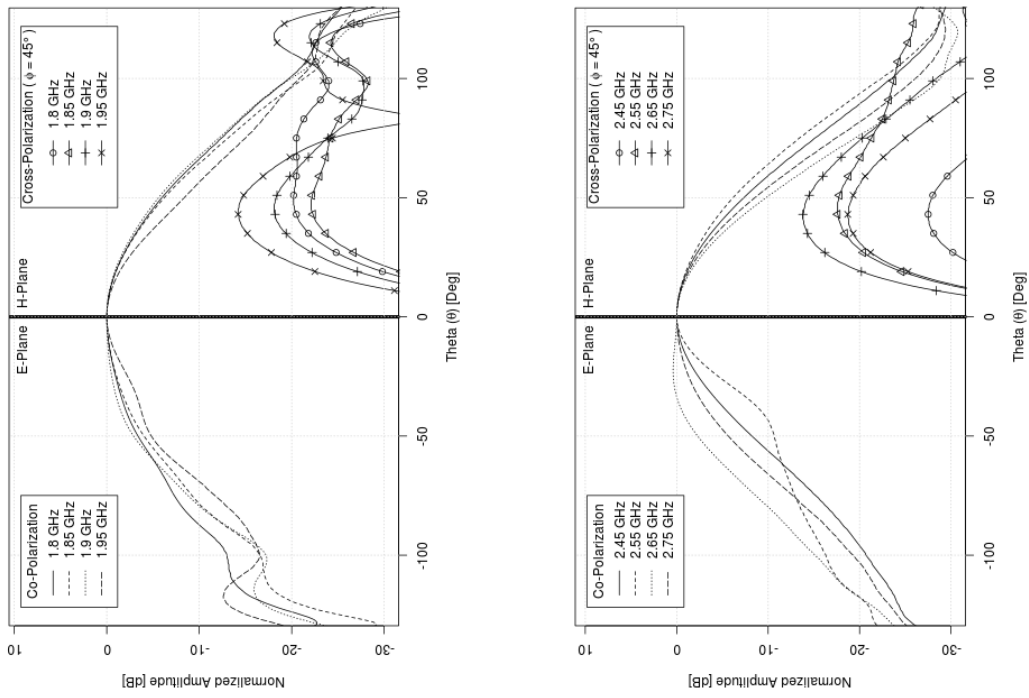
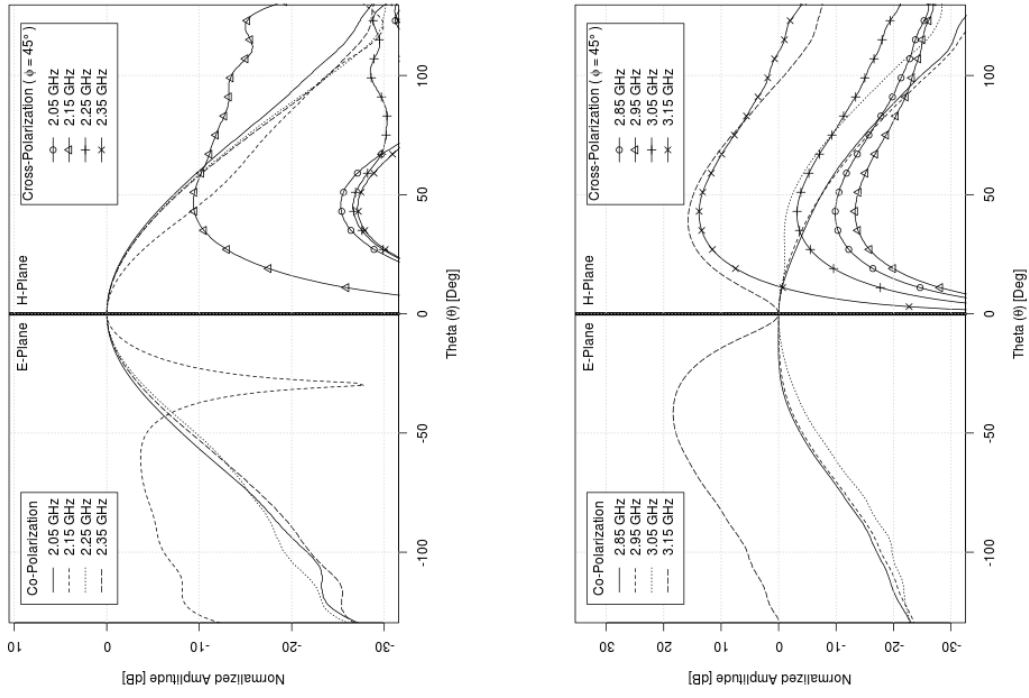


Figure 9.7: Simulated Farfield Patterns

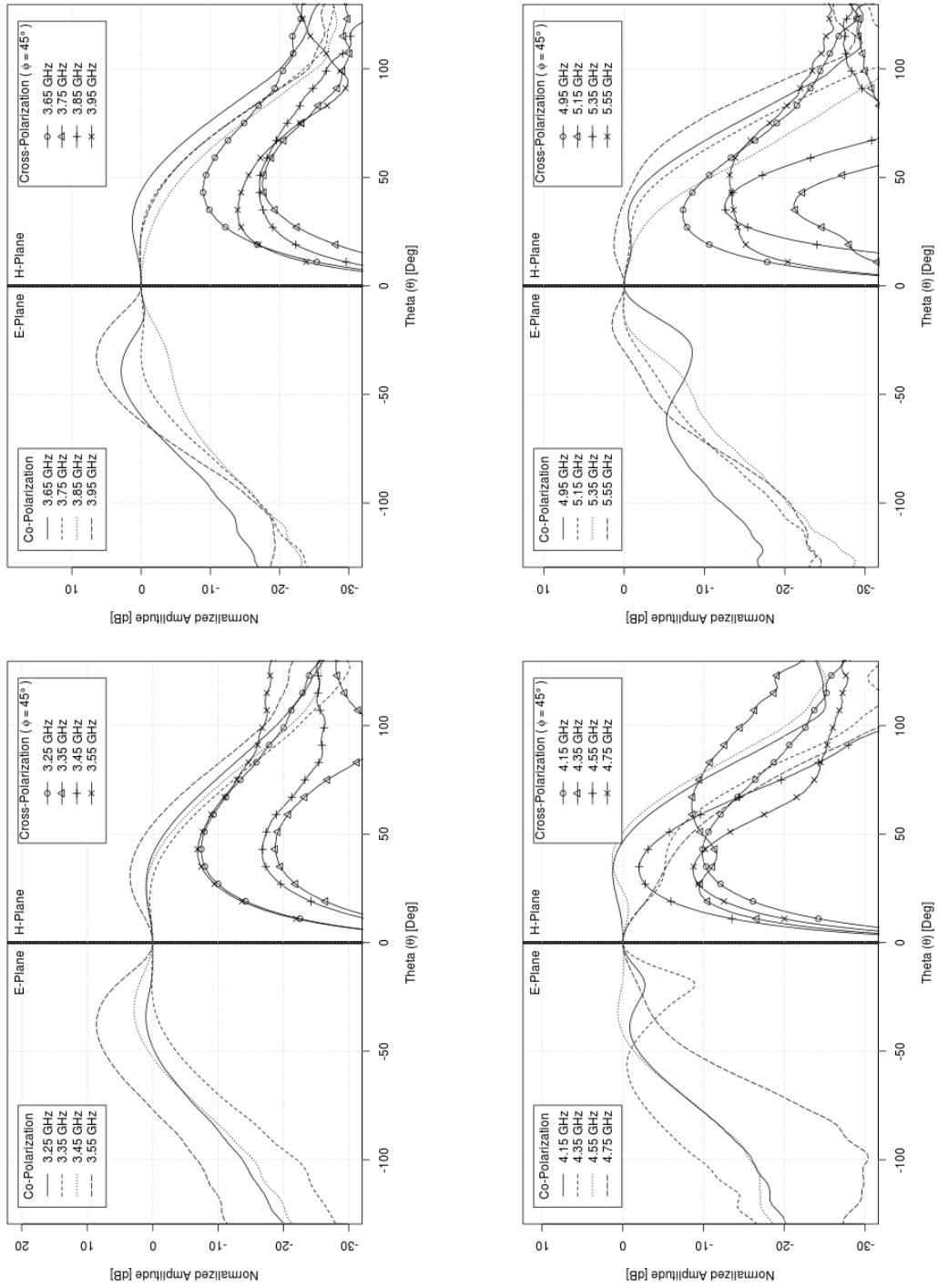


Figure 9.8: Simulated Farfield Patterns

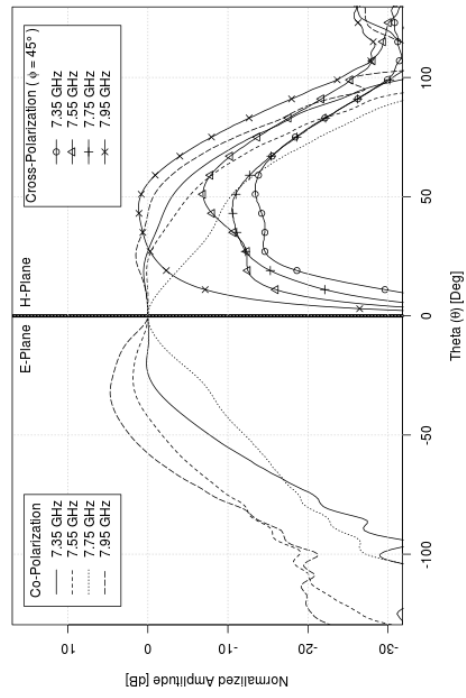
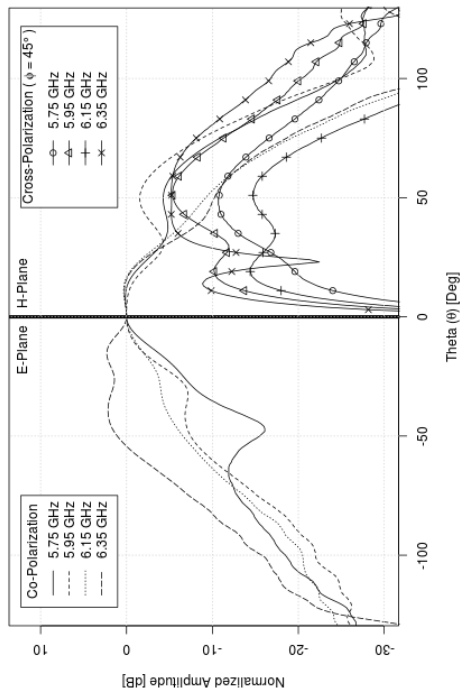
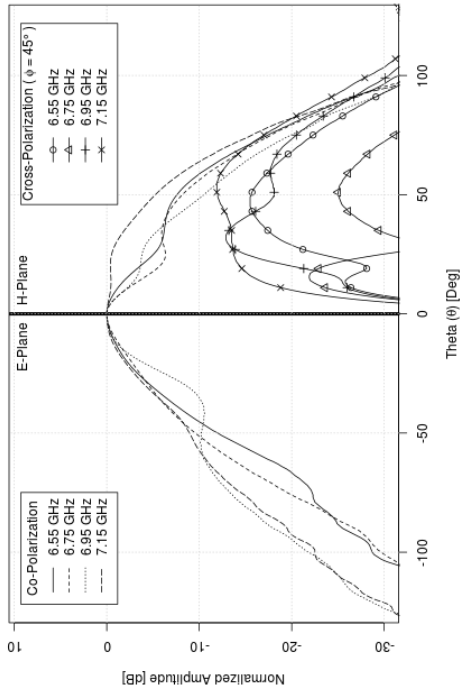
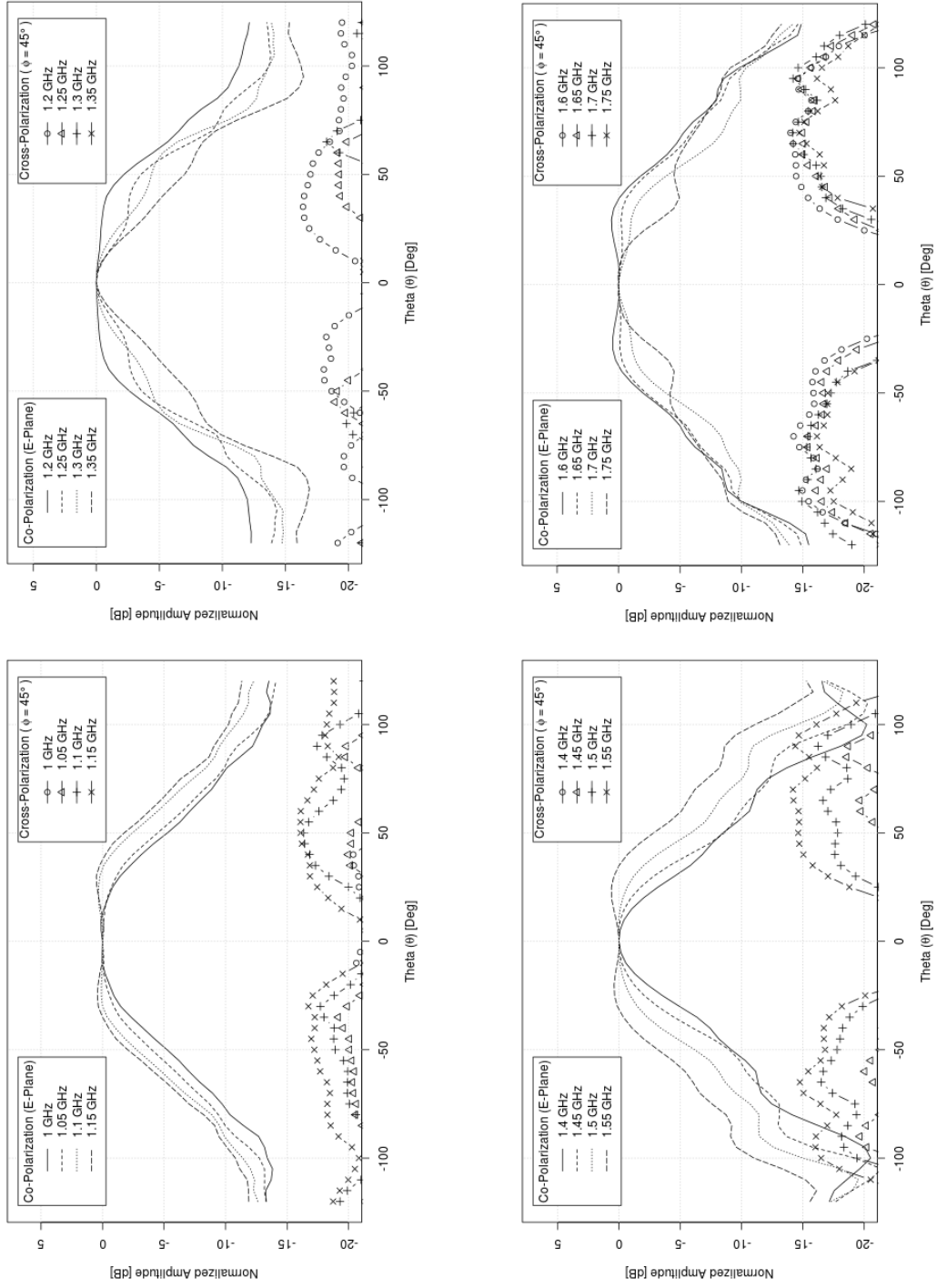
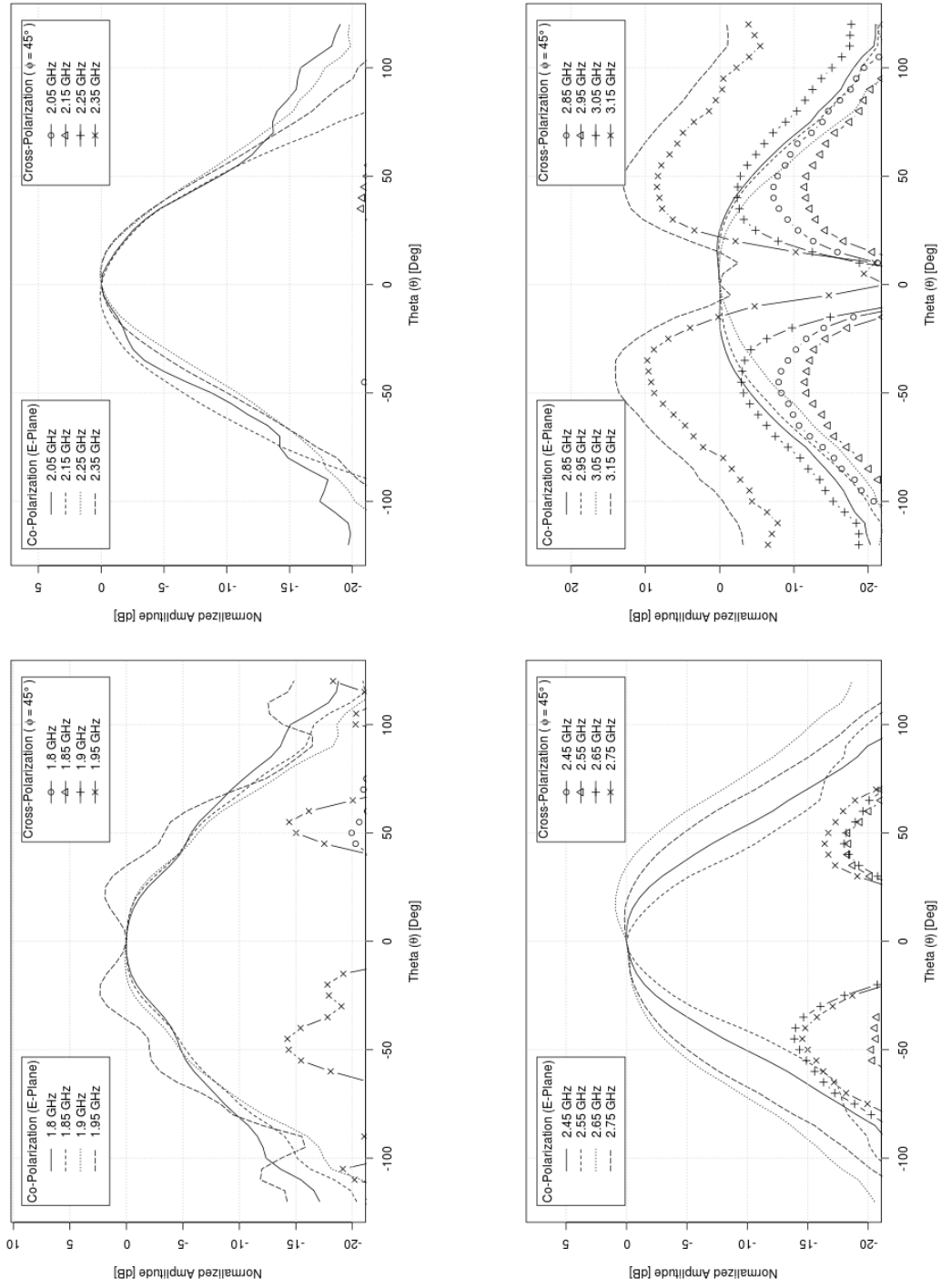


Figure 9.9: Simulated Farfield Patterns



**Figure 9.10:** Experimental Farfield Patterns – E-Plane Co-Polarization and Cross-Polarization



**Figure 9.11:** Experimental Farfield Patterns – E-Plane Co-Polarization and Cross-Polarization

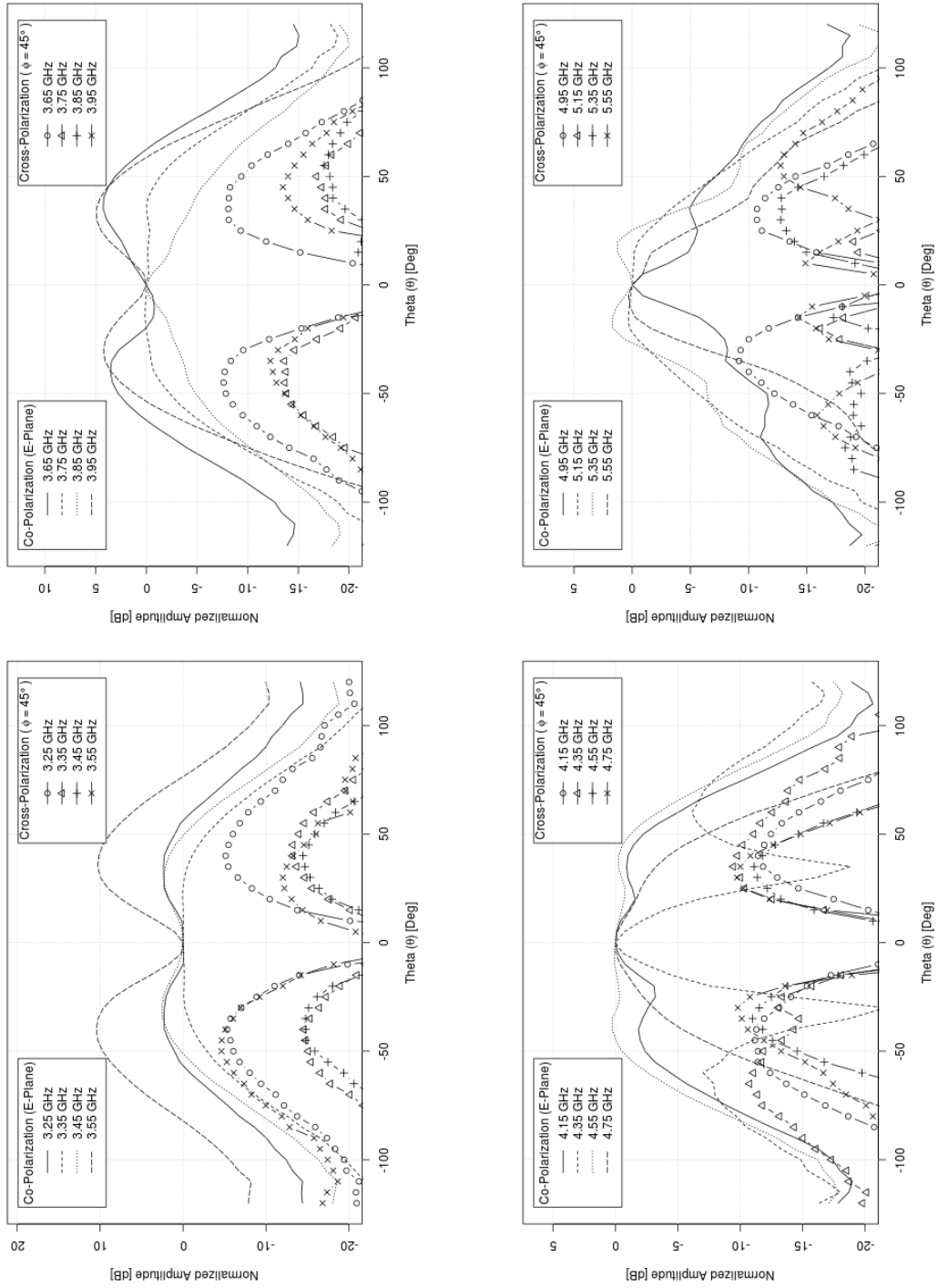


**Figure 9.12:** Experimental Farfield Patterns – E-Plane Co-Polarization and Cross-Polarization

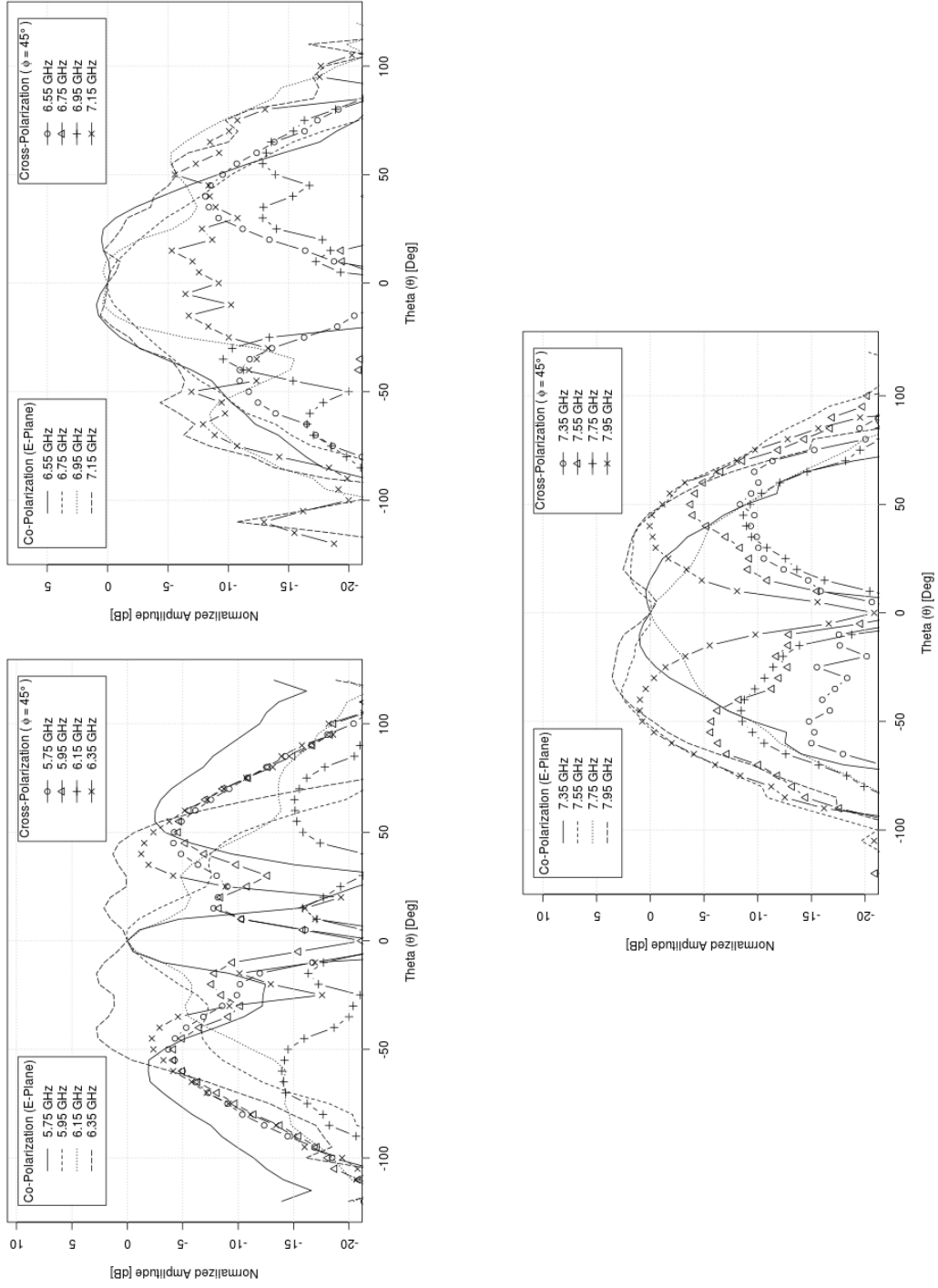


**Figure 9.13:** Experimental Farfield Patterns – E-Plane Co-Polarization and Cross-Polarization

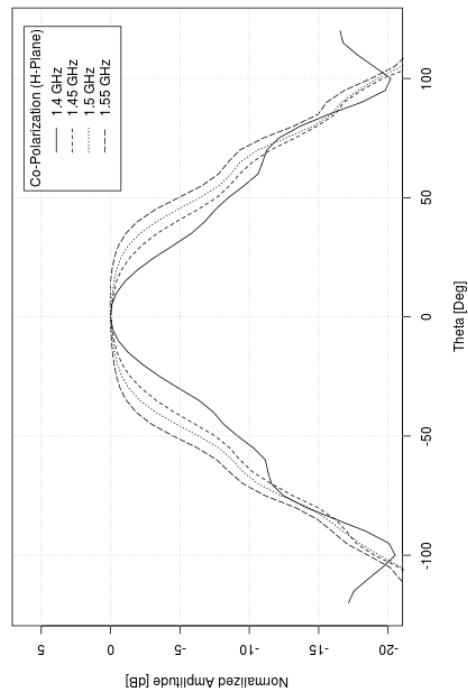
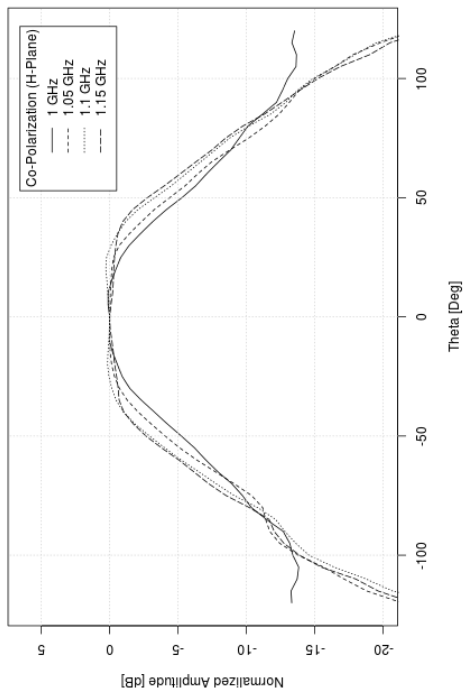
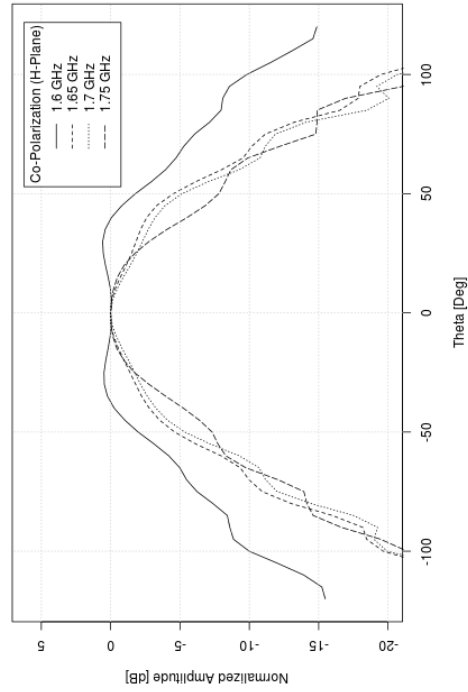
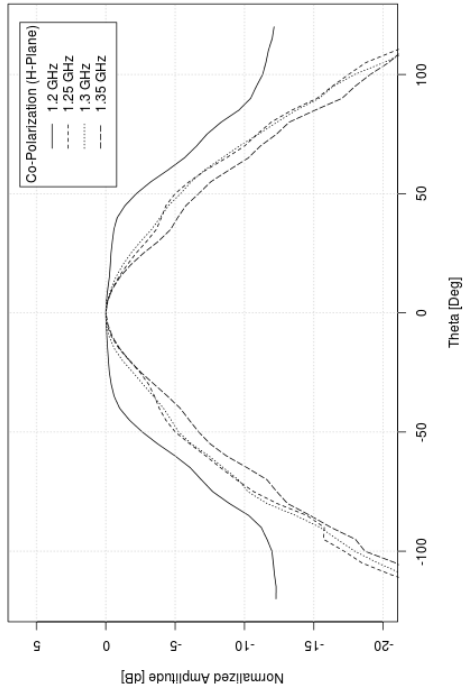


**Figure 9.14: Experimental Farfield Patterns – H-Plane Co-Polarization**

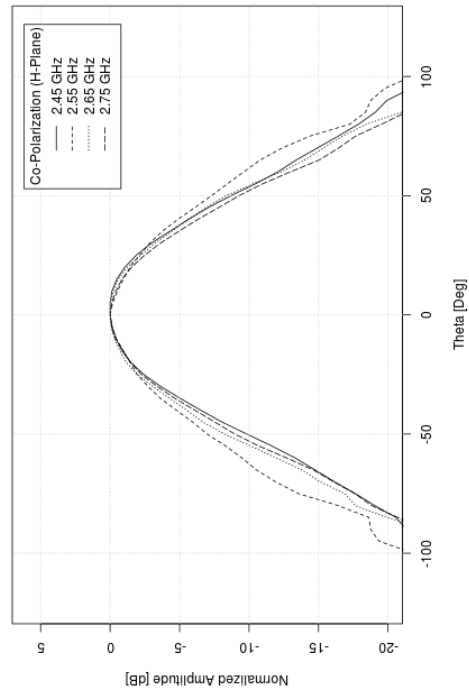
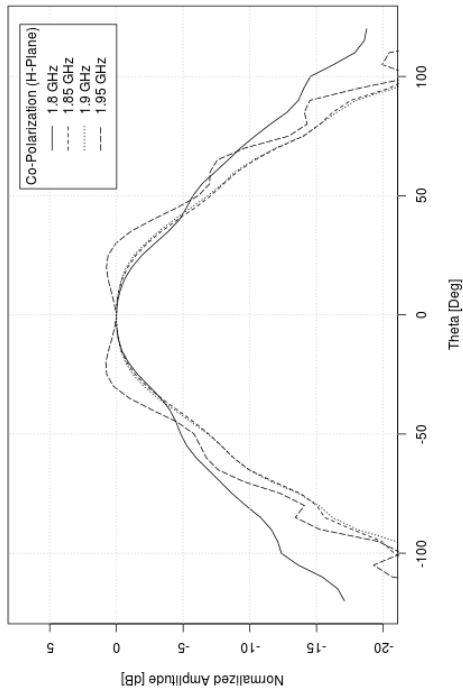
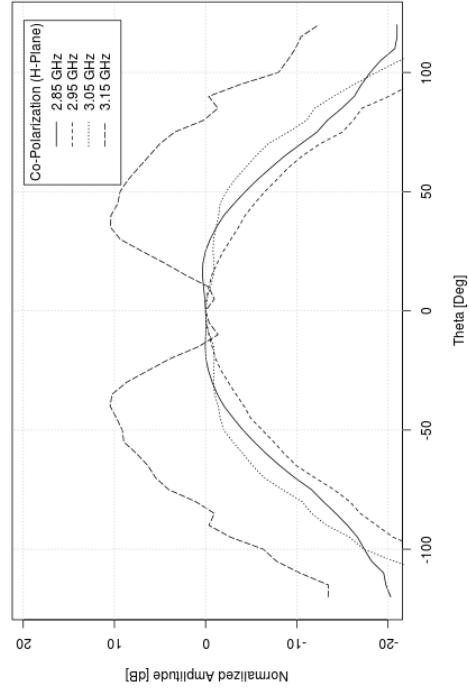
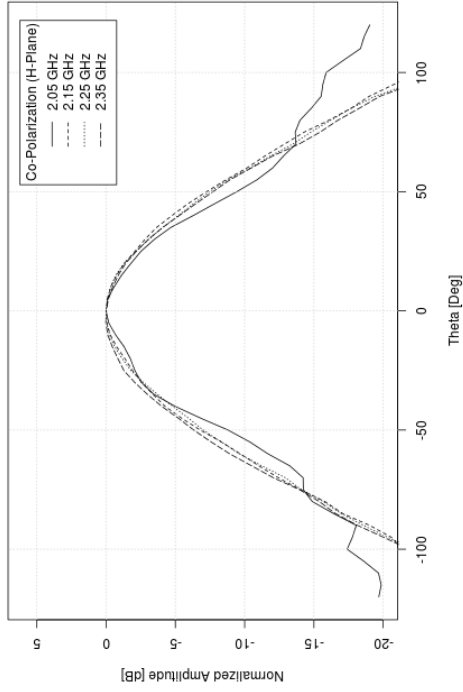


**Figure 9.15: Experimental Farfield Patterns – H-Plane Co-Polarization**

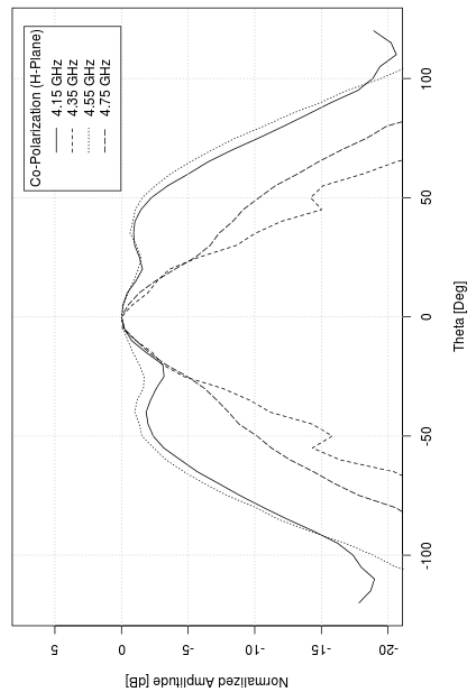
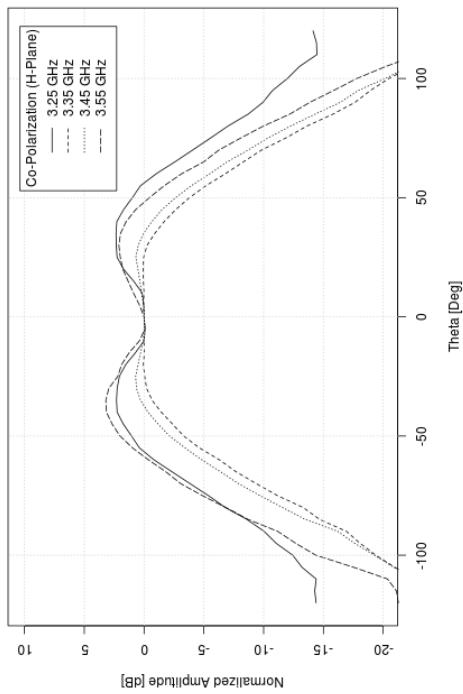
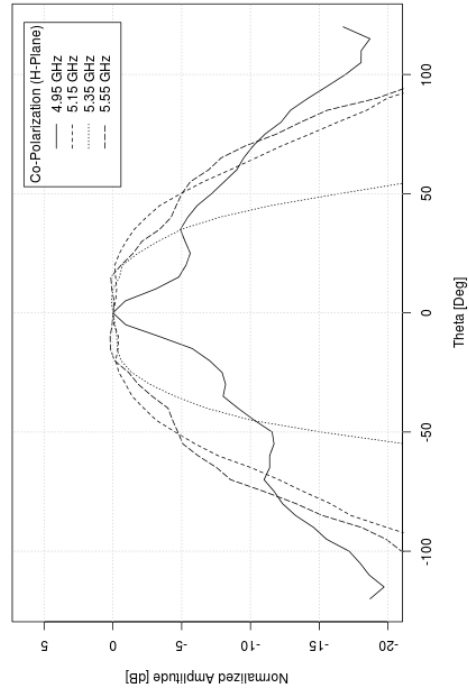
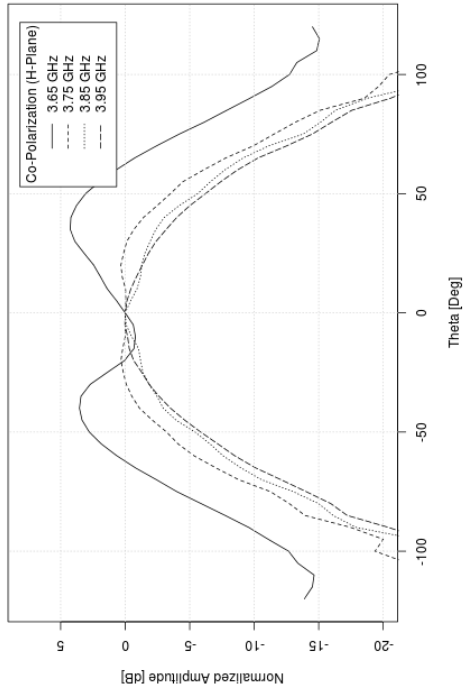


**Figure 9.16: Experimental Farfield Patterns – H-Plane Co-Polarization**

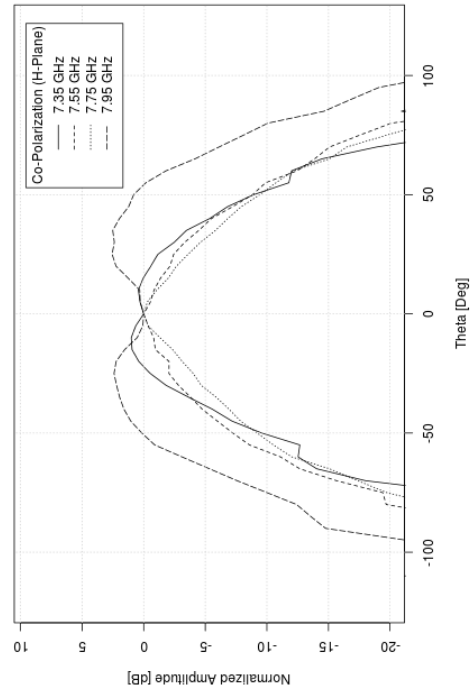
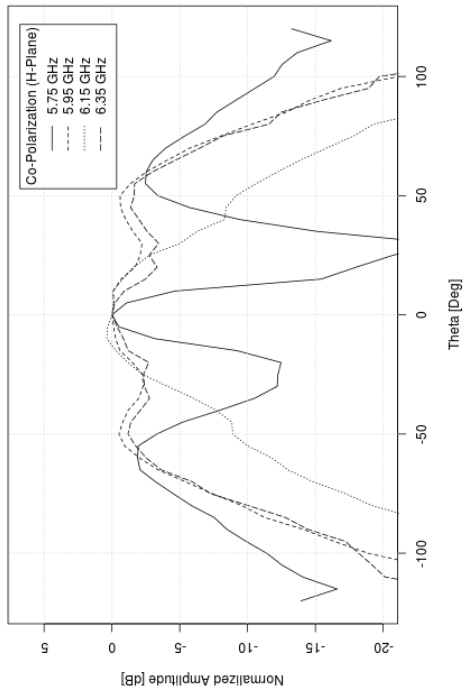
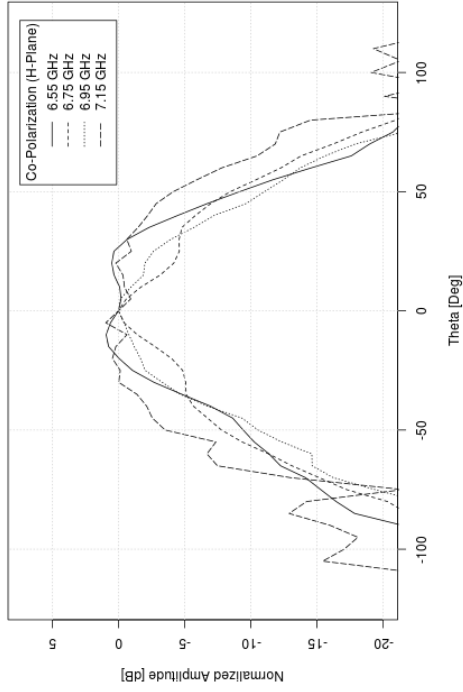


**Figure 9.17: Experimental Farfield Patterns – H-Plane Co-Polarization**

# Chapter 10

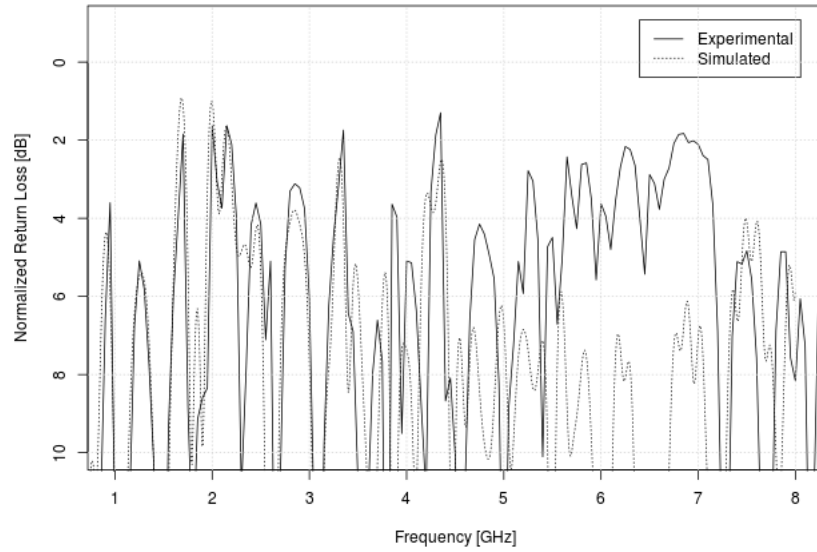
## Discussion

This chapter discusses the simulated and experimental results, the prototyping procedure, and the project as a whole.

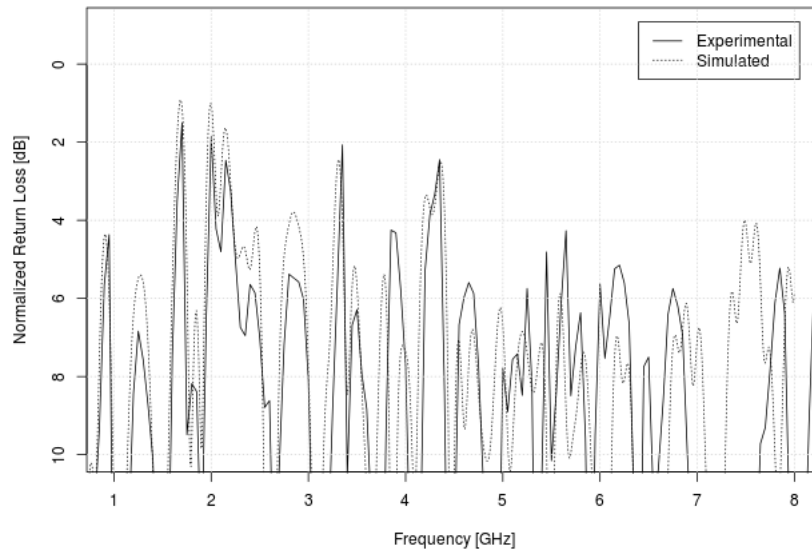
### 10.1 Comparison of Simulated and Experimental Return Loss

One of the purposes of the prototype was to test how accurately CST was able to model this design of antenna. Return loss is easy to compare because it is a two-dimensional data set. Figure 10.1a compares the simulated results to the original experimental results. From 1 GHz to 4.5 GHz there is good agreement between the simulated and experimental return loss. Above 4.5 GHz the agreement is not as good, where there are discrepancies over the amplitude of the return loss. The feed centre modification discussed in section 8.1.2 was made in an attempt to improve the agreement between the experimental and simulated return loss. Figure 10.1b compares the experimental results for the modified prototype to the simulated results. Except for the frequency range from 7 GHz to 7.5 GHz, the return loss with the modified feed centre has generally good agreement between the simulated and experimental results.

Comparing the unmodified prototype results to the results after the feed centre modification, the agreement between the simulated results and the experimental results was slightly worse from 1 GHz to 3 GHz, but significantly improved from



*(a) Return Loss Comparison without Modification*



*(b) Return Loss Comparison with Modification*

**Figure 10.1: Comparison of Return Loss Data**

4.5 GHz to 7 GHz. This behaviour can be explained using the principle of electric size. The feed centre modification involved filling a space in the centre of the excitation structure. At low frequencies, the electric size of this space is small. As a result of this, the space had little effect on the results, meaning that removing the space also had little effect on the results. At mid-frequencies, the electric size of the space was significant, and removing the space improved the performance. Finally, at high frequencies, the small wavelength of the signal means errors in construction or measurement are more significant. Most notably, the centre conductor of the feed line may not have been perfectly centred in the feed gap, which would affect the high frequency results more than the low frequency results.

Another factor that may have contributed to discrepancies between the simulated and experimental results are some of the simplifications made during the simulations. To reduce computation complexity, assumptions were made in CST that the antenna was made of an ideal conductor, and that the background material was a vacuum. Both these assumptions removed damping effects that may have occurred in the prototype. Without this damping, the simulation results may have resonant behaviours that were not reflected in the prototype.

## **10.2 Evaluation of Return Loss**

The return loss from both the simulation and experimental results were inferior to the design goal of 10 dB across the entire operating bandwidth. This is a significant shortcoming in the design. To understand this shortcoming, we consider the return loss in terms of the piece-wise return loss of each component. Figure 10.2 shows the layout of the components that affect the overall return loss. This figure assumes no interaction between the components. From figure 5.18, the return loss for the excitation structure is greater than 10 dB for almost the entire operating bandwidth of the antenna. Figure 5.22 shows that the return loss for each aperture matching structure is between 3 dB and 7 dB across the bandwidth of the matching structure. The return loss of the aperture matching structures is the dominant limiting factor in the overall return loss. Since multiple components are combined in the design, each component must have a return loss greater than 10 dB to achieve the overall return loss goal of 10 dB.

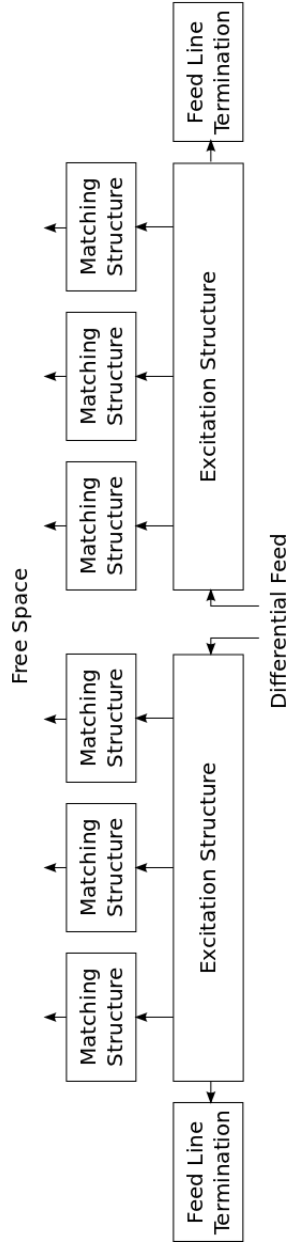


**Figure 10.2: Return Loss Block Diagram**

### 10.3 Simulated Farfield Patterns

The simulated farfield patterns of the electrical design that are shown in section 9.2 can be categorized as generally good with issues at specific frequencies. Figure 10.3 shows an example of a near ideal farfield pattern. This pattern exhibits very good symmetry between the E-plane and H-plane, an edge illumination of -10 dB, and a very small cross-polarization component. Similar patterns were common in the simulated results, especially in the lower frequencies. In these good patterns, the edge illumination of the farfield patterns tended to be somewhat high, often around -7.5 dB. The high edge illumination was a deliberate trade off made during the design procedure in order to increase the bandwidth of each waveguide. The edge illumination issue could be resolved without affecting the bandwidth by either changing the  $f/D$  ratio of the parabolic antenna used or by using a dielectric lens to reshape the farfield.

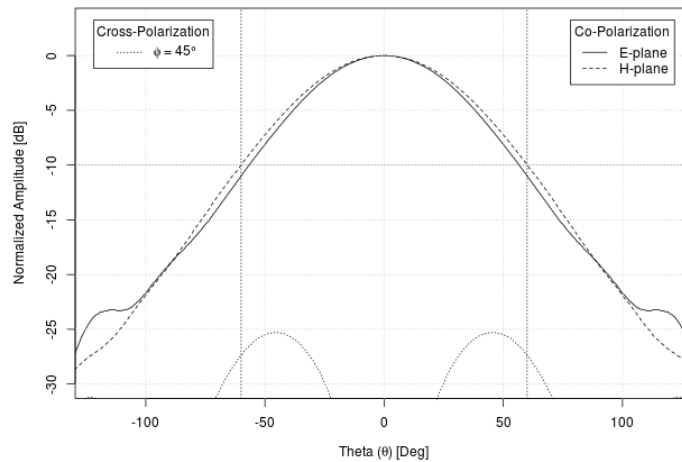


**Figure 10.3:** Near Ideal Farfield Pattern – Design Simulation – 2.05 GHz

The frequency-specific farfield issues manifest themselves as poor farfield patterns over narrow frequency ranges. Some of the frequency ranges may be so narrow that they fall completely between frequency samples in the simulation. The narrowband nature of these issues hints at a possible resonant cause, but investiga-

tion of this theory was not pursued. Most poor farfield patterns were variations on a dual-peak pattern. An extreme example of a dual-peak farfield pattern is shown in figure 10.4. This pattern has a large null at the boresight. This null indicates that parts of the electric field are pointing in opposite directions, such as in the  $TE_{21}$  and  $TE_{31}$  waveguide modes. The  $TE_{21}$  waveguide mode is unlikely since it directly contradicts the excitation structure, meaning that it is likely that the  $TE_{31}$  waveguide mode was present in the waveguide. Additional simulations were run examining the mode amplitudes in the waveguides which showed that the  $TE_{31}$  mode had a higher amplitude at frequencies that exhibited dual-peak farfield patterns than at frequencies that had good farfield patterns.

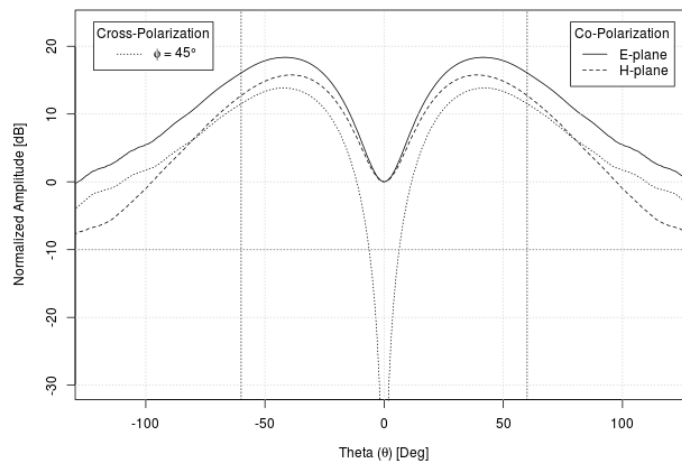


**Figure 10.4:** *Dual-Peak Farfield Pattern – Simulation – 3.15 GHz*

Not all occurrences of the dual-peak patterns were detrimental to the performance of the antenna. Figure 10.5 shows a weak dual-peak farfield pattern. This pattern has a flat amplitude curve near the boresight, and almost no null at the boresight. Because this farfield pattern is closer to the theoretical ideal rectangle pattern, it will collect more energy off the parabolic antenna than the farfield pattern goal set in chapter 4. However, this pattern is the result of both the  $TE_{11}$  and  $TE_{31}$  wave modes operating in the waveguide. It would be very difficult to control the relative amplitudes of the two modes in order to generate good farfield patterns

over the entire frequency range. It is preferable in this case to have only one active waveguide mode.

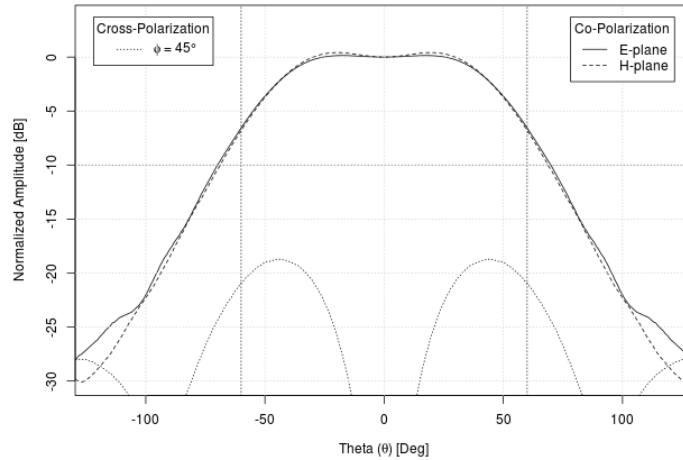


**Figure 10.5:** Weak Dual-Peak Farfield Pattern – Simulation – 3.35 GHz

Additional farfield issues were caused by the  $TE_{11}$  waveguide mode operating in multiple waveguides at the same frequency. Although the waveguides would have the same mode, the electromagnetic fields would be out of phase at the aperture, resulting in unpredictable farfield patterns. This effect is particularly noticeable at the overlap of the frequency bands of the second and third waveguide, with the farfield pattern shown in figure 10.6.

## 10.4 Experimental Farfield Patterns

As expected, the experimental farfield patterns exhibited the same general shape as the simulated results. Figure 10.7 shows an experimental result that is very close to the design goals. The experimental farfield results also exhibited dual-peak farfield patterns as well as patterns with more than two peaks that were not seen in the simulated results. Two examples of multi-peak results are shown in figure 10.8 and figure 10.9. One behaviour unique to the experimental results is frequency dependent asymmetric farfield patterns, as demonstrated in figure 10.10. This be-

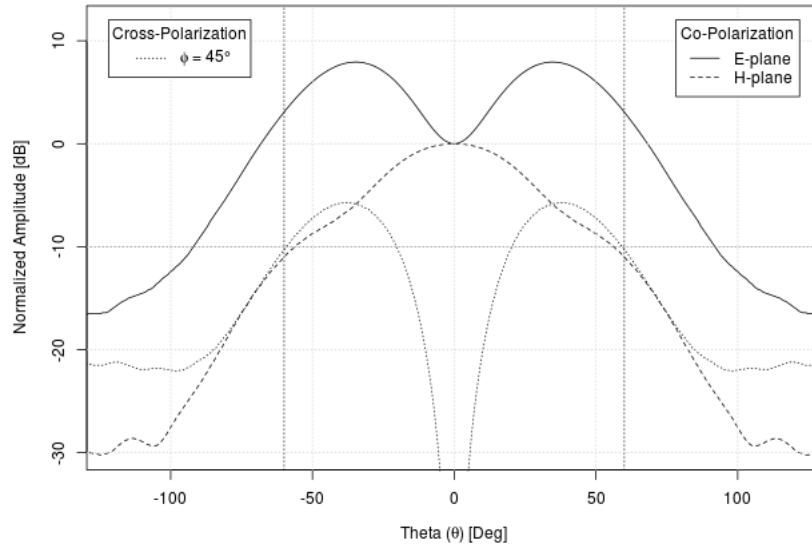


**Figure 10.6:** Farfield at Frequency Band Overlap – Simulation – 4 GHz

haviour was observed over narrow frequency ranges in the mid and high frequency bands of the antenna. Since the antenna is designed to be symmetric, these asymmetric farfield patterns must be caused by construction errors or obstructions in the anechoic chamber. Construction errors would be expected to affect the entire bandwidth, and not produce narrowband issues such as those observed. The anechoic chamber did have a post in it that is used to mount a web camera. This post is covered by radio absorbing material and located in the corner of the chamber behind the prototype positioner. The post would be expected to have an effect on the farfield consistently at high frequencies and not at low frequencies. Neither of these theories are consistent with the observed farfield patterns. These asymmetric patterns require further investigation, beginning with obtaining a second set of experimental farfield results.

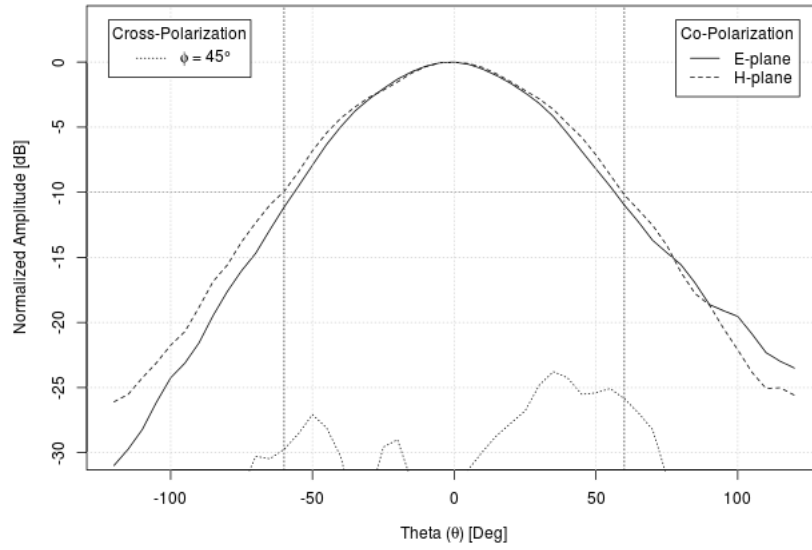


**Figure 10.7:** Near Ideal Farfield Pattern – Experimental – 2.1 GHz

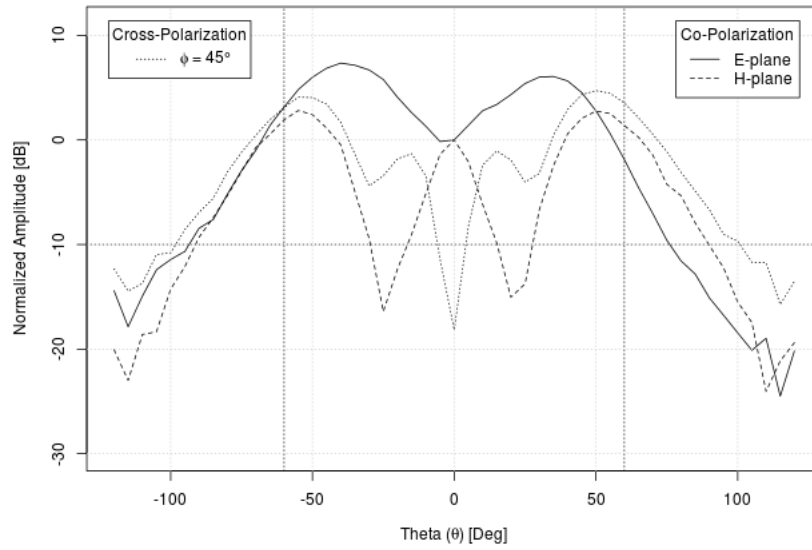


**Figure 10.8:** Dual-Peak Farfield Pattern – Experimental – 6 GHz

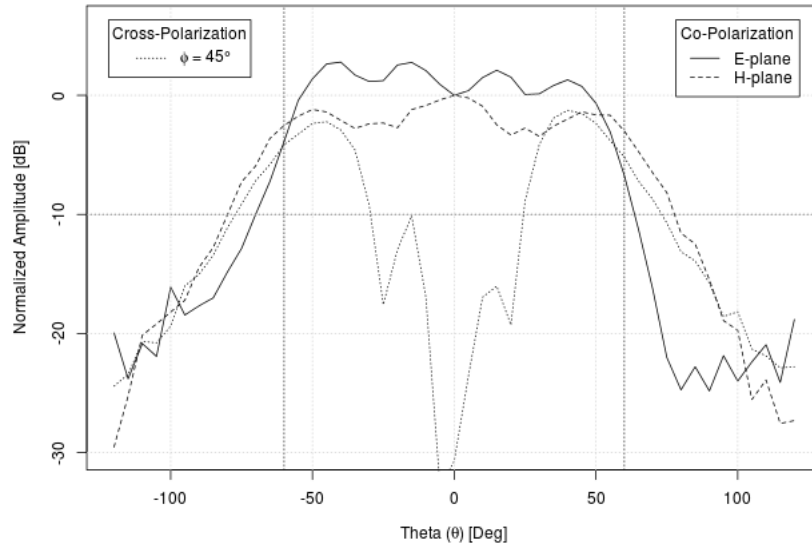


**Figure 10.9:** Multi-Peak Farfield Pattern – Experimental – 6.35 GHz

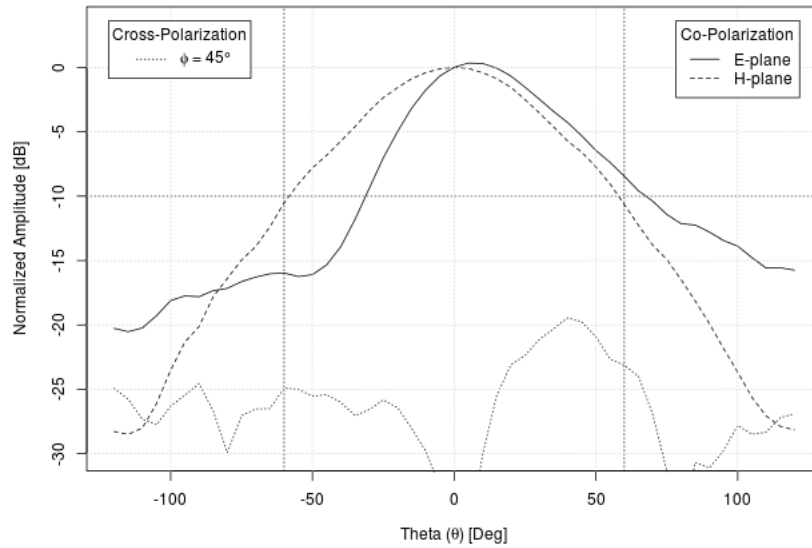


**Figure 10.10:** Asymmetrical Farfield Pattern – Experimental – 2.2 GHz

## **10.5 Comparing Simulated and Experimental Farfield Patterns**

The simulated and experimental farfield results were compared to determine the simulator accuracy for this antenna design. This is a key result of this experiment, because it validates CST as a tool to continue development of this design. The complete set of comparison plots are too numerous to include in this thesis and are kept on file at DRAO. The simulated farfield results are generally in good agreement with the simulated results, especially at low frequencies. An example of good agreement between simulated and experimental results can be seen in figure 10.11. The only common discrepancy between the simulated and experimental results is the cross-polarization component around the boresight. This is expected since the the simulator has  $-\infty$  dB cross-polarization component at the boresight which is not achievable in practice. The simulator was also able to accurately predict the frequencies at which a dual-peak pattern would occur, although the relative amplitudes of the dual-peaks were often incorrect with an error as large as  $\pm 5$  dB. A comparison of a dual-peak pattern is shown in figure 10.12. It is important to have good agreement for dual-peak patterns, as this behaviour is undesired and needs to be minimized. A grid sensitivity analysis could be conducted in CST with a specific goal of improving the agreement of the amplitude of dual-peaks. There were narrow frequency ranges that had poor agreement between simulated and experimented results. One example of this was at 4.35 GHz shown in figure 10.13. The only discrepancy that occurred over an extended frequency range was from 5.45 GHz to 5.6 GHz. There was poor farfield pattern agreement throughout this frequency range as illustrated by figure 10.14. These discrepancies should be investigated to see if the simulation model or the construction method can be changed to improve agreement.

## **10.6 Correlation Between Return Loss and the Quality of the Farfield Patterns**

The relationship between the return loss of the antenna and the quality of the farfield patterns as a function of frequency was investigated. For this analysis the experimental results were used. The frequencies that had the worst farfield patterns

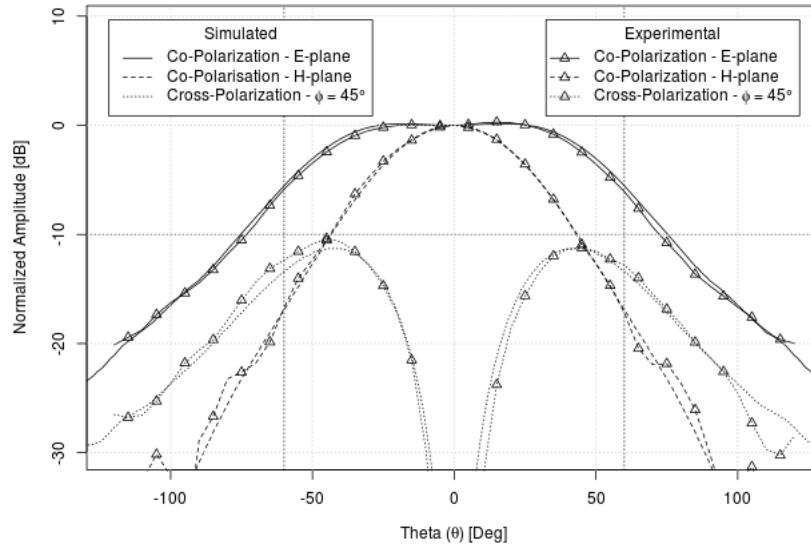


**Figure 10.11:** Good Agreement in Farfield Results – 2.8 GHz

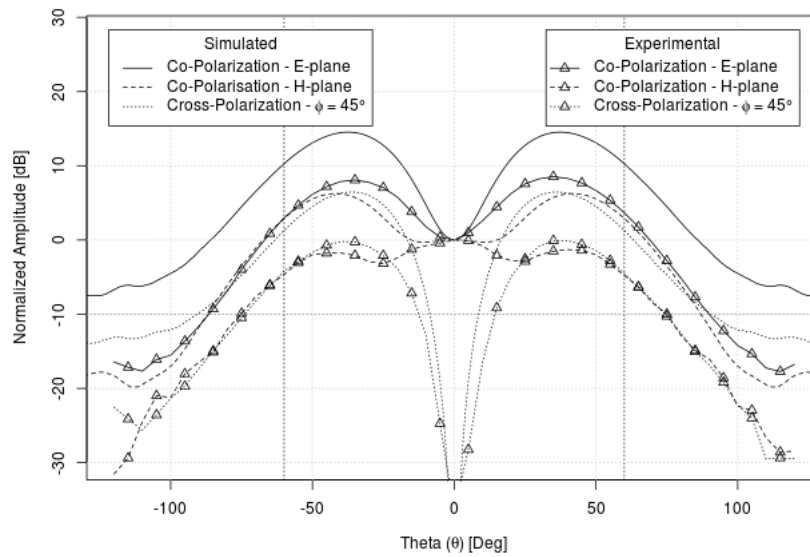


**Figure 10.12:** Different Amplitude of Dual-Peak – 4.05 GHz

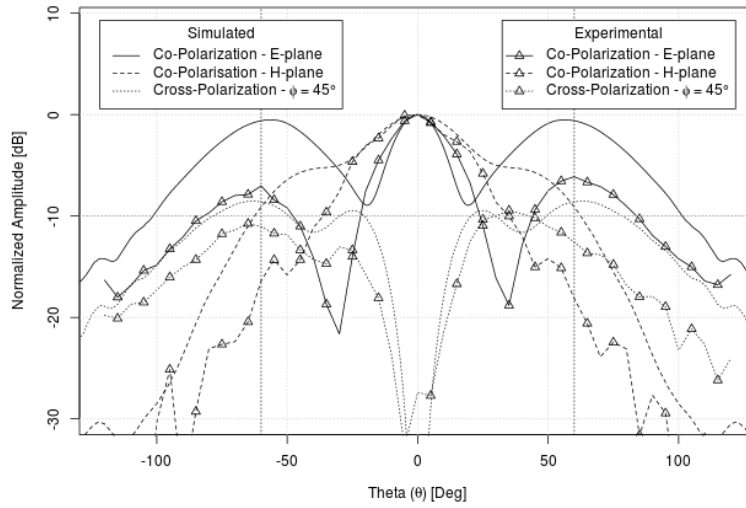


**Figure 10.13:** Poor Agreement in Farfield Results – 4.35 GHz

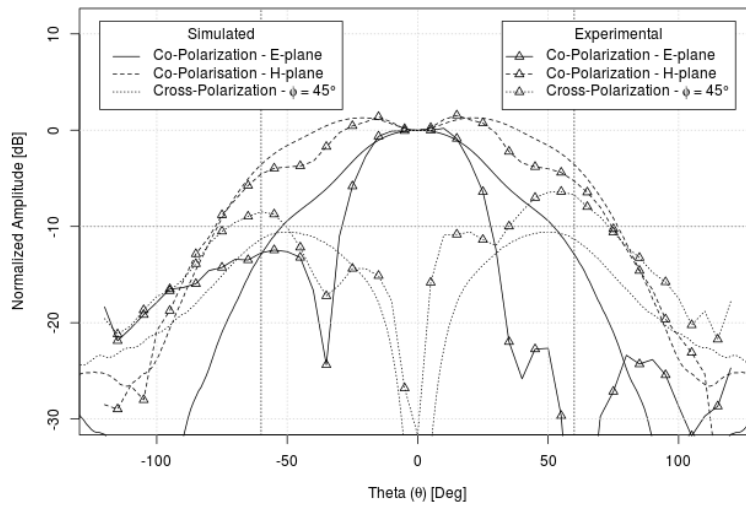


**Figure 10.14:** Sample from Extended Frequency Range of Poor Agreement in Farfield Results – 5.5 GHz

were noted and the return loss was found for those frequencies. It was discovered that the frequencies that had very poor farfield patterns also had very high return losses, in excess of 10 dB. The converse was also found to be true, that the frequencies that had good farfield patterns generally had a return loss between 2 dB and 6 dB. This correlation makes sense when the reasons for poor farfield patterns are considered. The two major causes of poor farfield patterns are multiple modes propagating and multiple waveguides radiating at the same frequency. Both these situations allow more energy to be coupled from the excitation structure to free space and as a result the return loss is increased at those frequencies. This makes the return loss a somewhat misleading metric and it should be noted in further testing that the return loss is only an accurate measure of performance at frequencies with good farfield patterns.

## **10.7 Effects of Poor Return Loss at the Aperture**

Each individual section of the antenna was designed assuming all other sections functioned perfectly. Since this assumption was false, there could be interactions between the sections. Most notably, the poor return loss at the aperture likely had negative effect on the performance of the other sections of the antenna. One hypothesis is that the poor return loss at the aperture was translated back to the excitation structure, leading to excitation performance inferior to that predicted by the piece-wise simulations. This would cause the signal to travel further down the feed line than it would otherwise and radiate into the wrong waveguides. These outer waveguides have lower cutoff frequencies, which would result in increased over-moding and worse farfield patterns. This hypothesis was not confirmed during this project.

## **10.8 Issues with Prototype Construction**

The construction of the prototype generally went well. Except for the excitation elements, which were redesigned late in the design process, all the components of the antenna could be fabricated as designed.

A few issues were found during the assembly procedure. It was difficult to position the centre conductor of the feed line correctly in the feed gap while the

feed line was being soldered. This can be solved by creating improved spacers, possibly using a water-jet cutting machine.

During the assembly of the back section, it was found that the semi-rigid SMA cables were blocking some of the screw holes used to secure the the front cylinders in place. This is shown in figure 10.15. Additionally, since these cables extended well out from the centre of the waveguide, they could easily torque the connections inside the antenna. Both these problems could be resolved by replacing the semi-rigid SMA cable in the design with flexible SMA cable. However, flexible SMA cable is harder to modify. This would make the connections to the feed lines inside the antenna more difficult.

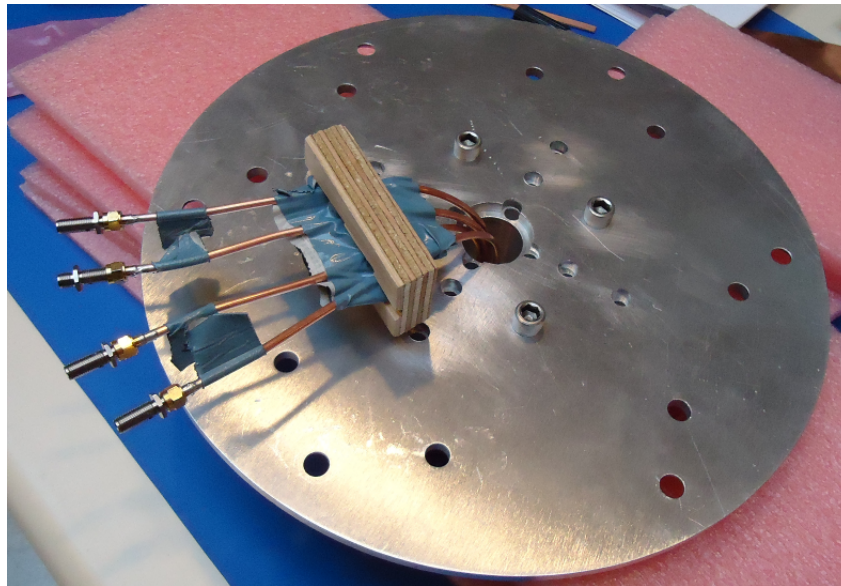


*Figure 10.15: Semi-rigid SMA Cable Protruding from Back Section*

For final assembly, it was found that positioning the front cylinder correctly while inserting the first and second screws was often difficult. This could be remedied by using pins for positioning. This option was considered during the design phase but never implemented. Once all the screws were in place they functioned well as fasteners and the prototype felt very solid.

The most significant issue with the physical design was the construction of the feed centre assembly. The brass plug was very difficult to solder and the conduc-

tive epoxy was not strong enough to prevent the SMA cables from moving. No modification to the current design has been conceived and it would be advisable to completely redesign this component.

## **10.9 General Feasibility of the Design**

The general feasibility of this design will be determined by how well the design meets the design goals, the ability to physically realize the design, the performance of the design, and the prospects of correcting any shortcoming in the design. This design meets the goal of taking one differential source and feeding multiple nested waveguides using a common excitation structure. The design goal of generating good farfield patterns across a wide bandwidth was also achieved with a bandwidth ratio of 8:1. The goal of having all the antenna components scale with frequency was not fully met because the angle of the excitation elements was different for each waveguide. This increases the complexity of designing the excitation structure for further iterations of the antenna design. The height of the feed line and excitation elements also did not scale with frequency, but it is believed that this will have little effect on future iterations of the design. Since a prototype was successfully built and tested, the current design has been proven to be physically realizable.

The return loss performance for this design was poor. This issue has been traced back to the poor performance of aperture matching structures. There were some poor farfield patterns, but these were all frequency-specific issues and the majority of the operating range had good farfield patterns. It is hypothesized that the poor farfields patterns will be improved by addressing the return loss issue. As such, the overall feasibility of this design hinges on the ability to significantly improve the return loss at the aperture. If a solution to this problem can be found, this antenna design could be fully feasible.

# Chapter 11

## Further Work

It was known from the conception of this project that it would require many years of work to produce a fully realized design. Since the primary researcher for this project was a student working towards a Master's degree, the work was scaled down to fit a reasonable time-line for the student. Throughout the course of the project many possible design options were not explored due to time constraints, and some issues were not resolved.

### 11.1 Improved Aperture Matching Structure

As discussed in section 10.2, the return loss at the aperture was a limitation of the design. This should be the first problem tackled when iterating on the design. The most promising avenue of research to solve this problem is to use extended centre conductors at the aperture in order to improve the return loss. An attempt could be made to modify the antenna design to work with an aperture structure similar to the one given in [26]. This aperture structure has been shown to have good return loss and reasonable farfield patterns.

A number of other possible solutions to the aperture return loss issue were conceived but not tested. One possible solution considered is to place dielectric material either in front of the antenna or inside the waveguides to try to improve the impedance match between the waveguides and free space. Conventional dielectric materials or meta-materials with a negative dielectric constant could be considered

for this purpose. Irises installed inside the waveguide have also been shown to improve matching with free space [11], but these matches are narrowband, and the challenge would be to design a system of irises to create a wideband match. A final possible solution would be to increase the waveguide ratio to improve the match between the waveguides and free space, but this would require altering all the other components in the antenna design to work over a significantly wider bandwidth.

## **11.2 Feed Centre Redesign**

As discussed in section 10.8, the feed centre assembly was very hard to construct, and should be redesigned. This component is not tied to the electrical design and can be redesigned without considering the effects on the farfield patterns. However, as noted in section 8.1.2, a poorly designed feed centre can affect the return loss. This needs to be considered during the redesign of the component. The feed centre component must physically secure the incoming coaxial cables to the antenna, ground the shield of the coaxial cables to the body of the antenna, and facilitate the connections between the feed lines and the centre conductor of the coaxial cables. An alternative design could use PCBs to accomplish these tasks.

## **11.3 Balun**

A balun is a device that converts an unbalanced line to two balanced lines and vice versa. The antenna design created in this project requires two sets of differential signals. Baluns that have the same bandwidth as the antenna need to be either designed or sourced.

## **11.4 Excitation Optimization and Redesign**

The excitation structure presented in this thesis has performance that almost meets the design goals. Because the excitation structure was modified after fabrication had begun, it was not fully optimized. Specifically, the lengths from the excitation elements to the shorting back plate and the feed line impedance were already fixed when the excitation structure was redesigned. It is likely that if the structure is re-optimized with these parameters available to the optimizer, the performance of

the excitation structure could be improved.

It would be worth while to see if the excitation structure could be redesigned to be made out of PCB. The structure already has a thickness of  $1/8''$  so this is not unreasonable. If the excitation structure could be made out of PCB, it would make the tasks of securing the excitation structure and attaching the coaxial cables and feed line terminations significantly simpler.

The excitation structure in this design does not meet the periodic design principle, as the excitation elements do not scale from one waveguide to the next. This was done for two reasons, the thickness is constant so that the excitation structure can be cut out of a single piece of sheet metal, and the angle changes from waveguide to waveguide to reduce over-moding in the outer waveguides. If the over-moding issue can be addressed in some other way, the excitation structure should be redesigned to be periodic in shape with constant thickness. It is theorized, although not tested, that at low frequencies the thickness of the feed line already has a small enough electric size that it can be considered arbitrarily thin. If this is true, reducing the electric size further would not affect performance, and additional waveguides could be added to the antenna with very limited alterations to the excitation structure beyond extending it by the replication ratio.

## **11.5 Mode and Frequency Filtering**

One possible way to address the dual peak farfield pattern issues is to add additional mode and frequency filtering to the waveguides. Currently the tasks of frequency filtering and mode control are attempted by the excitation structure with limited success.

## **11.6 Dielectric Lenses**

As discussed in section 10.3, the farfield pattern for most frequencies was wider than the design goal. One possible remedy to this problem is to use a dielectric lens to reduce the beamwidth. Dielectric lenses are discussed in [23, pp. 370]. This concept could also be used with the parallel rectangular waveguide concept, since that design was found to have farfield patterns that were too narrow. The problem with using dielectric lenses is that they introduce additional losses into

the system.

### **11.7 Choke Study**

Due to time constraint, the choke was only partially optimized. An extended optimization of the choke may find a more optimal, and possibly smaller, choke design.

### **11.8 Aperture Alignment Section Length Study**

The effect of the aperture alignment sections that were discussed in section 5.9 on the performance of the antenna is not fully understood. It was determined through simulation that extending the lengths of the aperture alignment sections improved the overall return loss. The aperture alignment sections should be studied more thoroughly to determine how the space affects the return loss and if there are optimal lengths that are reasonable to construct.

### **11.9 Phase Study**

The phase centre of the antenna as a function of frequency needs to be determined. CST provided phase data for the simulated antenna, but time restrictions prevented this data from being analyzed. Ideally, the phase centre of a feed antenna should be as stationary as possible and located at the focal point of the parabolic antenna to achieve optimal efficiency.

### **11.10 Cryogenic Study**

In radio astronomy, it is critical to reduce all sources of noise. To facilitate this, feed antennas are often operated while cryogenically cooled to minimize thermal noise. The physical model needs to be tested to see if the cooling process creates any issues. This can be done using simulator tools, such as SolidWorks, or by modifying and testing the prototype.

### **11.11 Full Model Optimization**

During the design of this antenna, only piece-wise optimizations of the sections were conducted, ignoring the interactions between the sections. To improve performance, the antenna as a whole should be optimized with all the major physical dimensions as optimization parameters. It is expected that a full model optimization would require many months to complete.

### **11.12 Improved Fabrication Techniques**

The fabrication of the major components proved to be very wasteful of raw materials. For this prototype, each component was cut out of a separate block of aluminium. This is extremely wasteful as the majority of the raw metal was turned into shavings. In a production design, material waste could be vastly improved by using a casting for the rough shape of the components and then finishing with a lathe or milling machine.

### **11.13 Alternative Designs**

A number of design alternatives were not explored in the design procedure. For example, parallel rectangular waveguides could be used instead of nested coaxial waveguides. This design was not chosen because it was found in simulation that the parallel rectangular waveguide antenna produced farfield patterns that were too narrow for the specified application. This design may become feasible if a method was found to widen the farfield pattern. Another design that deserves some analysis is a nested waveguide structure with the excitation elements located at the aperture. This design was proposed in the initial concept work for this project but never fully explored.

## Chapter 12

# Conclusion

This project succeeded in taking a concept for a log-periodic waveguide antenna, modelling the design, and then manufacturing and testing a prototype. The final electrical design was composed of four sections: the excitation section, the aperture section, the aperture matching sections, and the aperture alignment section. The antenna was designed to produce good farfield patterns, have high return loss, and be easy to construct.

The construction of the prototype went well, with a few areas that could be improved upon in further iterations of the design. Most notably, the feed centre structure requires a complete redesign. The prototype was tested and the simulated results were compared to the experimental results. It was found that the simulated results were in good agreement with the experimental results for the majority of the prototype's bandwidth, and the disagreements tended to be over narrow frequency ranges.

The return loss of the design was found to be poor, ranging from 2 dB - 6 dB compared to the return loss goal of 10 dB. This was most likely caused by the poor performance of the aperture matching structures. The farfield patterns of the design were good, although slightly wide. There were frequency-dependent issues with the farfield, relating to either over-moding or multiple waveguides radiating at the same time.

This design shows significant potential. A number of problems were successfully addressed in this design. If the aperture return loss issue can be solved, this

design may become feasible for practical use. This design merits further work, as do other design concepts that were not fully considered during the design process.

# Bibliography

- [1] *CST Microwave Studio, Workflow and Solver Overview*. CST - Computer Simulation Technology AG, 2001.
- [2] The Swift Gamma-Ray Burst Mission, Dec. 2011. URL [heasarc.nasa.gov/docs/swift/swiftsc.html](http://heasarc.nasa.gov/docs/swift/swiftsc.html).
- [3] Introduction to Infrared Astronomical Satellite (IRAS), Mar. 2011. URL [irsa.ipac.caltech.edu/IRASdocs/iras.html](http://irsa.ipac.caltech.edu/IRASdocs/iras.html).
- [4] C. A. Balanis. *Modern Antenna Handbook*. John Wiley and Sons, Inc., 2008.
- [5] T. Bird. TE<sub>11</sub> Mode Excitation of Flanged Circular Coaxial Waveguides with an Extended Center Conductor. *Antennas and Propagation, IEEE Transactions on*, 35(12):1358 – 1366, Dec. 1987. ISSN 0018-926X. doi:10.1109/TAP.1987.1144026.
- [6] T. Bird, G. James, and S. Skinner. Input Mismatch of TE<sub>11</sub> Mode Coaxial Waveguide Feeds. *Antennas and Propagation, IEEE Transactions on*, 34(8): 1030 – 1033, Aug. 1986. ISSN 0018-926X. doi:10.1109/TAP.1986.1143943.
- [7] R. N. Bracewell. *The Fourier Transform and Its Applications*. McGraw-Hill, 2000.
- [8] J. Z. Buchwald. *The Creation of Scientific Effects: Heinrich Hertz and Electric Waves*. University of Chicago Press, 1994.
- [9] M. A. R. Gunston. *Microwave Transmission-Line Impedance Data*. Van Nostrand Reinhold Company Ltd., 1972.
- [10] K. Hornik. The R FAQ, 2011. URL <http://CRAN.R-project.org/doc/FAQ/R-FAQ.html>. ISBN 3-900051-08-9.

- [11] G. James. Admittance of Irises in Coaxial and Circular Waveguides for  $TE_{11}$  Mode Excitation. *Microwave Theory and Techniques, IEEE Transactions on*, 35(4):430 – 434, Apr. 1987. ISSN 0018-9480. doi:10.1109/TMTT.1987.1133666.
- [12] S. Johns and J. Prata, A. An Ultra-Wideband Nested Coaxial Waveguide Feed for Reflector Antenna Applications. In *Antennas and Propagation Society International Symposium, 1999. IEEE*, volume 1, pages 704 –707 vol.1, Aug. 1999. doi:10.1109/APS.1999.789235.
- [13] A. Kishk, L. Shafai, and A. Ittipiboon. Improvement in Radiation Characteristics of Coaxial Feeds Using a Quarter-Wavelength Choke. *Electronics Letters*, 20(12):522 –523, July 1984. ISSN 0013-5194. doi:10.1049/el:19840362.
- [14] J. D. Kraus. *Radio Astronomy*. Cygnus-Quasar Books, 2nd edition, 1986.
- [15] J. D. Kraus and R. J. Marhefka. *Antennas: For all Applications*. McGraw-Hill, 2002.
- [16] L. Kraus and C. Profera. A Technique for Obtaining Pattern Symmetry and Low Sidelobes from a  $TE_{11}$  Mode Coaxial Radiator. *Antennas and Propagation, IEEE Transactions on*, 25(3):365 – 369, May 1977. ISSN 0018-926X. doi:10.1109/TAP.1977.1141607.
- [17] A. Ludwig. The Definition of Cross Polarization. *Antennas and Propagation, IEEE Transactions on*, 21:116 – 119, 1973.
- [18] N. Marcuvitz. *Waveguide Handbook*, volume 21 of *IEEE Electromagnetic Wave Series*. Peter Peregrinus Ltd., 1986.
- [19] J. C. Maxwell. A Dynamical Theory of the Electromagnetic Field. *Philosophical Transactions of the Royal Society of London*, 155:459–51, 1865.
- [20] E. McMilin, D. Henke, S. Claude, and J. Bornemann. A Low-Cost Directional Log Periodic Log Spiral Antenna. In *Antennas and Propagation Society International Symposium (APSURSI), 2010 IEEE*, pages 1 –4, July 2010. doi:10.1109/APS.2010.5561006.
- [21] P. J. Nahin. *Oliver Heaviside: the Life, Work, and Times of an Electrical Genius of the Victorian Age*. JHU Press, 2002.

- [22] R. Olsson, P.-S. Kildal, and S. Weinreb. The Eleven Antenna: a Compact Low-Profile Decade Bandwidth Dual Polarized Feed for Reflector Antennas. *Antennas and Propagation, IEEE Transactions on*, 54(2):368 – 375, February 2006. ISSN 0018-926X. doi:10.1109/TAP.2005.863392.
- [23] A. Olver. *Microwave Horns and Feeds*. Iee Electromagnetic Waves Series. IEEE, 1994. ISBN 9780852968093. URL <http://books.google.ca/books?id=ZZw7MHFuqF8C>.
- [24] D. M. Pozar. *Microwave Engineering*. John Wiley and Sons, Inc., 3rd edition, 2005.
- [25] G. L. Ragan. *Microwave Transmission Circuits*. McGraw-Hill Book Company, Inc., 1948.
- [26] W. Ruzheng, Q. Jinghui, and S. Zhaohui. Analysis and design of an ultra-wideband nested coaxial waveguide feed. In *Antennas, Propagation and EM Theory, 2003. Proceedings. 2003 6th International Symposium on*, pages 168 –171, Nov. 2003. doi:10.1109/ISAPE.2003.1276655.
- [27] D. Savini, G. Figlia, A. Ardenne, and K. van't Klooster. A Triple Frequency Feed for the QUASAT Antenna. In *Antennas and Propagation Society International Symposium, 1988. AP-S. Digest*, pages 342 –345 vol.1, Jun. 1988. doi:10.1109/APS.1988.94066.
- [28] J. Thal, H.L. and J. Manges. Theory and Practice for a Spherical-Scan Near-Field Antenna Range. *Antennas and Propagation, IEEE Transactions on*, 36(6):815 –821, June 1988. ISSN 0018-926X. doi:10.1109/8.1183.
- [29] T. Weiland. Rf microwave simulators – from component to system design. In *Microwave Conference, 2003. 33rd European*, pages 591 –596, Oct. 2003. doi:10.1109/EUMA.2003.341022.
- [30] R. Wohlleben, H. Mattes, and O. Lochner. Simple Small Primary Feed for Large Opening Angles and High Aperture Efficiency. *Electronics Letters*, 8 (19):474 –476, 1972. ISSN 0013-5194. doi:10.1049/el:19720341.
- [31] A. Yaghjian. An Overview of Near-Field Antenna Measurements. *Antennas and Propagation, IEEE Transactions on*, 34(1):30–45, Jan. 1986. ISSN 0018-926X. doi:10.1109/TAP.1986.1143727.
- [32] J. Yang. On Conditions for Constant Radiation Characteristics for Log-Periodic Array Antennas. *Antennas and Propagation, IEEE*

*Transactions on*, 58(5):1521 –1526, May 2010. ISSN 0018-926X.  
doi:10.1109/TAP.2010.2044332.

- [33] J. Yang, X. Chen, N. Wadefalk, and P.-S. Kildal. Design and Realization of a Linearly Polarized Eleven Feed for 1-10 GHz. *Antennas and Wireless Propagation Letters, IEEE*, 8:64 –68, 2009. ISSN 1536-1225.  
doi:10.1109/LAWP.2008.2011148.
- [34] J. Yang, M. Pantaleev, P.-S. Kildal, B. Klein, Y. Karandikar, L. Helldner, N. Wadefalk, and C. Beaudoin. Cryogenic 2-13 GHz Eleven Feed for Reflector Antennas in Future Wideband Radio Telescopes. *Antennas and Propagation, IEEE Transactions on*, 59(6):1918 –1934, June 2011. ISSN 0018-926X. doi:10.1109/TAP.2011.2122229.

# Appendices

## **Appendix A: DRAO Concept Document**

**Document Author:** Dr. Tom Landecker

**Document Date:** 8 February 2010

## Some Thoughts on Waveguide-Based Log-periodic Feed

Tom Landecker

8<sup>th</sup> February 2010

Feeds based on waveguides have very low losses. Is it possible to design a log-periodic feed based on waveguides?

Coaxial waveguides can provide very good illumination of paraboloidal reflectors. Various designs exist that achieve good performance in two bands by nesting a circular waveguide feed inside a coaxial waveguide feed, or performance in three bands by nesting coaxial waveguides inside one another. It should be possible to obtain wideband performance with an assembly of concentric coaxial waveguides whose diameters are chosen in a log-periodic fashion, as illustrated in Figure 1.

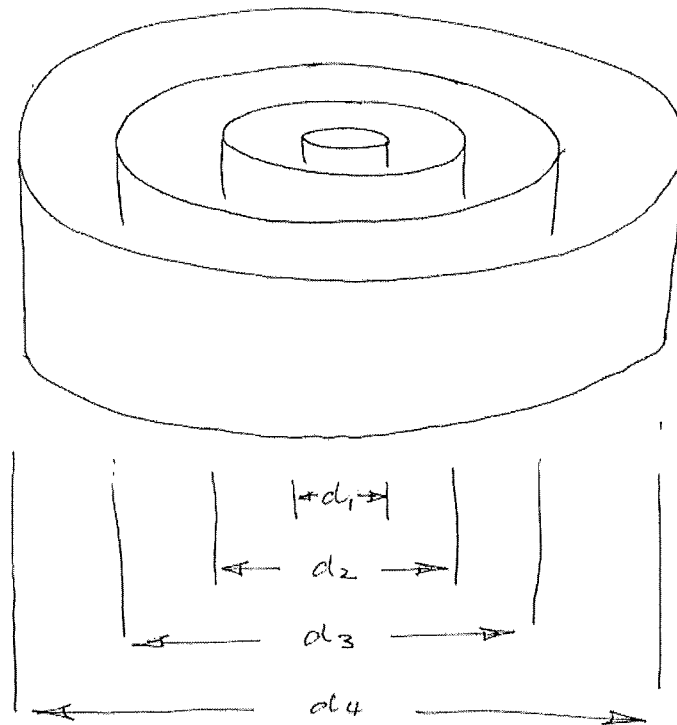


Figure 1: A log-periodic assembly of coaxial waveguides.  
 $d_1/d_2 = d_2/d_3 = d_3/d_4$  etc.

An individual coaxial waveguide feed can have a fractional bandwidth of 20% to 30% without significant change in radiation properties, so this would determine the scaling factor.

The phase centres of these feeds will be in or near the waveguide apertures. The front face should either be flat or slightly sloped, as illustrated in Figures 2 and 3.

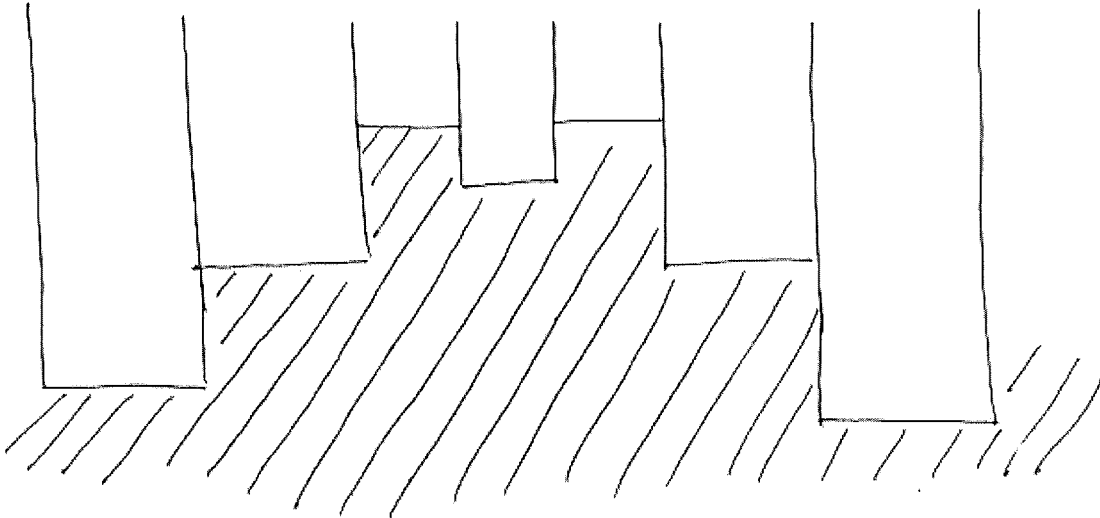


Figure 2: Cross section with flat front surface

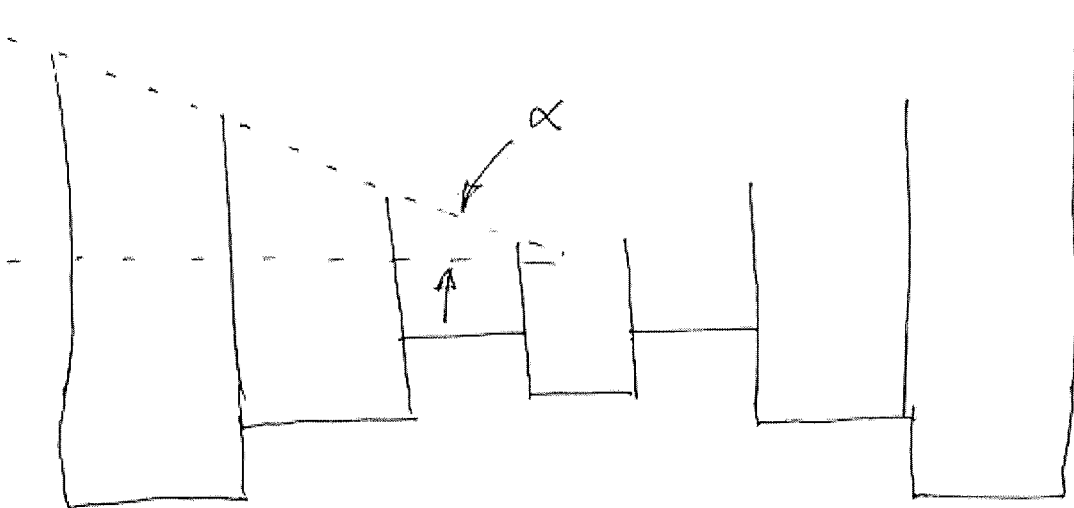


Figure 3: Cross section with sloped front surface. The optimum value of angle  $\alpha$  would have to be determined.

One possible complication arises from coupling between the waveguides. The high-frequency signal radiated by the innermost coaxial waveguide would couple into the next ring outwards, and so on. It may be necessary to use choke sections to eliminate this coupling, as suggested in Figure 4.

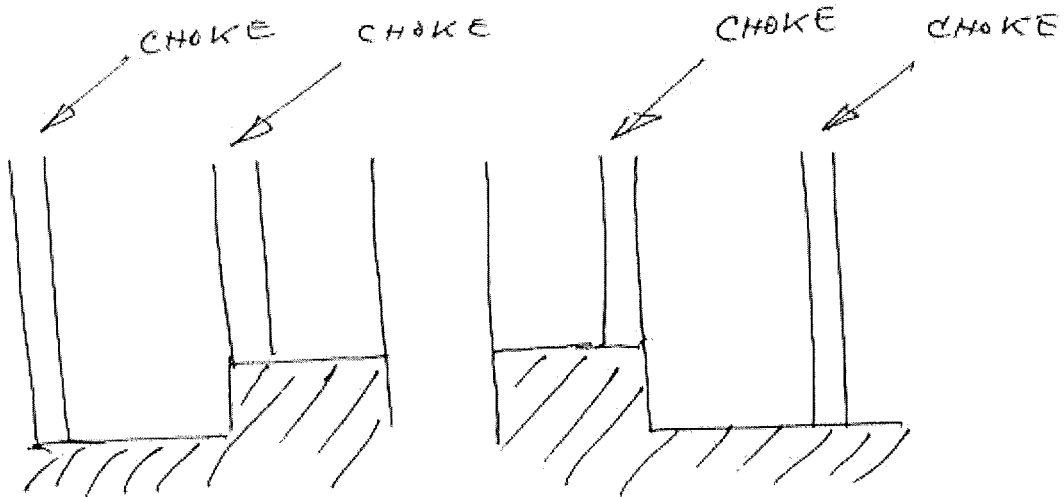


Figure 4: Feed with choke sections to eliminate or control coupling between waveguides.

Exciting the coaxial waveguide feeds is a remaining problem. Each coaxial waveguide could be excited by probes that would launch two orthogonal  $TE_{11}$  modes in each waveguide, but we want to connect all the probes to one transmission line. One idea is illustrated in Figure 5, but it is likely to be very hard to make this work.

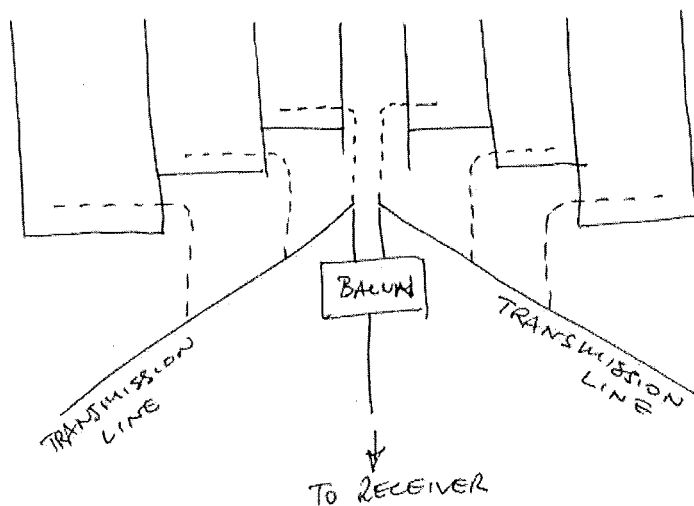


Figure 5: One possible means of exciting the waveguides.

An alternative is to put the exciting probes outside the front face of the waveguides, as illustrated in Figure 6 (this was suggested in Bruce's earlier scheme). However, this may generate unwanted modes in the waveguides and may also cause unwanted coupling.

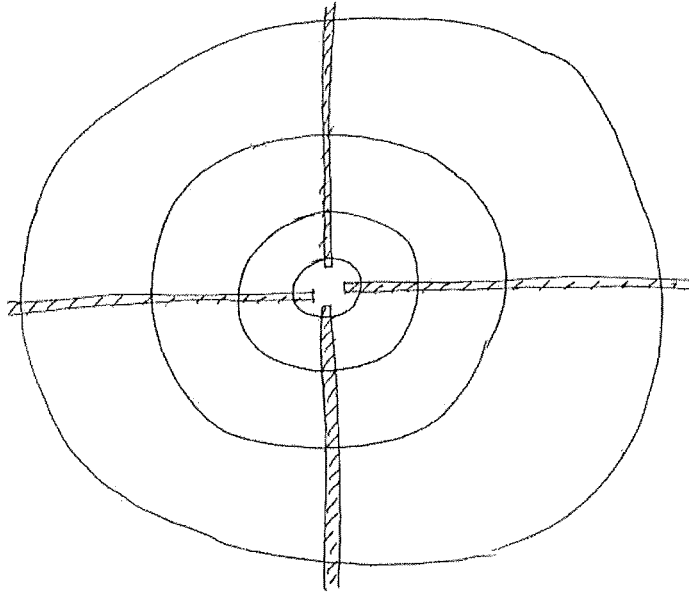
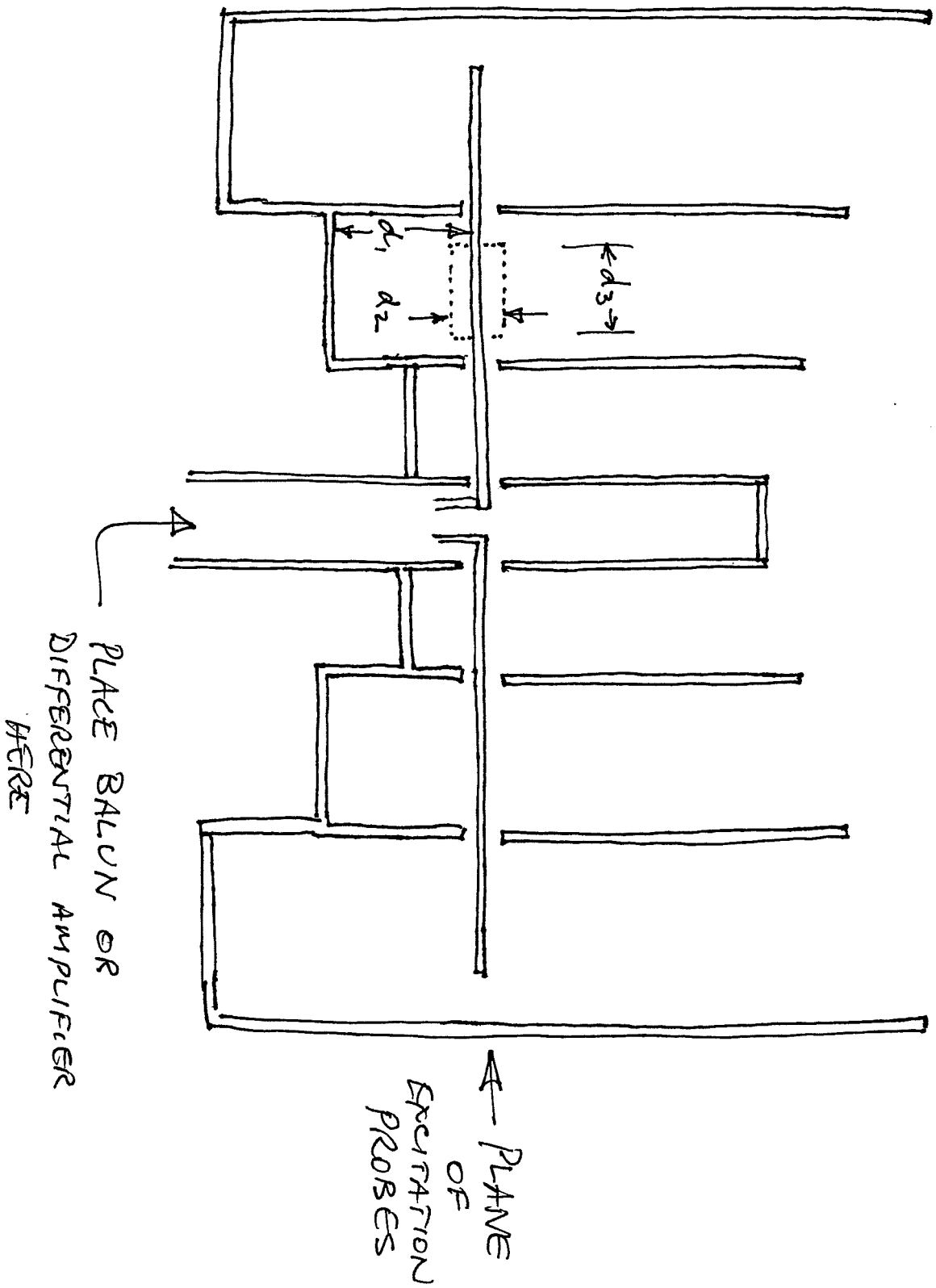


Figure 6: Possible method of exciting the waveguides using a conductor outside the front surface.



PLACE BALUN OR DIFFERENTIAL AMPLIFIER HERE

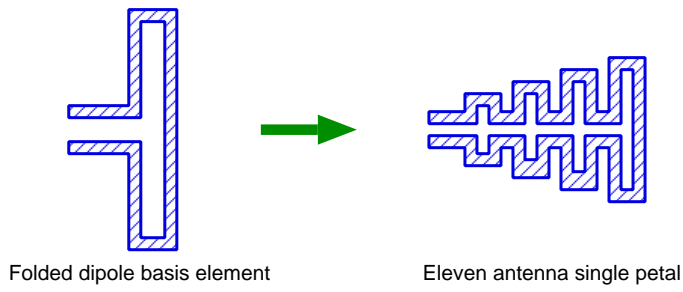
← PLANE OF EXCITATION PROBES

## **Appendix B: DRAO Concept Drawing I**

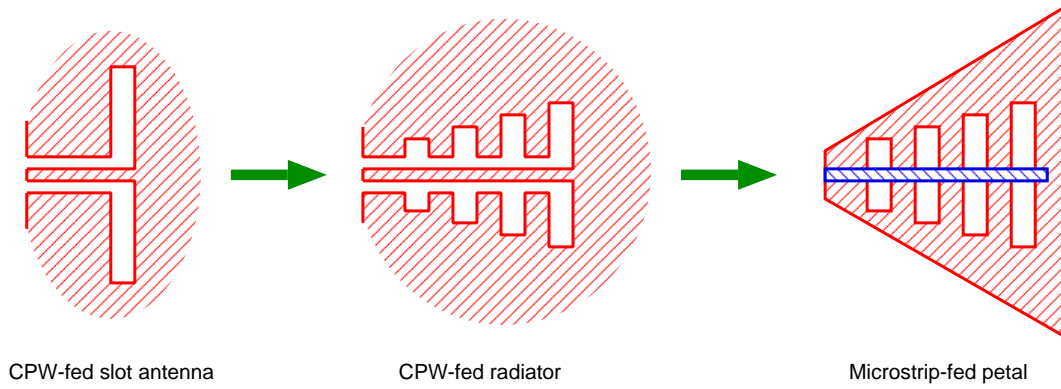
**Document Date:** 1 February 2010

# Variations on the Eleven Antenna

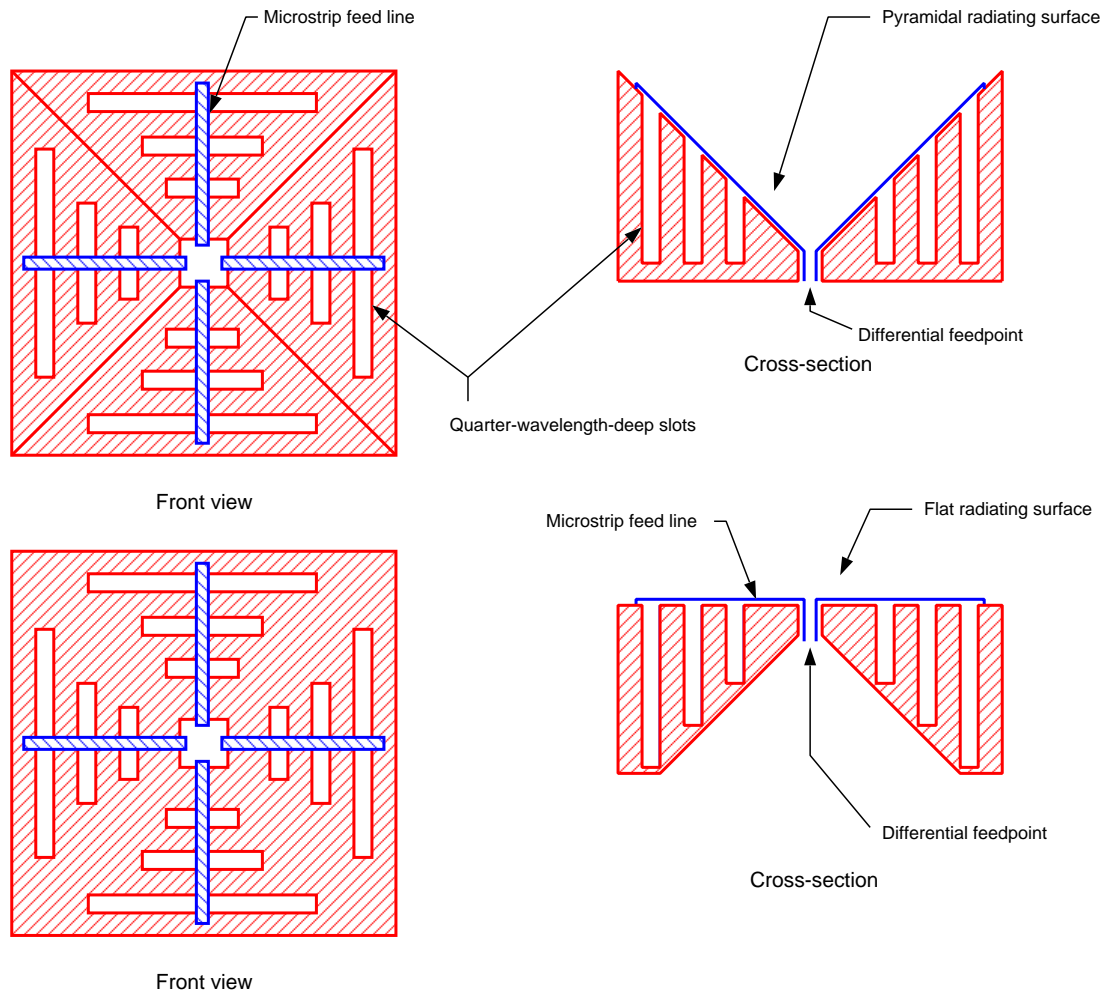
## 1) Conventional Eleven antenna



## 2) Slot-radiator Eleven antenna



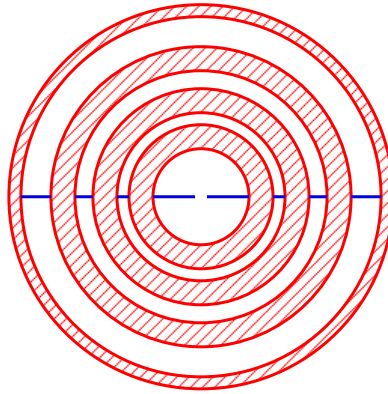
## 3) Eleven antenna horns



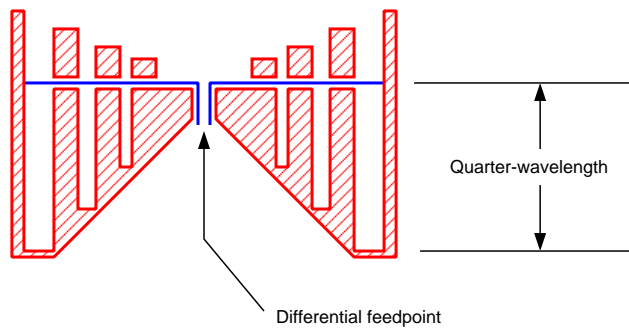
## **Appendix C: DRAO Concept Drawing II**

**Document Date:** 28 February 2010

# Variations on the Eleven Antenna



Top view



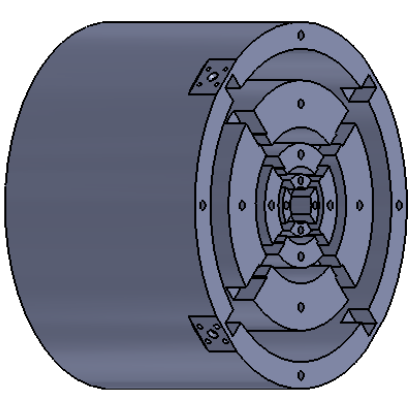
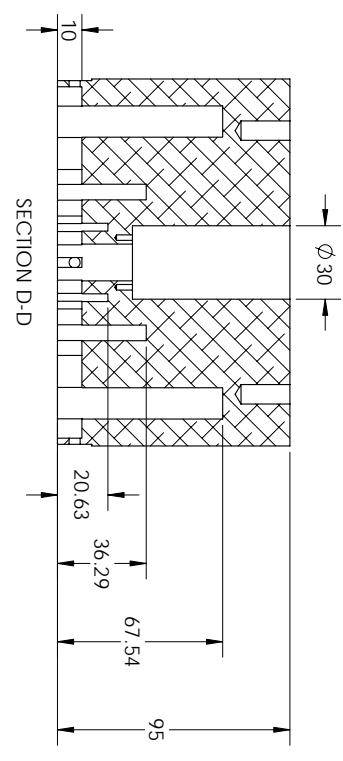
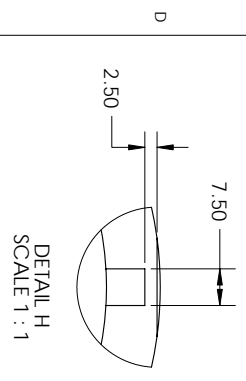
Cross-section

## **Appendix D: Prototype Construction Drawings**

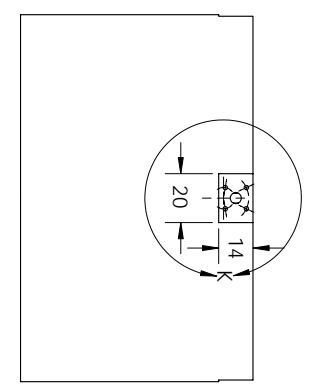




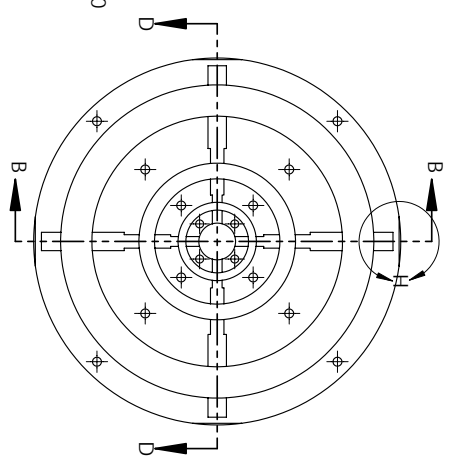




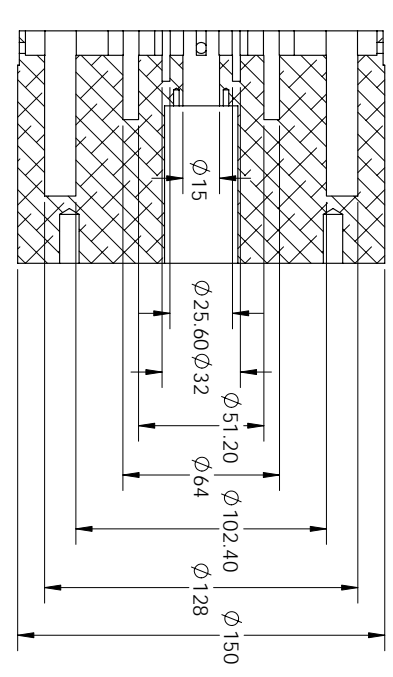
PART 1 - ISO VIEW



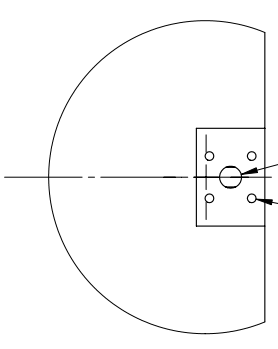
PART 1 - FRONT  
SCALE 1:2



PART 1 - TOP VIEW  
SCALE 1:2



SECTION B-B



DETAIL K  
SCALE 1:1

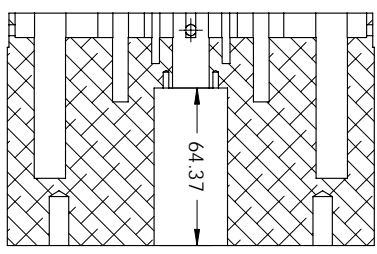
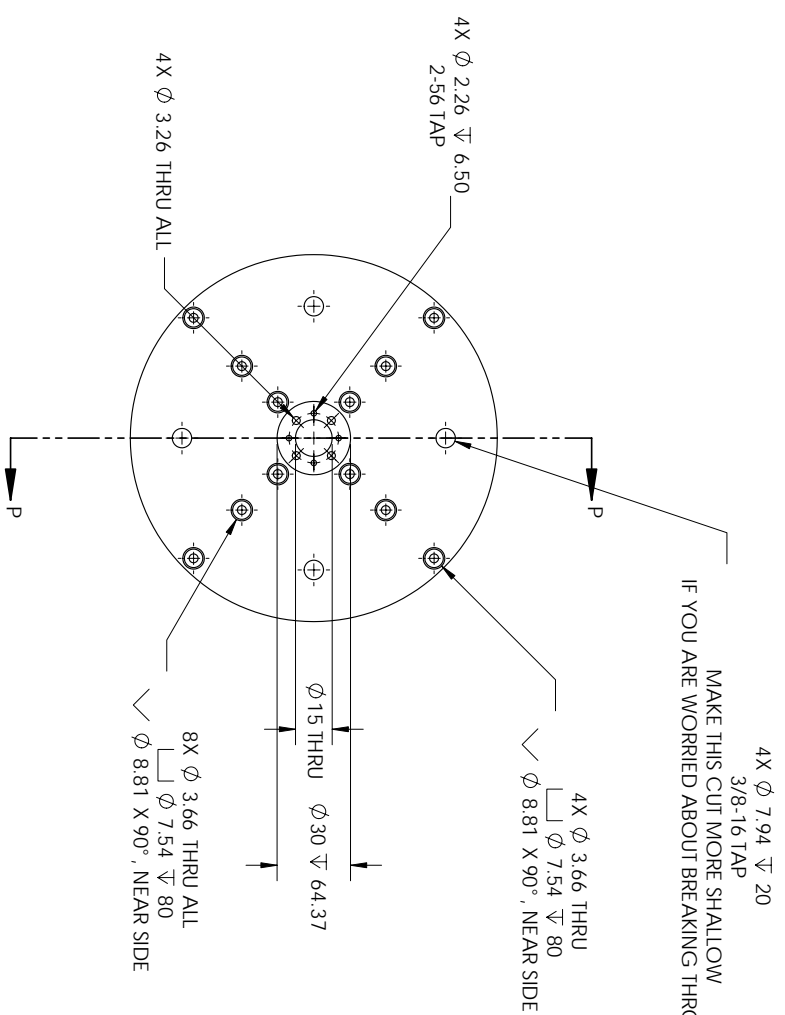
**PROPRIETARY AND CONFIDENTIAL**  
THE INFORMATION CONTAINED IN THIS DRAWING IS THE SOLE PROPERTY OF [FIRM NAME] AND IS NOT TO BE REPRODUCED IN PART OR AS A WHOLE WITHOUT THE WRITTEN PERMISSION OF [FIRM NAME]. [FIRM NAME] COMPANY NAME HERE IS FROBBERD.

NEXT ASSY		USED ON		FINISH		DO NOT SCALE DRAWING		UNLESS OTHERWISE SPECIFIED:		DRAWN		NAME		DATE		TITLE:	
								DIMENSIONS ARE IN INCHES									
								TOLERANCES:									
								ANGULAR MATCH ±									
								BEND ±									
								THREE PLACE DECIMAL ±									
								INTERFRET GEOMETRIC									
								TOLERANCES PER:									
								MATERIAL									
								COMMENTS:									
								O.A.									

SIZE DWG. NO. **B**  
Assembly  
SCALE: 1:2 WEIGHT: SHEET 4 OF 9

REV

PART 1  
SCALE 1 : 2



SECTION P-P

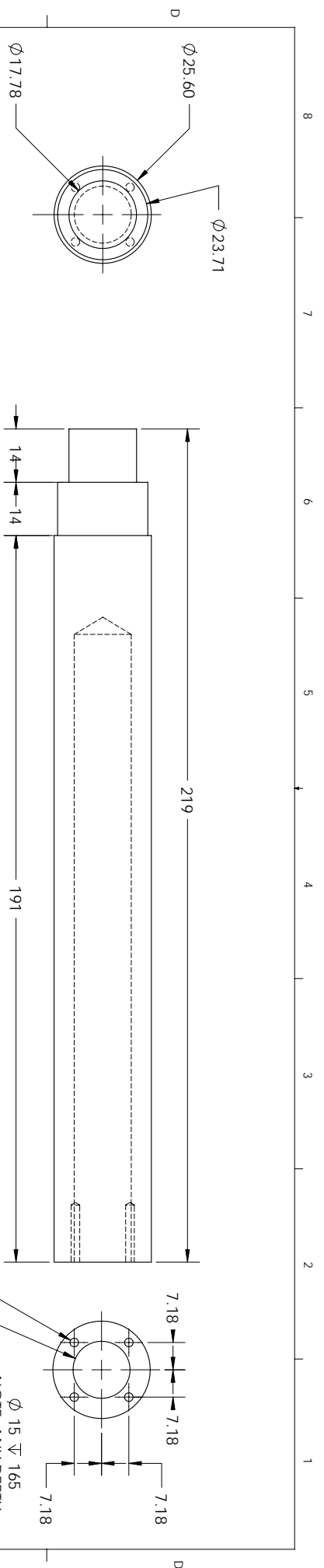
**PROPRIETARY AND CONFIDENTIAL**  
THE INFORMATION CONTAINED IN THIS DRAWING IS THE SOLE PROPERTY OF [REDACTED] AND IS TO BE USED FOR THE REPRODUCTION IN PART OR AS A WHOLE WITHOUT THE WRITTEN PERMISSION OF [REDACTED]. [REDACTED] COMPANY NAME HERE IS PROHIBITED.

NEXT ASSY		USED ON		FINISH		DO NOT SCALE DRAWING		DRAWN		NAME		DATE	
APPLICATION								CHECKED					
								ENG APPR					
								MFG APPR					
								O.A.					
								COMMENTS					
								TITLE:				SIZE DWG. NO.	
												B Assembly	
												SCALE: 1:2 WEIGHT: SHEET 5 OF 9	
												REV	

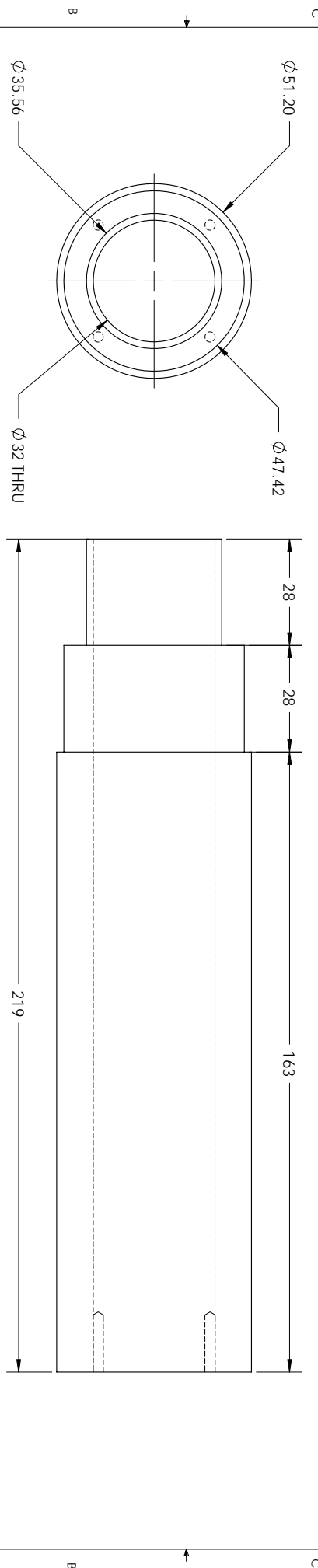
8 7 6 5 4 3 2 1

A B C D

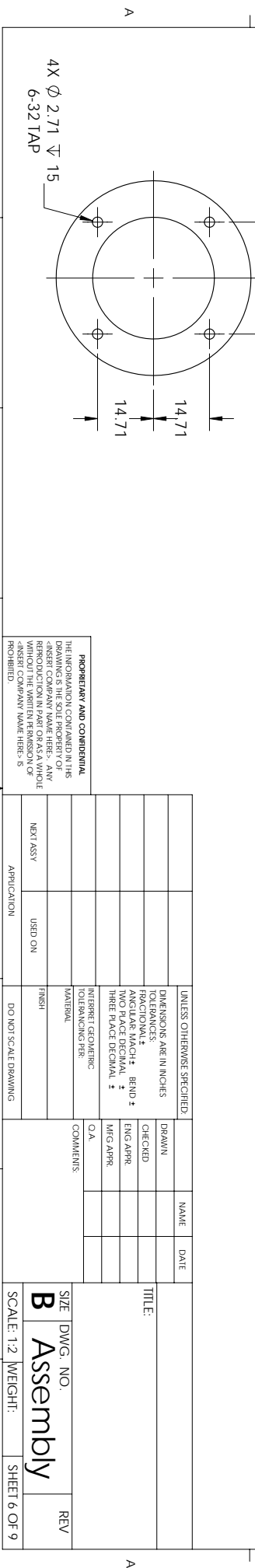
A B C D



PART 2  
SCALE 1:1



PART 3  
SCALE 1:1

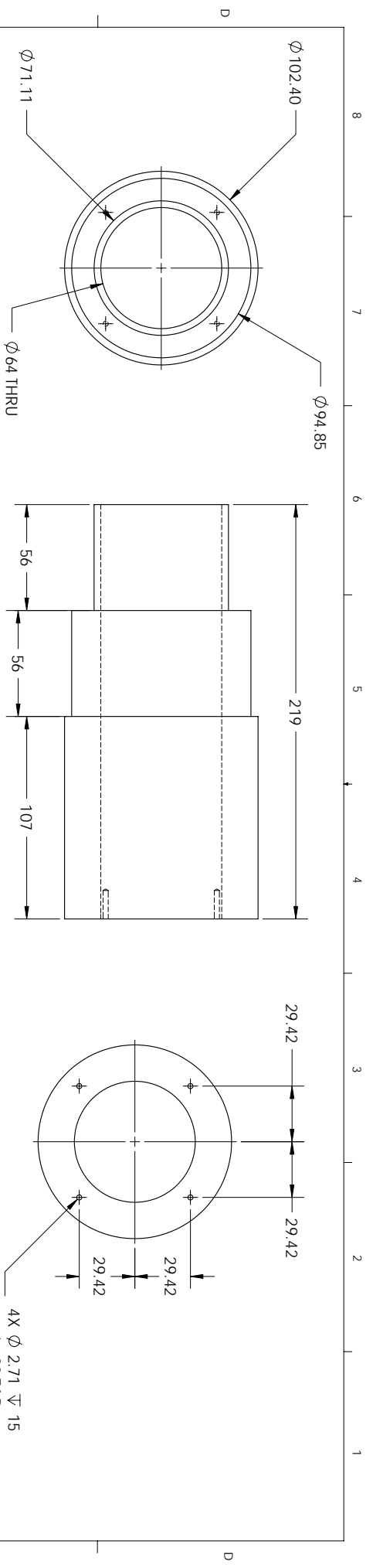


**PROPRIETARY AND CONFIDENTIAL**  
 THE INFORMATION CONTAINED IN THIS DRAWING IS THE SOLE PROPERTY OF THE DRAWING COMPANY AND IS NOT TO BE REPRODUCED IN PART OR AS A WHOLE WITHOUT THE WRITTEN PERMISSION OF THE DRAWING COMPANY. NAME HERE IS PROHIBITED.

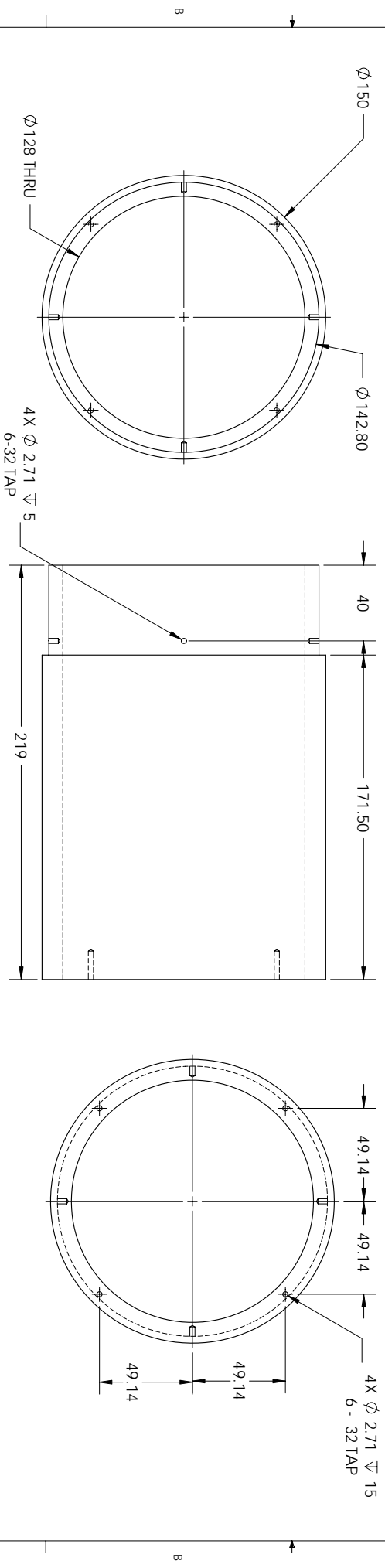
UNLESS OTHERWISE SPECIFIED:		DRAWN	NAME	DATE
DIMENSIONS ARE IN INCHES	TOLERANCES:	CHECKED		
FRAC TIONAL ±	ANGULAR MATCH ±	ENG APPR		
BEND ±	THREE PLACE DECIMAL ±	MFG APPR		
	INTERPRET GEOMETRIC TOLERANCES PER MATERIAL	COMMENTS		
		O.A.		
DO NOT SCALE DRAWING	FINISH			
USED ON	APPLICATION			
NEXT ASSY				

TITLE:  
**B Assembly**  
 DWG. NO.:  
 SCALE: 1:2 WEIGHT:  
 SHEET 6 OF 9

REV



PART 4  
SCALE 1:2

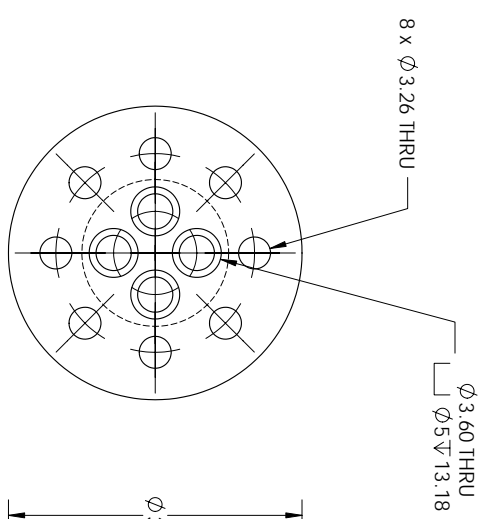
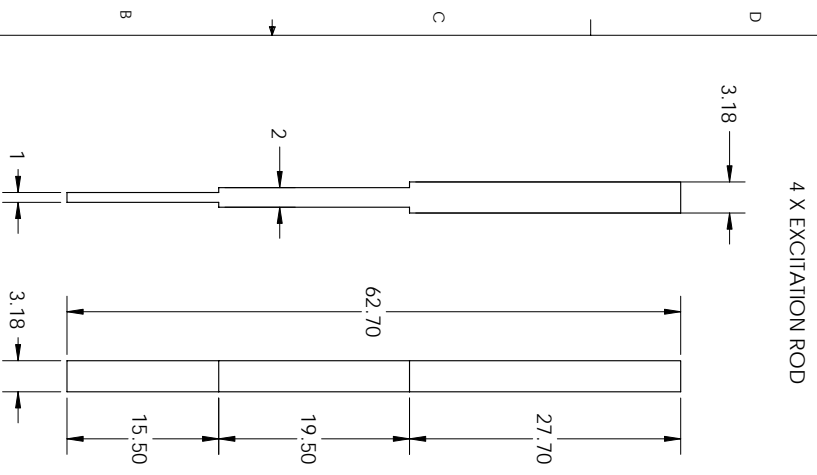


PART 5  
SCALE 1:2

**PROPRIETARY AND CONFIDENTIAL**  
 THE INFORMATION CONTAINED IN THIS DRAWING IS THE SOLE PROPERTY OF [FIRM NAME] AND IS NOT TO BE REPRODUCED IN PART OR AS A WHOLE WITHOUT THE WRITTEN PERMISSION OF [FIRM NAME]. COMPANY NAME HERE IS PROHIBITED.

UNLESS OTHERWISE SPECIFIED:		NAME	DATE
DIMENSIONS ARE IN INCHES	DRAWN		
TOLERANCES:	CHECKED		
FRACTIONAL ±	ENG APPR		
ANGULAR MATCH ±	BEND ±		
THREE PLACE DECIMAL ±	MFG APPR		
INTERPRET GEOMETRIC TOLERANCING PER MATERIAL	COMMENTS		
FINISH			
DO NOT SCALE DRAWING			
USED ON			
NEXT ASSY			
APPLICATION			
SIZE DWG. NO.	REV		
<b>B</b>	<b>Assembly</b>		
SCALE: 1:2	WEIGHT:		
	SHEET 7 OF 9		





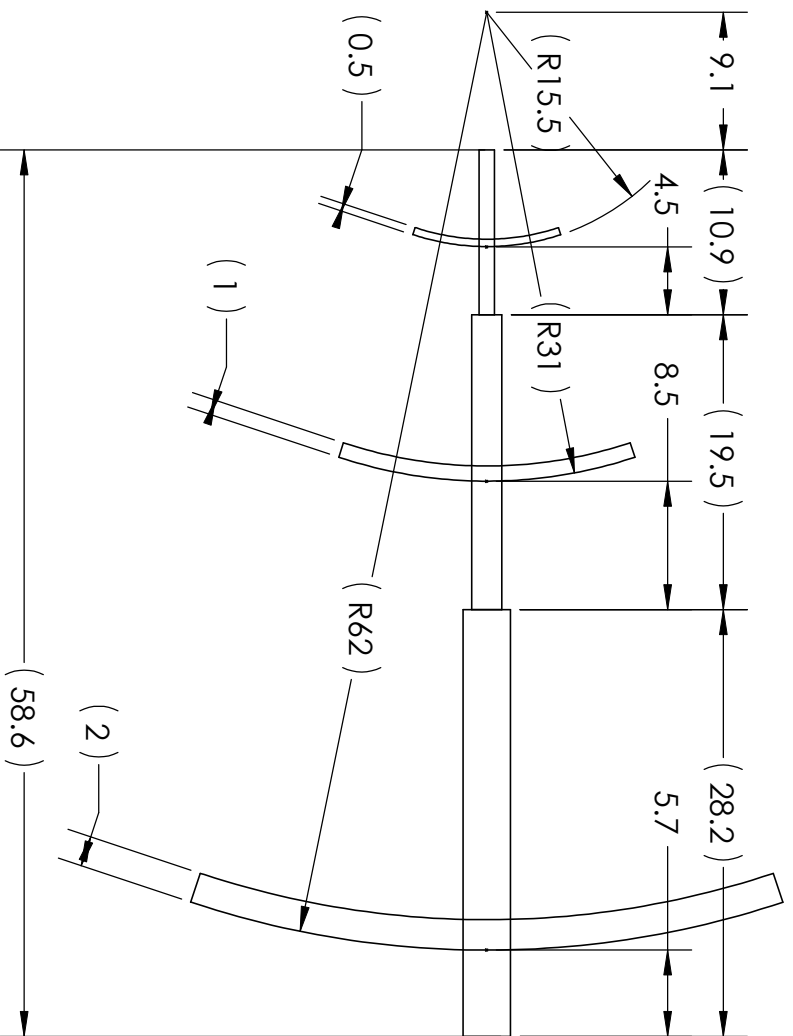
PART 7 - "BRASS PLUG"  
SCALE 1:2

I ORDERED THE BRASS PLUG MATERIAL A LITTLE SHORT. IF YOU NEED TO YOU CAN REDUCE THIS DIMENTION TO AS LITTLE 15.4 BUT I WOULD PREFER TO KEEP IT AS CLOSE TO 20.4 AS POSSIBLE

PART 8  
SCALE 1:1

<p><b>PROPRIETARY AND CONFIDENTIAL</b></p> <p>THE INFORMATION CONTAINED IN THIS DRAWING IS THE SOLE PROPERTY OF [COMPANY NAME] AND IS NOT TO BE REPRODUCED IN ANY MANNER WITHOUT THE WRITTEN PERMISSION OF [COMPANY NAME]. [COMPANY NAME] IS PROHIBITED.</p>		<p>UNLESS OTHERWISE SPECIFIED:</p> <p>DIMENSIONS ARE IN INCHES</p> <p>TOLERANCES:</p> <p>FRACTIONAL ±</p> <p>ANGULAR MATCH ±</p> <p>BEND ±</p> <p>THREE PLACE DECIMAL ±</p> <p>INTERPRET GEOMETRIC TOLERANCES PER MATERIAL</p>		<p>DATE</p> <p>NAME</p> <p>COMMENTS</p>	
<p>DRAWN</p> <p>CHECKED</p> <p>ENG APPR</p> <p>MFG APPR</p> <p>O.A.</p>	<p>DATE</p> <p>NAME</p> <p>COMMENTS</p>	<p>FINISH</p> <p>DO NOT SCALE DRAWING</p>	<p>USED ON</p> <p>APPLICATION</p>	<p>NEXT ASSY</p>	<p>SIZE DWG. NO.</p> <p><b>B</b> Assembly</p> <p>SCALE: 1:2 WEIGHT:</p>
<p>REVISIONS</p>				<p>REV</p>	<p>SHEET 9 OF 9</p>

## **Appendix E: Feed Line Construction Drawings**



UNLESS OTHERWISE SPECIFIED:  
 DIMENSIONS ARE IN INCHES  
 TOLERANCES:  
 FRACTIONAL: ±  
 ANGULAR: MACH ± BEND ±  
 TWO PLACE DECIMAL ±  
 THREE PLACE DECIMAL ±

INTERPRET GEOMETRIC TOLERANCING PER:	
MATERIAL:	
FINISH:	
DO NOT SCALE DRAWING	
USED ON	
NEXT ASSY	
APPLICATION	

NAME	DATE
DRAWN	
CHECKED	
ENG APPR.	
MFG APPR.	
Q.A.	
COMMENTS:	

**PROPRIETARY AND CONFIDENTIAL**  
 THE INFORMATION CONTAINED IN THIS DRAWING IS THE SOLE PROPERTY OF <INSERT COMPANY NAME HERE>. ANY REPRODUCTION IN PART OR AS A WHOLE WITHOUT THE WRITTEN PERMISSION OF <INSERT COMPANY NAME HERE> IS PROHIBITED.

SIZE	DWG. NO.	REV
<b>A</b>	<b>flat-exv4</b>	
SCALE: 1:1	WEIGHT:	SHEET 1 OF 1